MEASUREMENT OF $Z^0 \to e^+e^- +$ N JET CROSS SECTIONS IN $\overline{p}p$ COLLISIONS AT $\sqrt{s} = 1.8$ TeV

by

Susanne Andrea Hauger

Department of Physics
Duke University

Date: Dec. 13, 1995

Approved:

Alfred T. Goshaw, Supervisor

Berndt Müller

Seog Oh

Thomas J. Phillips

Henry R. Weller

Dissertation submitted in partial fulfillment of the requirements for the degree of Doctor of Philosophy in the Department of Physics in the Graduate School of Duke University

1995

ABSTRACT

(Physics — Particle)

MEASUREMENT OF $Z^0 \rightarrow e^+e^- +$ N JET CROSS SECTIONS IN $\bar{p}p$ COLLISIONS AT $\sqrt{s} = 1.8$ TeV

by

Susanne Andrea Hauger

Department of Physics
Duke University

Date: Dec. 13, 1995

Approved:

Alfred T. Goshaw, Supervisor

Berndt Müller

Seog Oh

Thomas J. Phillips

Henry R. Weller

An abstract of a dissertation submitted in partial fulfillment of the requirements for the degree of Doctor of Philosophy in the Department of Physics in the Graduate School of Duke University

1995

Abstract

The Collider Detector at Fermilab (CDF) has collected 106 pb^{-1} of $\overline{p}p$ data from the 1992–1995 Tevatron run, at a center-of-mass energy of $\sqrt{s} = 1.8$ TeV. From this data sample we extract 6708 $Z \rightarrow e^+e^-$ decay candidates, the largest sample available from hadronic collisions. The size of the dataset is sufficient to allow the first measurement of the $Z \rightarrow e^+e^-$ cross section as a function of associated jet multiplicity. In calculating B($Z \rightarrow e^+e^-)\sigma(Z^0 + \geq N$ jets), we make use of a previously measured inclusive $Z \rightarrow e^+e^-$ cross section to obtain relative cross sections for the higher jet multiplicities. We measure B($Z \rightarrow e^+e^-)\sigma$ for jet multiplicities N = 1–4, and study the production properties of the jets produced in association with the Z^0 boson. The data sample is examined for evidence of b-quark secondary decay vertices, and no excess of b-tags over Standard Model expectations is found.

We compare our results with QCD predictions obtained with the heavy boson plus jet tree-level matrix element calculation VECBOS. The VECBOS program generates $Z^0 + N$ parton events for $N = 1-3$. The generated partons are fragmented with a HERWIG routine which adds an underlying event and gluon radiation and introduces color coherence effects in the fragmentation. The events are then processed through a detector simulation. The cross sec-

tions of these fully reconstructed events are compared to the measured cross sections. The ratio of the measured to calculated cross section is computed for jet multiplicities 1–3. We find that the value of this ratio depends on the renormalization scale (Q^2) used in generation, and on the magnitude of the allowed gluon radiation at fragmentation. The best agreement with the data is achieved with $Q^2 = \langle p_T \rangle^2$ of the partons, and essentially unlimited gluon radiation. The kinematic distributions of the boson and jets in these QCD events are compared to the data. We find good agreement between the predicted and measured distributions for all jet production variables.

Acknowledgements

In completing a thesis one owes thanks in varying degrees to so many people that to name them all is an impossibility. Nevertheless, I will attempt to acknowledge those who have been of great personal assistance to me over the past few years, and trust that those whom I inadvertently forget will forgive my omission.

First of all, I wish to thank my colleagues at CDF for the awesome work entailed in commissioning and running a detector like CDF, without which there would literally be no thesis. I would like especially to thank my fellow Aces Young-Kee, Theresa, Kurt, Brian, and Bill, who more than anyone taught me the workings of the experiment, and the VTX crew, with whom I spent many hours debugging electronics.

At Duke, I owe much gratitude to my adviser, Al Goshaw, for getting me interested in high energy physics and for providing me with the guidance and patience which I sorely needed in completing my analysis. Bill Robertson helped me more than I can say through the pitfalls of batch job crashes and debugging nightmares, and in general helped me to keep things in perspective. And Pat Hoyt deserves recognition for all the work she does behind the scenes, and for lending me her ear every morning over my first cup of coffee.

An especially big thank-you goes to my fellow high energy graduate students Jay Dittmann and Dan Cronin-Hennessy, who did enormous amounts of work on this analysis. They bring a freshness and enthusiasm to physics which I must admit tends to elude me in times of stress, and, most importantly, they exhibit heroic patience in listening to my frequently vented frustrations.

Lastly, I turn to those whose emotional support has sustained me through the early years of graduate school and through the writing of a thesis, endeavors which, though ultimately rewarding, are exceedingly trying at times. Among these are my good friends Cal Loomis, Dawn Hasemann, Mickey McDonald, Rich Hornung, Keener Hughen, Alessandra Chiareli and my classmates Mark Godwin and Richard Braun. Most importantly, I thank my fiancé Dinko González Trotter, whose encouragement and love in the last four years have meant more to me than I can express. Of course, through it all and much, much more, my parents Donald and Brigitte Hauger, my sister Tini and my brother Jan have provided me with unwavering support and unceasing entertainment, for which I will always be grateful.

Contents

List of Figures

List of Tables

Chapter 1

Introduction to the Standard Model

1.1 Quarks and Leptons

The study of particle physics constitutes the continuation of a search for elementary particles which was begun when Democritus first postulated an indivisible smallest building block, which he called "atom." Through the years many pretenders for the position of elementary particle have risen and fallen, beginning with the molecule and continuing on through the atom, the nucleus, and the nucleon. The demise of all these candidates was motivated by their prodigious proliferation, which suggested that they actually represented bound-state structures of some as yet undiscovered constituent particles.

The proton and neutron, long considered elementary, turned out to be the lightest of an extended family of nucleons whose numbers approached a hundred. A similarly vast array of strongly interacting bosons, called mesons, added to the confusion. It was inevitable that the proliferation of hadron species would encourage speculation about the existence of more elementary particles, dubbed "partons", from which the hadrons were constructed. Experimental evidence of such substructure was first observed in deep inelastic

scattering experiments at the Stanford Linear Accelerator Center (SLAC) in 1968[B+69]. In these experiments the incident high-energy electron appeared to scatter off point-like particles within the proton.

In 1964 Gell-Mann[GMN64] and Zweig[Zwe64] independently proposed a scheme in which strongly interacting fermions with fractional charge and baryon number constituted the building blocks of the hadrons. Gell-Mann dubbed these particles "quarks"[1]. In the quark scheme, three quarks or three antiquarks combined to form a baryon, while a meson had a quark-antiquark pair.

The model was very successful, apart from a few nagging features which it could not explain. First of all, there was the problem of the Δ^{++} baryon, which consisted of three identical *up* quarks all in a spin-up state. This meant that the Δ^{++} ground state was symmetric, in clear violation of the Pauli exclusion principle. Another mystery was the absence of states corresponding to other quark combinations or even single quarks. Why were no fractionally charged particles ever observed? Why did one never encounter a fractional baryon number?

Both of these problems were solved with the introduction of a new quantum number called "color". Suppose that there are three colors, say red, blue, and green, and three anticolors (antired, antiblue, and antigreen), which obey the $SU_c(3)$ color algebra. Then assigning one each of the colors to the *u* quarks in the Δ^{++} restores the asymmetry of the ground state. If one further supposes that only the "colorless" singlet states can be observed in nature, the simplest combinations of quarks and their colors are limited to three: equal mixtures of all three colors (*e.g.*, rgb); equal mixtures of all three anticolors, (*e.g.*, $\overline{rgb}$); or

[1]The name "quark" comes from the line "Three quarks for Muster Mark" in James Joyce's **Finnegan's Wake**.

equal mixtures of a color and its anticolor (*e.g.*, $g\bar{g}$)—in other words, precisely the combinations which were postulated for baryon and meson construction. As a mathematical tool, then, color served exceedingly well. Luckily, it was a concept for which there was also experimental evidence.

There had been puzzlement for some time over a serious discrepancy between the theoretically predicted and the experimentally measured values of the ratio:

$$R = \frac{\sigma(e^+e^- \to \bar{q}q \to \text{hadrons})}{\sigma(e^+e^- \to \mu^+\mu^-)}.$$

Theory predicted this ratio to be a factor of three smaller than was observed experimentally. Summing the numerator over three allowed quark color states, however, gave

$$R = N_c \sum_i q_i^2,$$

bringing theory and experiment into perfect agreement[2].

Over the years additional quarks were discovered, so that the set of three in the original theory (*up, down,* and *strange*) were soon joined by *charm* (1974), *bottom* (1977), and finally, in 1994, *top*. The six types, called flavors, are divided up into three generations of doublets:

$$\begin{pmatrix} u \\ d \end{pmatrix} \begin{pmatrix} c \\ s \end{pmatrix} \begin{pmatrix} t \\ b \end{pmatrix}$$

The first generation consists of the *up* and *down* quarks, which together make up the nucleons of all the ordinary matter we see. The second and third generations are essentially more massive copies of the first, and are produced

[2]The sum here is over quark flavors for which $2m_i < \sqrt{s}$, and q_i = the quark charges

only in highly energetic conditions. Such conditions existed in the early aftermath of the Big Bang and are now recreated in laboratories to further our understanding of the way the universe began.

A similar family of three generations is seen in the leptons, which are also elementary as far as is known. Each lepton generation consists of a charged lepton (such as the electron) and its massless neutral partner, the neutrino.

$$\begin{pmatrix} e^- \\ \nu_e \end{pmatrix} \begin{pmatrix} \mu^- \\ \nu_\mu \end{pmatrix} \begin{pmatrix} \tau^- \\ \nu_\tau \end{pmatrix}$$

All leptons interact via the weak nuclear force, though the charged leptons can also interact electromagnetically. The six quarks and six leptons, together with their antiparticles, are currently thought to be the elementary buiding blocks of nature. Nevertheless, the apparent redundancy of three generations hints at the possibility of even smaller substructure, speculation which has not (yet) been borne out by experiment. Table 1.1 lists the elementary particles and some of their properties.

The mathematical framework which describes the interactions between quarks and leptons is a relativistic quantum field theory known as the Standard Model. The Standard Model incorporates three of the four known forces: the weak, the electromagnetic, and the strong[3]. Each of these forces is mediated by vector bosons. The electromagnetic force is carried by the photon. In the weak force, the mediators are the massive Z^0 and $W^\pm$ bosons. The strong force, which binds quarks together to form nucleons, is transmitted by gluons. Table 1.2 shows the forces and the vector bosons which mediate them. The

[3]Because of a nagging incompatibility between relativistic quantum mechanics and Einstein's General Relativity, gravity has so far resisted incorporation into the Standard Model.

Table 1.1: The elementary particles.

Particle Name	Symbol	Charge (e)	Mass (MeV/c^2)	Spin	Forces
Quarks					
up	u	+2/3	6	1/2	strong, EM, weak
down	d	-1/3	10	1/2	strong, EM, weak
charm	c	+2/3	1300	1/2	strong, EM, weak
strange	s	-1/3	200	1/2	strong, EM, weak
top	t	+2/3	174000	1/2	strong, EM, weak
bottom	b	-1/3	4300	1/2	strong, EM, weak
Leptons					
electron	e	-1	0.511	1/2	EM, weak
neutrino	ν_e	0	$\simeq 0$	1/2	weak
muon	μ	-1	105.7	1/2	EM, weak
neutrino	ν_μ	0	$\simeq 0$	1/2	weak
tau	τ	-1	1777.1	1/2	EM, weak
neutrino	ν_τ	0	< 21	1/2	weak

Table 1.2: The vector bosons of the Standard Model.

Boson	Symbol	Charge	Mass (GeV/c^2)	Spin	Forces
photon	γ	0	0	1	EM
W	$W^\pm$	+, -	80.4	1	EM, weak
Z	Z^0	0	91.2	1	weak
gluon	g	0	0	1	strong

interplay between the quarks and leptons and the vector bosons is dictated by local gauge symmetries and described by *gauge theories*. These are the Unified Electroweak Theory and Quantum Chromodynamics.

1.2 Quantum Electrodynamics (QED)

Quantum Electrodynamics, or QED, is the prototypical quantum field theory and the simplest of the gauge theories. The force between two charged particles is characterized by the exchange of a field quantum, the virtual photon. Figure 1.1 shows the Feynman representations of the lowest-order QED process for e^+e^- elastic scattering.

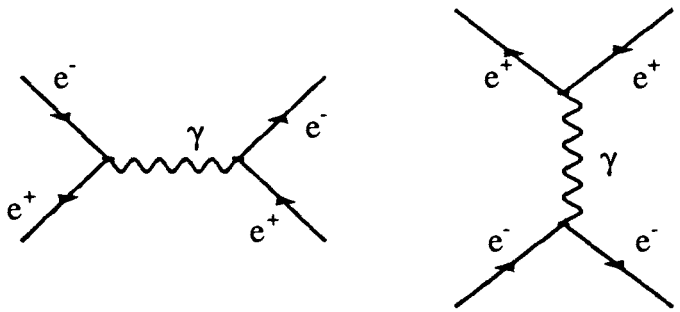

Figure 1.1: Feynman diagrams for the lowest-order QED process.

Originally the calculation of a cross section for such a process was exceedingly difficult, until Feynman introduced a technique which simplified things enormously. He devised a set of rules, now known as the Feynman Rules, which associate each line and vertex of the diagram with a term in the matrix element calculation. Each vertex contributes a factor proportional to $\sqrt{\alpha}$ to the matrix element $\mathcal{M}$, where $\alpha = e^2/4\pi \approx 1/137$ is the electromagnetic coupling constant. Thus the process shown in Figure 1.1 has a cross section $\propto |\mathcal{M}|^2$ of

order α^2.

Alas, diagrams such as this do not represent the whole. Higher-order processes, involving internal loops and additional vertices, constitute an infinite progression of diagrams which must in theory be summed over to yield the correct matrix element. To complicate matters even further, the theory must be *renormalized* in order to avoid infinities which creep in with the higher-order diagrams. Luckily, the small size of the coupling constant allows one to ignore the contributions from higher-order processes. Hence perturbative techniques can be used to calculate cross sections in QED.

1.3 The Unified Electroweak Theory

In 1954, Yang and Mills[YM54] proposed a non-Abelian massless gauge theory with a singlet field corresponding to the photon, and a triplet field corresponding to bosons with isospin and charge. The fact that such bosons had not yet been observed indicated that they were in fact massive, but the introduction of massive gauge bosons into the theory violated gauge invariance. The solution of this problem was the extension of the theory by *spontaneous symmetry breaking* mechanisms by Goldstone[Gol61] and Higgs[Hig64]. In 1961, Glashow developed an SU(2)×U(1) electroweak gauge theory with three massless vector bosons in addition to the photon[Gla61]. A few years later, Weinberg[Wei67] and Salam[Sal68] independently applied the Higgs mechanism to the theory to give the three new gauge bosons their mass. These bosons are the $W^{\pm}$ and the Z^0 . The resulting Unified Electroweak Theory is renormalizable. Glashow, Weinberg, and Salam received the 1979 Nobel Prize for their achievement.

In the Electroweak Model the gauge coupling constant α remains the same

as it was in QED; however, its strength is suppressed by the mass of the bosons to yield an "effective" coupling strength α_W. See Figure 1.2 for the lowest-order Z^0 production diagram. The huge masses of the W and Z^0 , shown in Table 1.2, mean that they are extremely short-lived. They were first observed experimentally in 1983 at the CERN proton-antiproton collider[B+83b, A+83a, B+83a, A+83b].

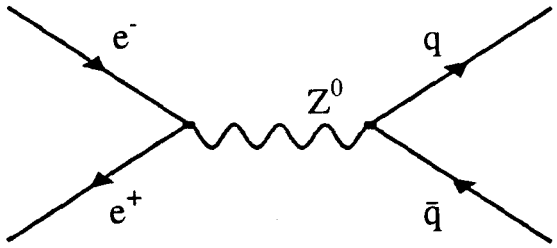

Figure 1.2: Lowest-order diagram of Z^0 production.

While the electromagnetic and strong forces cannot affect the flavor of the fermions with which they interact, the charged W is a flavor-changing mediator (see Figure 1.3). The rate at which flavor-changing can occur across generational boundaries is governed by the Cabibbo-Kobayashi-Maskawa matrix, the elements of which are determined by experiment.

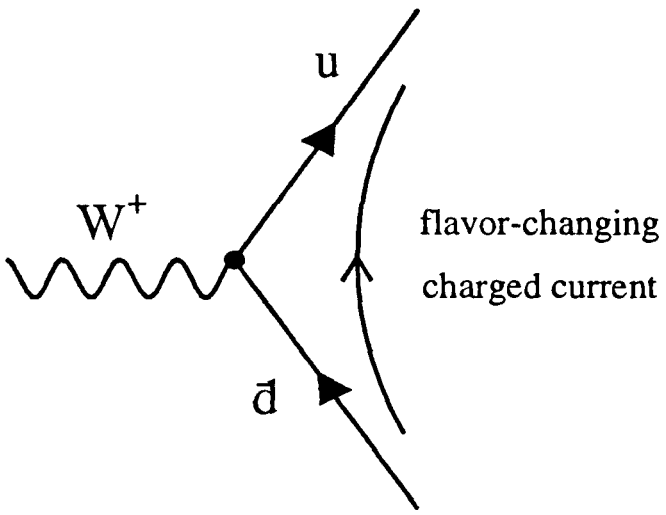

Figure 1.3: The flavor-changing property of the W boson.

1.4 Quantum Chromodynamics (QCD)

Quantum Chromodymanics, or QCD, is a non-Abelian SU(3) renormalizable gauge theory which rigorously describes the workings of the strong force. The field quantum of this theory is the gluon. Gluons, of which there are eight, possess a color and an anticolor. Their exchange between quarks constitutes a color exchange. The first (indirect) evidence for the existence of gluons was the discovery that only about half of the proton's momentum is carried by

quarks. This fact indicated that the other half was carried by something which did not interact with the electron probe. Direct evidence for the existence of gluons soon followed with the observation of three-jet events in e^+e^- collisions at PETRA in Hamburg. These events occur when a colored boson, in this case the gluon, is radiated by one of the quarks produced in the collision (see Figure 1.4).

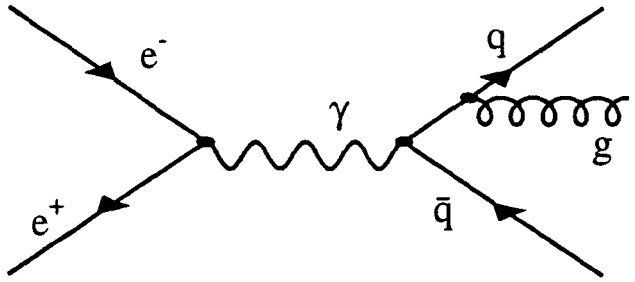

Figure 1.4: A gluon is radiated off a quark line to produce an extra jet.

Though QCD is in many respects similar to QED, and the mechanics of calculating cross sections and other quantities are the same, a major difference arises from the fact that the color-charged gluons can interact among themselves. This aspect of the strong force has an interesting consequence. A bare negative electromagnetic charge is "screened" at large distances (corresponding to small probing energies) by an electromagnetic field of creating and

annihilating electron-positron pairs, because the created positive charges will on average be closer to the bare charge. Thus it is at large distances that α becomes a constant. A bare color charge, on the other hand, is surrounded by a virtual "sea" of quarks and gluons, and will preferentially attract objects of its own color. Thus at small distances (high-energy probes), the color of the bare charge is visible, and the quark appears free (a condition referred to as *asymptotic freedom*). At larger distances (lower-energy probes), the intervening sea will *increase* the measured color, so that the force between widely separated color charges becomes very large. In fact, when two quarks are sufficiently far apart, the potential energy of their separation makes it more economical to create a new quark-antiquark pair to terminate the force lines. This process is known as *hadronization* or *fragmentation.* The potential between quarks is approximated by

$$V(r) = -\frac{4}{3}\frac{\alpha_s}{r} + kr.$$

Because hadronization will always occur when quarks pull apart, free quarks cannot exist. This condition is referred to as *quark confinement*, and it explains why only colorless objects are observed in nature.

All this also means that the QCD coupling strength, α_s, which comes into the matrix element calculation as α does in QED, is not a constant, nor is it necessarily small. It is what is called a "running coupling", and is given, to first order, by[HM84]

$$\alpha_s(Q^2) = \frac{12\pi}{(33 - 2n_f)\ln(Q^2/\Lambda^2)} \tag{1.1}$$

Here, Q is the momentum transfer (*i.e.*, the energy of the probe) and Λ^2 corresponds roughly to the energy boundary between asymptotically free quarks

and hadrons. n_f is the number of energetically allowed flavors. Figure 8.2 shows the dependence of α_s on Q.

Clearly, the perturbative methods used in QED are no longer applicable for large α_s. To render the calculations tractable, we must limit ourselves to the asymptotically free regime where α_s is small, which means that we must investigate processes for which the momentum transfer Q^2 is large. These are called "hard scattering" events. The selection of hard scattering events allows us to test QCD in a region which is calculable.

Chapter 2

Testing QCD with Z^0 + Jet Events

At the Fermilab Tevatron fixed-energy $\overline{p}p$ collider the center-of-mass energies of collisions are given by $\sqrt{s} = 1800$ GeV. Since the protons are not point-like and since the quarks and gluons within each carry some fraction of the proton momentum, the collisions actually sample a broad range of center-of-mass energies. In a typical hard scattering process at Tevatron energies the particles undergoing hard interaction are either gluons or valence quarks [1].

Overall, the incident protons have virtually no transverse momentum component. While the two partons are interacting, the remaining quarks and gluons, dubbed "spectator" partons, continue on in the longitudinal direction and fragment into hadron jets. The jets along the beam direction cannot be measured, so that the longitudinal momentum component of the spectators, and therefore of the interacting pair, remains undetermined. However, the hard interaction itself may have a substantial *transverse* component, which causes the product partons to exit the interaction point well away from the

[1] Valence quarks are the three principal quarks of which the nucleon is composed. There are additional quarks which are continually undergoing pair creation and annihilation. Together with the ubiquitous gluons, they form the parton "sea".

beam. These partons fragment into collimated jets of hadronic particles[2]. We study the transverse components of these jets to avoid the sticky problem of the unknown longitudinal Lorentz boost in the lab frame. If events are chosen with a sufficiently large transverse momentum, the Q^2 of the process involved is guaranteed to be large enough for perturbative QCD to be applicable. Also, since the theory converges logarithmically, higher-order terms in the expansion of α_s cannot be excluded unless Q^2 is very large.

There are several processes we can study which will fall into the perturbative regime. These include the pure QCD jet processes; photon plus jet processes; and heavy boson plus jet processes. Because of the fragmentation of partons the testing of QCD with pure jet events presents unavoidable complications. The nonlinear response of calorimeters to low energy particles means that the energy of the hadrons hitting the detector will not necessarily equal the energy of the original parton; the detector response, especially for hadrons, is also highly dependent on the number of particles in the jet. In addition, there is the difficulty of determining, at the analysis level, what exactly constitutes a jet. At the Collider Detector at Fermilab (see Chapter 5), the clustering algorithm draws a cone about the energy centroid of a particle shower and sums the energies of particles within the cone to arrive at the jet energy. However, there is no way of knowing if some hadronic particles legitimately belonging to the jet happen to fall outside of the cone, or if energy from some other source than the jet falls within it. Both of these scenarios lead to jet energy mismeasurement, and render any precision tests using pure jet events extremely difficult. See Section 7.4.2 for a more detailed discussion of jet energy mismeasurement and

[2]Fragmentation is a soft process, so the resulting hadrons have little momentum transverse to the initial parton direction.

correction.

If one were to study events in which one of the product jets were replaced by a direct photon, or by an electronically decaying heavy boson, one would start with a much cleaner sample in which the transverse energy of the photon or boson can be determined to high precision. This is because the energy in these cases is almost entirely electromagnetic, and is measured with much higher resolution than hadronic energy[3]. Electrons have the additional advantage that they are identifiable by a single track whose momentum closely matches the energy measured in the calorimeters. It is comparatively simple to trigger on photons and electrons, and hence to select well-defined data samples in which jet activity can be studied for high-Q^2 processes[4].

Much of this analysis was motivated initially by the desire to verify that the matrix element calculation and fragmentation algorithms used in the recent top quark search correctly model the production properties of heavy bosons with associated jets, specifically the W + jets events that constitute the major background to lepton + jet top quark decays. Because in this case a "clean" W sample is unobtainable from the data for purposes of comparison to the matrix element calculation, the Z^0 sample, which is essentially free of top contamination, makes a logical substitute[5]. The production processes for the Z^0 and W

[3]This is a consequence of the fact that a nuclear cascade is much less probable than an electromagnetic cascade over a given distance. A lot of hadronic energy goes into breaking up the nuclei of the absorbing medium, or is transferred to slow neutrons where it is not measured.

[4]A high degree of accuracy is achieved also in the measurement of muon momenta. Muons leave only minimum ionizing energy in the calorimeters and are identified by the track stubs they leave in muon chambers many interaction lengths from the event vertex.

[5]There are other reasons why Z^0 data are better to use in QCD tests. Because of the non-interacting neutrino in the W semileptonic decay, there are difficulties associated with identifying W candidates and measuring their energies, as well as with removing the large QCD backgrounds from the W sample. Z^0 bosons decay into well-measured electrons or muons and are readily identifiable by their distinctive invariant mass.

are so similar (see Figure 2.1, for example) that the verification of the reliability of the QCD model for the Z^0 serves to validate its use in modelling W + jets backgrounds in the top quark sample.

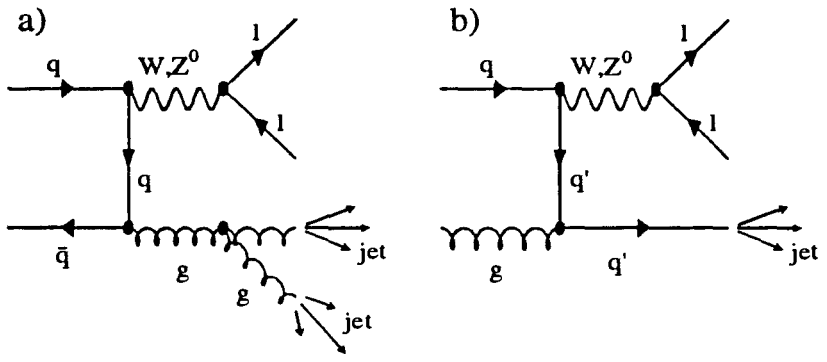

Figure 2.1: Feynman diagrams of vector boson plus jet production. a.) $q\bar{q}$ process (dominant at Tevatron energies) of $\mathcal{O}(\alpha_s^2)$, resulting in a vector boson and two jets. b.) qg $V + 1$ jet process of $\mathcal{O}(\alpha_s)$.

In this analysis we study Z^0 + jets data recorded at the Collider Detector at Fermilab over a three-year period. The Z^0 data sample is the largest available from hadron collisions and contains over 6700 $Z \rightarrow e^+e^-$ decays. We measure the cross sections for $Z \rightarrow e^+e^-+ \geq N$ jet production for jet multiplicities ranging from 1 to 4. These cross sections are compared to cross sections calculated in QCD. We also compare the production properties (such as jet energies, angular distributions, etc.) in the data to QCD predictions. In this way we hope to test the reliability of the QCD model in predicting various aspects of heavy boson plus jet production.

Chapter 3

A Review of the Literature

The first observation of Z^0 bosons at a $\bar{p}p$ collider in 1983[B$^+$83a, A$^+$83b] precipitated a flurry of interest in Z^0 production and decay characteristics at both the theoretical and experimental levels. Z^0 boson properties can be studied most precisely at electron-positron colliders, since center-of-mass energies can be tuned to the resonance mass of the boson. Proton-antiproton colliders facilitate the investigation of the electroweak QCD sector of heavy boson production with associated hadronic jets. In addition, $\bar{p}p$ collisions probe greater interaction energies and larger momentum transfers Q, both of which mark the regime in which new physics beyond the Standard Model is expected to make its first appearance[AEM85, B$^+$89].

By the time the first data were analyzed, the theoretical calculations of Z^0 and W QCD differential cross sections momenta were available. Of particular interest were events in which the boson has substantial transverse momentum, and those with associated jet production. These processes probe the QCD sector and make tests of QCD possible. At zeroth-order QCD ($q\bar{q}$ fusion), the boson has essentially no p_T, except for that imparted by the small

p_T ($\approx$ 1 GeV) of the primordial partons. In $\mathcal{O}(\alpha_s)$ QCD, quark-gluon interactions contribute. In such events, the initial partons can acquire p_T *via* the radiation of a hard gluon[A+89]. The gluon jet resulting from the hard gluon radiation may fail to pass experimental jet selection cuts; nevertheless the p_T of the boson will convey information about the nature of the production process. The average p_T of a heavy boson has been shown to increase with increasing jet multiplicity[B+89], a fact which establishes a link between the two phenomena. It is no surprise, therefore, that Z^0 production cross sections in QCD are often calculated as a function of jet multiplicity or Z^0 boson p_T.

In 1985, Ellis *et al.*[EKS85] calculated the LO W and Z^0 + 2 jet cross sections. In their paper they postulated that, given physically reasonable cuts on the parton momentum and separation, the ratio

$$R_n = \frac{\sigma(V + n \text{ jets})}{\sigma(V + (n-1) \text{ jets})},$$

between the n-jet and $(n-1)$-jet cross sections was constant. Berends *et al.*[B+89] showed a few years later that this simple formula, used with then available NLO inclusive and LO 1-jet calculated cross sections, yielded 2 and 3-jet cross sections within 20% of the LO calculated values. The tree-level 2 and 3-jet calculations had been done using cuts which approximated those used in experiment, and compared favorably to early CDF results. A 1991 paper by Berends *et al.*, using LO QCD matrix elements, confirms that R_n is indeed constant at $\simeq 0.22$ for small jet clustering cone sizes, though for larger cones this does not hold[BKTG91]. The present experimental study of this ratio using CDF Z^0 + N jet data will show similarly constant behavior (see Table 9.1).

In 1990, Matsuura *et al.*[MHvN90] expanded QCD calculations at high

energies to include contributions from the subprocess $gg \rightarrow VX$. This contribution is very small at Tevatron energies, where the dominant contributions to the cross section come from $q\overline{q}$, qg and $\overline{q}g$ interactions.

The differential cross section as a function of Q^2 for inclusive W, Z^0 , and γ^* production was calculated to $\mathcal{O}(\alpha_s^2)$ (NNLO) by Arnold and Reno[AR89] and by Gonsalves *et al.*[GPW89] in 1989. The authors determined that the dependence of the radiative corrections on renormalization and factorization scales was small, and that QCD-improved parton model predictions were therefore reliable and stable for electroweak boson production at large momentum transfers. Their work investigated only medium and high values of Q^2, avoiding the need for gluon resummation. Two years later, Arnold and Kauffman calculated the predicted p_T distributions of W and Z^0 bosons for the entire Q range[AK91], to $\mathcal{O}(\alpha_s^2)$ at large Q and using soft gluon summation at low Q. Matching these techniques at their boundaries led to a NLO result for all Q values. A comparison with preliminary 1990 CDF results showed good agreement between theory and experiment. (For a plot showing a similar comparison, see Figure 3.1).

The first full analyses of hadronically produced Z^0 bosons were done at CERN by the UA1[A$^+$83b, A$^+$86b, A$^+$87a, A$^+$89] and UA2[B$^+$84, A$^+$86a, A$^+$87b, A$^+$90b] collaborations, using data taken at the S$\overline{p}p$S collider during the years 1982-1989. Since then, measurements of B$(Z \rightarrow e^+e^-)\sigma$ at $\overline{p}p$ colliders have been made at four different experiments. The details of the experiments are given in the text; Table 3.1 gives an overview of the cross section measurements to date.

The early CERN data were taken at $\sqrt{s} = 0.546$ TeV. The initial $Z \rightarrow e^+e^-$

Table 3.1: Overview of $B(Z \to e^+e^-)\sigma$ measurements.

Experiment	Year	$\sqrt{s}$ (TeV)	Events	Int. Lum. (pb^{-1})	$B(Z \to e^+e^-)\sigma$ (pb)
UA1	1983	0.546	4	0.136	$50 \pm 20 \pm 9$
UA2	1984		8	0.131	$110 \pm 40 \pm 20$
UA2	1986			0.142	$110 \pm 39 \pm 9$
UA1	1987		4	0.136	$42^{+33}_{-20} \pm 6$
UA2	1987			0.142	$116 \pm 39 \pm 11$
UA1	1989		4	0.136	$39^{+33}_{-20} \pm 4$
Theory					44^{+14}_{-8}
UA2	1986	0.630		0.310	$52 \pm 19 \pm 4$
UA1	1987		12		$74 \pm 14 \pm 11$
UA2	1987			0.768	$73 \pm 14 \pm 7$
UA1	1989		29		$68 \pm 14 \pm 7$
UA2	1990		169	7.8	$70.4 \pm 5.5 \pm 4.0$
Theory					54^{+17}_{-11}
CDF	1991	1.8	243	4.05	$209 \pm 13 \pm 17$
D0	1995		775	12.8	$218 \pm 8 \pm 8 \pm 12$
CDF	1995		1312	19.7	$231 \pm 6 \pm 7 \pm 8$
Theory					222.5 ± 1.1

event sample at UA1 consisted of 4 events, which yielded $B(Z \to e^+e^-)\sigma = 0.050 \pm 0.020 \pm 0.009$ nb; at UA2, 8 (loosely selected) events gave the result $B(Z \to e^+e^-)\sigma = 0.110 \pm 0.040 \pm 0.020$ nb[1]. The paucity of $Z \to e^+e^-$ events made a precison measurement of $B(Z \to e^+e^-)\sigma$ impossible. Nevertheless, the data provided the first experimental number to compare to QCD predictions. The QCD calculations performed by Altarelli *et al.* predicted $B(Z \to e^+e^-)\sigma = 0.044^{+0.014}_{-0.008}$ nb, assuming a top mass of 80 GeV[AEM85].

In subsequent years the center-of-mass energy at the CERN $\bar{p}p$ collider was raised to $\sqrt{s} = 0.630$ TeV. In 1989 UA1 reported their findings based on

[1]In all the cross section results quoted here the first error is statistical and the second systematic. If there is a third error, it reflects the uncertainty due to the luminosity measurement.

1982-1985 data[A+89]. They identified 29 $Z \rightarrow e^+e^-$ events, which led to the measurement $B(Z \rightarrow e^+e^-)\sigma = 0.068 \pm 0.014 \pm 0.007$ nb. A year later, UA2 published a result based on 169 $Z \rightarrow e^+e^-$ candidates[A+90b] from 7.8 pb^{-1} of integrated luminosity. They obtained $B(Z \rightarrow e^+e^-)\sigma = 0.0704 \pm 0.0055 \pm 0.0040$ nb. The theoretical prediction at this energy, again by Altarelli *et al.*, gave $B(Z \rightarrow e^+e^-)\sigma = 0.054^{+0.017}_{-0.011}$, which agrees within errors with the experimental results.

In a related study, UA2 measured the W and Z^0 p_T[A+90a]. They found that the high-p_T tail of the boson, in which an excess of events could potentially signal the presence of new physics, agreed with Standard Model predictions.

In 1991, CDF reported the analysis of their 1988-89 data sample of 4.05 pb^{-1} integrated luminosity. The data were from $\bar{p}p$ collisions at $\sqrt{s} = 1.8$ TeV. CDF measured the cross section for dielectron production[A+91b] for events with $M_{ee} > 30$ GeV/c^2, and found good agreement with the Standard Model predicted Drell-Yan production mechanism. The 406 events in the sample further permitted the first search for additional heavy neutral bosons (Z'), which were excluded at 95% confidence level for $M_{Z'} < 387$ GeV/c^2. Of the dielectron events, 243 passed Z^0 selection cuts, with an estimated background of 5 ± 3. These events yielded $B(Z \rightarrow e^+e^-)\sigma = 0.209 \pm 0.013 \pm 0.017$ nb[A+91a]. The electronic Z^0 candidates were combined with 103 $Z \rightarrow \mu^+\mu^-$ events to yield a measurement of $d\sigma/dp_T$[A+91d]. The comparison of the resulting spectrum over the range $0 < p_T < 160$ GeV/c to NLO QCD prediction yielded a χ^2 fit of 5 per 13 degrees of freedom. The comparison between data and prediction is shown in Figure 3.1. The low statistics prevented a similar investigation of the cross section as a function of jet multiplicity.

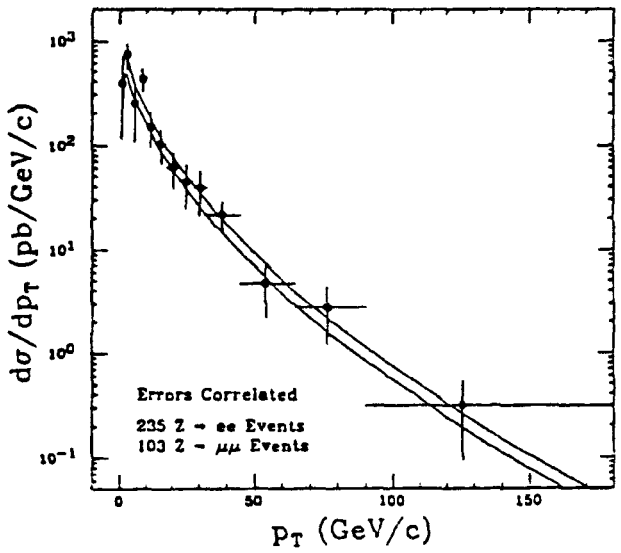

Figure 3.1: The differential cross section for Z^0 production. The NLO QCD calculation is shown as a band, the width of which indicates the theoretical uncertainty. (Plot taken from Reference [A+91d])

Meanwhile, progress on theoretical predictions made it possible to calculate W and Z^0 plus 1 jet cross sections to NLO and 2 jet cross sections to LO and compare them to UA2 and CDF data. In 1991, Brandt *et al.*[BKN91] calculated the QCD predictions for generated jet parameters which approximated the UA2 and CDF jet cuts. Comparing their spectra with the UA2 results at $\sqrt{s} = 0.630$ TeV[A+90a] and the CDF results at $\sqrt{s} = 1.8$ TeV[A+91d], they found good agreement between theory and experiment. They also found a strong dependence in the 2-jet cross section calculation on the factorization and renormalization scales, which they attributed to the fact that contributions

to the calculation at $\mathcal{O}(\alpha_s^2)$ were at LO, which means they came *entirely* from tree-level diagrams. For the 1-jet case at $\mathcal{O}(\alpha_s^2)$, on the other hand, there were contributions from tree-level *and* virtual diagrams. The higher-order corrections compensated for the dependence on mass scales, making the NLO $\mathcal{O}(\alpha_s^2)$ 1-jet cross section prediction much more meaningful from the theoretical point of view.

In 1993 CDF published a paper on $W + n$ jet cross sections for $n = 0 - 4$[A+93]. The events were extracted from 4.05 pb^{-1} of 1988-89 data. The corresponding sample of $Z^0 + n$ jet events was too small for meaningful analysis. Both electronic and muonic W decays were included. For the cross section measurement, the jets were clustered in a cone of radius $R_j = \sqrt{\Delta\eta^2 + \Delta\phi^2} = 0.7$ and had the requirements $E_T{}^j > 15$ GeV (corrected) and $|\eta^j| < 2.4$. The data were compared to VECBOS $W + n$ jet LO matrix element calculations[BKTG91] using a Field and Feynman fragmentation function[FF78] tuned to CDF data. The parton cuts at generation were $p_T > 8$ GeV/c, $|\eta| < 2.5$, and $\Delta R_{pp} \geq 0.6$. Parton jets were defined as cones in the final state centered on the initial parton direction, with the final data selection cuts applied. The reconstructed multiplicity n included the contributions of processes generating n, $n - 1$, and $n + 1$ parton jets, normalized to each other according to their cross sections. It was found that the relative jet rates and the shape of the kinematic distributions in the data were well reproduced by QCD, but that the dependence in the QCD calculation on the Q^2 scale increased with jet multiplicity. The data were found to favor a Q^2 scale smaller than M_W^2. Figure 3.2 shows a plot of the W cross sections as a function of associated plot multiplicity.

The most recent work on Z^0 cross sections was submitted this year by the

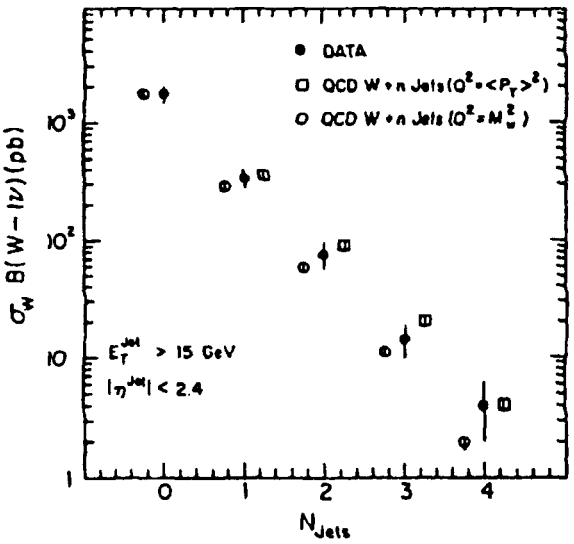

Figure 3.2: $B(W \to l\nu)\sigma$ as a function of jet multiplicity. The QCD predictions are estimated at two different Q^2 scales and include hadronization. (Plot taken from Reference [A+93])

D0 and CDF collaborations. The D0 work[A+95b] is based on a $Z \to e^+e^-$ event sample extracted from 12.8 pb^{-1} of data. There are 775 events in the sample (with an estimated background of about 4 events), from which an inclusive Z^0 cross section $B(Z \to e^+e^-)\sigma = 0.218 \pm 0.008 \pm 0.008 \pm 0.012$ nb was extracted. The first error is statistical, the second systematic, and the third reflects uncertainties in the luminosity measurement. The NNLO QCD prediction with CTEQ2M parton distribution functions yields $B(Z \to e^+e^-)\sigma = 0.2225 \pm 0.0011$ nb, in excellent agreement with the data.

Using a 19.7 pb^{-1} $Z \to e^+e^-$ sample of 1312 events with a background of 21 ± 9, CDF measured $B(Z \to e^+e^-)\sigma = 0.231 \pm 0.006 \pm 0.007 \pm 0.008$ nb[A+95c]. This is a significant improvement in the luminosity measurement compared to previous CDF publications, from a 6.8% to a 3.6% uncertainty. The result has

been compared to NNLO QCD calculated cross sections for five different parton distribution functions, and all are within 1σ of the CDF measurement. For a comparison of inclusive W and Z^0 cross section measurements at $\sqrt{s} = 0.630$ TeV and $\sqrt{s} = 1.8$ TeV with theoretical predictions, see Figure 3.3.

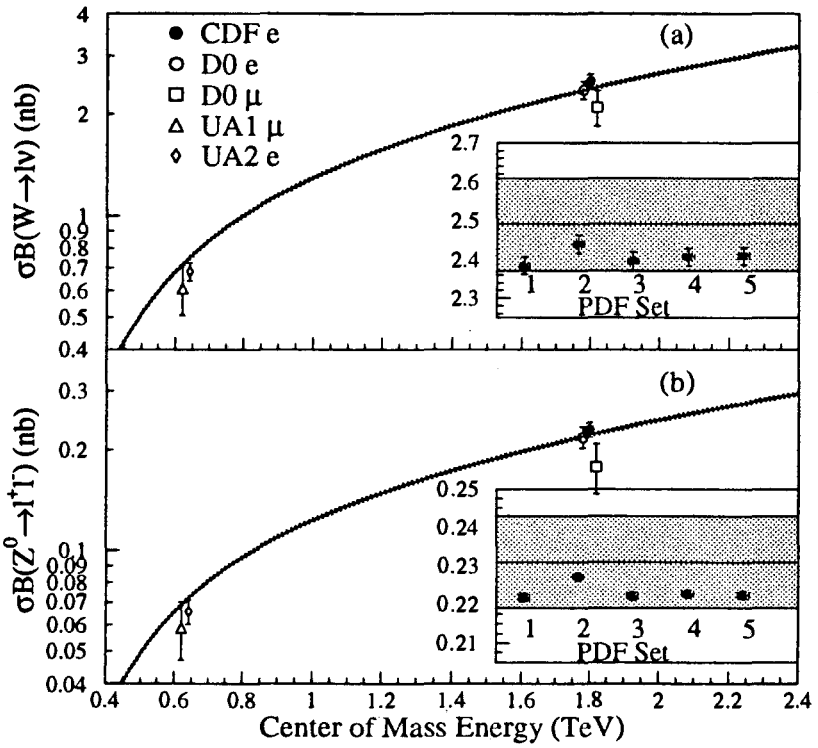

Figure 3.3: Comparison of measured cross sections a.) $B(W \to e\nu)\sigma$ and b.) $B(Z \to e^+e^-)\sigma$ to NNLO theoretical predictions using MRSA parton distribution functions. The shaded area in the inset shows the 1σ region of the CDF measurement; the stars show predictions using the five PDF sets (1) MRSA, (2) MRSD0′, (3) MRSD-′, (4) MRSH, and (5) CTEQ2M. (Plot taken from Reference [A+95c])

Both the CDF and D0 experiments are currently amassing more data, with an expected final yield of over 100 pb^{-1} of integrated luminosity each. Up to now CDF has accumulated over 6700 $Z \to e^+e^-$ candidates, an event sample

which has sufficiently high statistics to permit the first measurement of $Z^0 + n$ jet cross sections and a careful comparison to LO QCD predictions. In addition to improving our understanding of the QCD theory underlying heavy boson plus jet production processes, this measurement is useful in the search for new heavy particles[AEM85, B+89, GPW89] and in the extraction of the value of α_s, which has been attempted previously using W events by the UA2, UA1, and D0 collaborations[A+91e, L+92, A+95a, A+88c]. This thesis describes the CDF $Z^0 + n$ jet cross section analysis.

Chapter 4

The Fermilab Tevatron

The Tevatron at Fermilab is the highest-energy proton-antiproton accelerator in the world. It can deliver 800 GeV protons to a complex of four different experimental areas when running in fixed target mode. When operating in colliding beam mode, it produces $\bar{p}p$ collisions at center-of-mass energies of 1.8 TeV. These energies, combined with high instantaneous beam luminosities[1], make it possible to study processes with high momentum transfers (Q^2) and small production cross sections. The luminosities delivered by the accelerator group at the Tevatron have increased from 1992 to the present by about an order of magnitude, from $\mathcal{L} \approx 3 \times 10^{30}$ cm^{-2}s^{-1} to almost 3×10^{31} cm^{-2}s^{-1}.

Delivering these high-energy protons and antiprotons to the experiments is a complicated process. It involves precise coordination among the numerous accelerator stages that raise the energies of the beams bit by bit to the final 0.9 TeV. A schematic of the Tevatron accelerator complex is shown in Figure 4.1. A description of the acceleration process follows (see also [Dug89, Led91, Sho91, YN90]). We begin with the birth of the proton beam from a hydrogen gas and

[1]The instantaneous luminosity of a beam is a measure of its intensity. The product of the luminosity and a reaction cross section yields the expected event rate for that process.

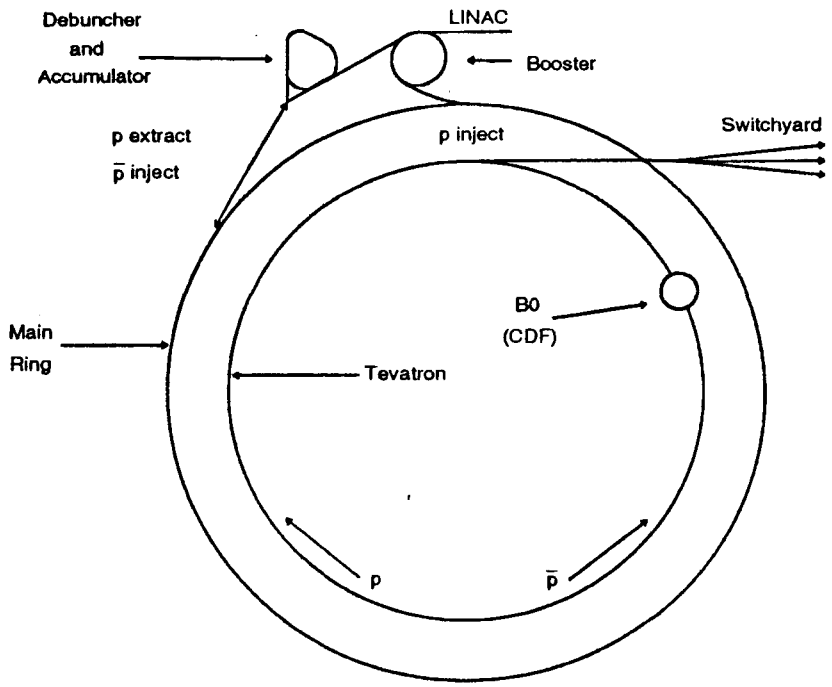

Figure 4.1: Schematic of the Fermilab accelerator complex. The main ring and the Tevatron physically occupy the same tunnel. The CDF experiment is located at the B0 interaction region, as shown.

end with its violent demise in the bowels of a detector.

The protons are extracted in the form of negatively ionized hydrogen (H^-) from a hot plasma of cesium and H_2. The hydrogen ions are subjected to a constant electric field in a Cockroft-Walton accelerator. They exit with a momentum of 750 keV/c and continue on into the 150 m long linear accelerator. Here a radio-frequency wave accelerates the ions to a final momentum of 400 MeV/c. The nature of the RF field causes the ions to exit in bunches. A dipole magnet deflects the pulsed beam of ions into the booster ring, where they hit a carbon foil target which strips them of their electrons. The resulting proton beam is then forced into an 80 m radius circular orbit by a series of

dipole magnets. The intensity of the proton beam is increased by the continual injection of ions until approximately 10^{13} protons have been accumulated. At this point the booster accelerates the protons to 8 GeV/c.

The protons now enter the main ring, a synchrotron of 1 km radius. The main ring has two major functions. One is the acceleration of proton and antiproton beams to an energy of 150 GeV for injection into the superconducting Tevatron. The other is instrumental in the production of antiprotons.

Antiprotons do not occur naturally and are difficult to produce, especially in the numbers that are required for colliding beam operation. At Fermilab, the main ring and two specially designed storage rings are involved in the production process. The main ring accelerates protons to an energy of 120 GeV. The protons are then extracted and strike a tungsten target. The resulting decay products include 8 GeV antiprotons, which are focused into a beam using a lithium lens in which a large magnetic field gradient is created with a 600,000 A current pulse. The antiproton beam has the same bunched structure as did the incident protons. The beam passes on into the debuncher ring, where the longitudinal momentum spread of the bunches is reduced from 3.5% to 0.2%[Sho91]. This results in a complementary increase in the spatial spread of the bunches. Concurrently, the debuncher reduces the transverse momentum spread of the beam by stochastic cooling. Sensors detect the deviation of a particle from an ideal orbit and send an amplified signal across the ring to a kicker. The kicker receives the signal before the antiproton gets there, and applies an electric field to force the errant particle back into the correct orbit. Of course the field affects other particles also, introducing noise into the system. Consequently the stochastic cooling process is rather slow. However, after about four hours there is a dense core with a transverse momentum spread of

only a few MeV/c. The accumulator receives the bunches from the debuncher and stores them until they are needed for collisions. In the meantime it continues to cool them further. It takes approximately eight hours to accumulate a "stack" of antiprotons sufficiently large for a "shot", that is, for injection into the Tevatron. Usually a good-sized stack has about 10^{12} antiprotons.

Having done its duty in the production of antiprotons, the main ring accelerates protons to 150 GeV and injects them in six bunches into the Tevatron. The Tevatron has the same radius as the main ring and lies directly below it in the same tunnel. It is capable of accelerating the beams to higher energies because of its superconducting magnets, which produce fields powerful enough to keep the beams in a tight orbit. If the Tevatron is operating in fixed-target mode, the proton beams are accelerated to 800 GeV and then shunted off to the switchyard, from which they are transferred to the various experiments on the meson, proton, muon and neutrino lines. In colliding beam mode, the protons remain at 150 GeV, rotating around the ring in a clockwise direction, while they wait for the arrival of the antiprotons.

When the antiproton stack is large enough, the accumulator injects a portion of it into the main ring, where its energy is raised to 150 GeV. Then the antiprotons are transferred to the Tevatron in six bunches, circulating counterclockwise. Once all twelve bunches are in the Tevatron, it ramps up their energy to 900 GeV ("flat top"). The beams have now attained their final energy, but a few steps remain before collisions can begin. First of all, quadrupole and octupole magnets focus the beam to give it a cross section of about 0.1 mm. This is referred to as a "low β squeeze."[2] Next, the p and $\bar{p}$ bunches are

[2]The β function value depends on the configuration of the quadrupole magnets around the ring. Luminosity is maximized if the minimum value of β is realized at the detector center.

rotated, or "cogged," with respect to one another so that they pass each other at six predetermined points on the ring. These points are designated A0, B0, and so on to F0. Although in theory B0–E0 can all support experiments[3], only B0 and D0 currently do so. The beams actually collide at B0 and D0, while separators prevent $\overline{p}p$ collisions at the remaining crossing points.

The last step in tuning the Tevatron beams is "scraping." In this step collimators remove a peripheral halo of particles from the edges of the beam to minimize radiation losses in the detectors. If the losses exceed normal values, the beam is dumped within 3.1 μs at one of the beam dump sites around the ring.

If all has gone well to this point, six bunches consisting of about 2×10^{11} protons and six bunches of 6×10^{10} antiprotons are colliding, with a bunch crossing time of 3.5 μs. Data taking can begin. Generally, the main ring remains active during collisions, making a new stack of antiprotons. This reduces the intervals between shots and maximizes the data-taking time for the detectors. A shot may last up to about 20 hours, with the initial instantaneous luminosity declining steadily over that period. A typical initial luminosity at B0 in the 1992-1995 run was $\mathcal{L} \approx 7 \times 10^{30}$ cm^{-2}s^{-1}.

[3]A0 and F0 are beam injection and extraction points.

Chapter 5

The Collider Detector at Fermilab: CDF

The Collider Detector at Fermilab (CDF) is a multi-purpose high transverse momentum detector located at the B0 collision point on the Fermilab Tevatron. It was commissioned in 1985 and has since been used in three data-taking runs. In the first of these, the '88-'89 run, 4 pb^{-1} of integrated luminosity[1] were collected. In the ensuing three years the CDF was upgraded in preparation for the expected rise in instantaneous luminosity to be delivered by the Tevatron. Several detector subsystems were replaced (such as the vertex chamber), improved (central muon detectors), or newly installed (the silicon vertex chamber). These detector components, as well as the original detector, will be described in detail later in this chapter.

In May of 1992 data-taking resumed with the first part of Run 1 (Run 1A) and continued until May of the following year. The 1A data comprised 19.6 pb^{-1} of integrated luminosity. A four-month shut-down was used to replace the radiation-damaged silicon vertex detector (SVX) with its rad-hard successor

[1]Integrated luminosity is the instantaneous luminosity integrated over the total time over which beam was delivered.

SVX′. During this time a new data acquisition system was installed and tested. In October of 1993 Run 1B began and is still in progress. It is scheduled to run until February of 1996, with an anticipated accumulated luminosity of ≈150 pb^{-1}. The data used in this analysis were collected before a brief scheduled shut-down in the summer of 1995. Combining the 1A and 1B data up to the shut-down yields 106 pb^{-1} of luminosity.

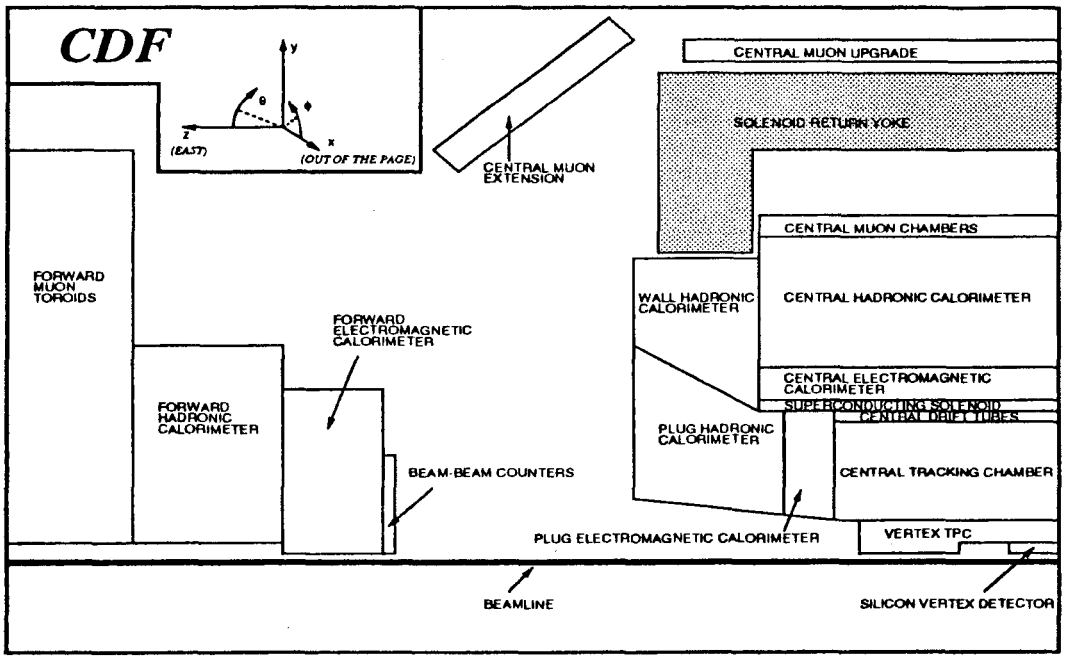

Figure 5.1: A side view cross section of the CDF detector. The detector is forward-backward symmetric about the interaction region, which is shown at the lower right corner of the figure. The proton direction is to the left, along the positive z axis.

The CDF[A+88a] is a forward-backward and azimuthally symmetric detector with its geometric center positioned at the nominal collision point. Its coverage includes the full azimuthal range and extends to within 2° of the beam axis on either side. A side view of one half of the detector is shown in Fig-

ure 5.1. The CDF coordinate system takes the direction of the proton beam to be the positive z-axis. The y-axis points upward; the x-axis points radially out of the Tevatron ring in compliance with the right-hand rule. The azimuthal angle ϕ is measured from the positive x-axis; the polar angle θ is measured with respect to the positive z-axis. Generally at CDF a polar position is given in terms of the pseudorapidity η, which is defined as

$$\eta = -\ln(\tan\frac{\theta}{2}).$$

The detector is divided into three subdetector regions, each of which is finely segmented in ϕ and η. The central region extends out to $|\eta| < 1.2$. The plug region covers the range $1.1 < |\eta| < 2.4$, and the forward, $2.2 < |\eta| < 4.2$.

5.1 The Beam-Beam Counters (BBC)

The Beam-Beam Counters (BBC)[A+88a] are very small scintillating tile detectors located 5.8 m from the nominal interaction point on both sides of the CDF. They cover the pseudorapidity range $3.24 < |\eta| < 5.9$. They are used as luminosity monitors and provide a minimum bias trigger for detector readout. The minimum bias trigger requires that there be at least one hit in both detectors within 15 ns of the beam crossing time. The luminosity delivered to CDF is determined by counting the number of times the minimum bias requirement is met.

5.2 The Central Region

The central detector can be thought of as being a roughly cylindrical detector with the beampipe as its axis. The inner sections of the detector are occupied

by various tracking chambers, all contained within a 1.4 Tesla solenoidal field. Outside the solenoid, arranged in a projective tower geometry, are the electromagnetic and hadronic calorimeters. Beyond these are the central muon drift chambers. The subsystems are described in detail below.

5.2.1 The Tracking Detectors

The Silicon Vertex Detector (SVX)

Directly outside the 1.9 cm radius beryllium beam pipe lies the Silicon Vertex Detector, or SVX[B+92, A+94d]. It is used to determine track impact parameters in the transverse $(r-\phi)$ plane with a resolution of 15 μm. This precision enables it to reconstruct the secondary vertices arising from c and b quark decays. From these secondary vertices it is possible to determine the lifetime of the quarks. The identification of secondary vertices is also central to a process known as b-tagging, in which jets in an event are examined for b vertices. Jets containing such a vertex are tagged as b jets, thus distinguishing them from the large number of QCD jets from light quark and gluon evolution normally produced at high energies.

The SVX was installed in 1991. It consists of two barrels, each 25.5 cm long, laid end-to-end, with the nominal collision point in the center between them. The isometric view of one of the barrels is shown in Figure 5.2. Since the distribution of the primary collision vertices at CDF approximately describes a Gaussian curve with a σ of 30 cm, roughly 60% of all events have a vertex which lies within the SVX fiducial volume. The SVX barrels each have twelve 30° ϕ-wedges containing four layers, or ladders. The detector medium consists of p-type deposits in narrow axial strips on silicon chips. The signals, created

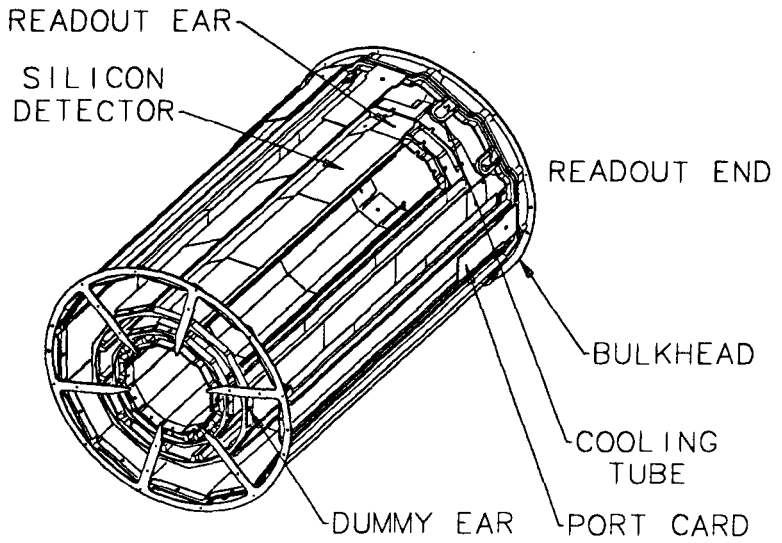

Figure 5.2: Isometric view of the SVX.

by voltage drops in the strips due to the passage of ionizing particles through the silicon, are read out from the ladders by a chip, and sent to the level 3 trigger (Section 6.3) for use in offline analyses. There are a total of 46,000 channels in the SVX.

The radiation-hard SVX′, which replaced the SVX in 1994, has essentially the same design as its predecessor, except that some ϕ gaps existing in the earlier version were closed.

The Vertex Detector (VTX)

The Vertex Detector, or VTX, lies outside the SVX and has an outer radius of 22 cm. It is used to identify the primary collision vertex of an event along the

z direction with an accuracy of $\sigma_z = 1$ mm, and to provide limited tracking in $r - z$ for particles which are produced too far forward to fall within the fiducial volume of the Central Tracking Chamber. Its spatial resolution in $r-z$ is 200-500 μm. The VTX identifies the event vertex by reconstructing the tracks of charged particles and extrapolating them back to the beam position. The quality of the primary vertex depends on the number of tracks and the number of hits found in the VTX. Only track segments with extrapolated vertex positions within ± 150 cm of the detector center are considered.

The VTX is a proportional wire chamber. It has a total of 56 modules laid end-to-end. Adjacent modules have a relative rotation angle of $\phi = 11.3°$. Each module has eight wedges, or octants, in which wires are arranged circumferentially, forming a plane transverse to the beam. There are 8448 channels in the VTX. Field-shaping wires parallel to the sense wires provide a constant potential. The VTX uses a 50%/50% mixture of argon and ethane with 0.7% isopropyl, for which the drift velocity is 46 μm/ns. Charged particles passing through the gas ionize it; the freed electrons drift to the sense wires and cause a voltage drop. The resulting signal is amplified, shaped, discriminated, and digitized.

The Central Tracking Chamber (CTC)

The Central Tracking Chamber, or CTC[B+88b], is a barrel-shaped wire chamber which surrounds the VTX. It extends outward to a radius of 138 cm and is 3.2 m long. It is used to reconstruct the tracks and determine the momentum of charged particles exiting the collision in a pseudorapidity range of $|\eta| < 1.2$. (It should be noted that beyond $|\eta| = 1.1$ the particle does not traverse the entire CTC and momentum measurements are somewhat degraded.) Since the

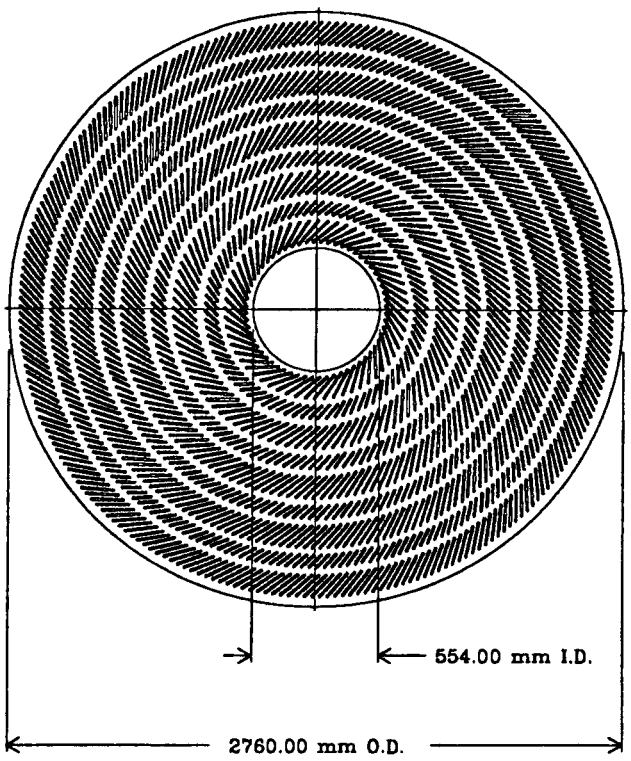

Figure 5.3: Endplate of the Central Tracking Chamber.

CTC is immersed in a magnetic field of 1.4 Tesla, the charged particles are subject to Lorentz forces. Consequently the curvature of a particle trajectory is a measure of its momentum, and the direction of curvature indicates the sign of the charge. The momentum of a particle is determined with a precision of

$$\frac{\delta p_T}{p_T} = 0.0011 p_T.$$

The CTC is internally divided into 9 superlayers of which five are axial and four are stereo with a 3° tilt. Figure 5.3 shows a cross sectional view of the CTC in which the superlayer structure is clearly visible. Each axial

superlayer contains 12 wire layers and adjoins a stereo layer with 6 wire layers, for a total of 84 layers containing 6156 channels. The wires within a superlayer are grouped into measurement cells which are tilted by 45° with respect to the radial direction, corresponding to the Lorentz angle of drifting electrons in combined electric and magnetic fields. The CTC is capable of a spatial resolution of 200 μm in $r-\phi$ and 4 mm in $r-z$. The detector volume is filled with the standard 50%/50% argon/ethane mixture and the wire voltages are set to provide a constant potential field of 1350 V/cm throughout the CTC.

5.2.2 The Central Calorimeters

The central calorimeters lie outside the solenoid. They are sampling calorimeters, consisting of alternating layers of an absorber, which precipitates particle showers, and scintillating material, which responds to the particle showers by emitting blue light. The light is collected in doped acrylic, wave-shifted, and directed through lightguides into photomultiplier tubes, one for each tower. The amount of light emitted, and thus the amplitude of the signal, is proportional to the number of charged secondary particles in the shower, which in turn corresponds to the energy of the incident particle. While the calorimeters cannot differentiate between individual particles, they provide a good measure of the amount and distribution of energy in jets and for neutral particles for which there is no tracking information.

The central calorimeters at CDF are composed of four semi-circular arches which are pushed together to form a barrel. The barrel is split at $z = 0$ and along the y-z plane. The arches can be rolled away from the detector to allow access to the tracking chambers during assembly and repair. An arch consists

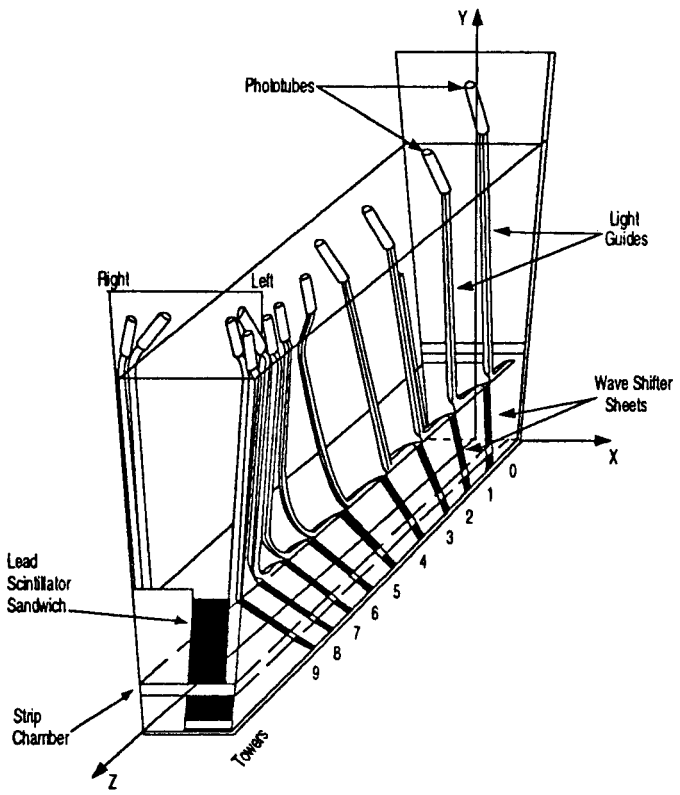

Figure 5.4: View of one wedge of the central calorimeter. The Central Electromagnetic Strip (CES) proportional chamber is embedded at shower maximum.

of 12 wedges, each covering 15° in ϕ. Each wedge is further segmented in η into 10 calorimeter towers. Figure 5.4 shows the layout of a calorimeter wedge. The towers are arranged in a projective geometry with the detector center at its hub. This geometry facilitates the reconstruction of energy distribution patterns at the event vertex, assuming it is near the nominal vertex.

The calorimeter wedges house two types of calorimeter, electromagnetic and hadronic. The electromagnetic section lies closest to the tracking. It absorbs the energies of electrons and photons, which shower relatively early

through bremsstrahlung and pair production. The thicker absorber in the hadronic calorimeter is designed to stop particles which penetrate farther into dense material. Hadrons lose their energy via nuclear cascade. Since many fewer particles are produced in a nuclear cascade than in an electromagnetic cascade, the statistical fluctuations tend to be much larger. Consequently the energy resolution is poorer for hadronic calorimeters.

The Central Electromagnetic Calorimeter (CEM)

The Central Electromagnetic Calorimeter, known as the CEM[B+88a], lies outside the solenoid. It is composed of 0.32 cm layers of lead, a high-density absorber, alternating with 0.5 cm layers of scintillating polystyrene. This combination gives good shower resolution, determined by test beam pions and electrons to be

$$\frac{\sigma_E}{E} = \frac{13.7\%}{\sqrt{E \sin\theta}} \oplus 2\%$$

(energy E in GeV) for electrons centered in towers. The overall thickness of the CEM is 18 radiation lengths. At a depth of 6 radiation lengths, where shower development reaches its maximum for electromagnetic particles, lie the Central Electromagnetic Strip (CES) chambers. These chambers determine the position and transverse profiles of showers by measuring the charge deposition on orthogonal strips and wires.

The Central Hadronic Calorimeter (CHA)

In the Central Hadronic Calorimeter, or CHA[B+88c], which adjoins the CEM in the calorimeter wedges, the absorber layers are 2.5 cm thick and made of steel. Sandwiched in between them are 1 cm layers of doped scintillating

acrylic. The total depth of the hadronic calorimeter is 4.7 absorption lengths. Its resolution, measured with test beam pions, is given by

$$\frac{\sigma_E}{E} = \frac{50\%}{\sqrt{E \sin\theta}} \oplus 3\%$$

(energy E in GeV).

The EndWall Hadronic Calorimeter (WHA)

Essentially the same type of detector as the CHA, the Endwall Hadronic Calorimeter, or WHA[B+88c], covers the range $0.9 < |\eta| < 1.3$. It also has a projective tower geometry. The calorimeter modules plug into cavities in the magnet yoke and serve as part of the flux return path. Its resolution is

$$\frac{\sigma_E}{E} = \frac{75\%}{\sqrt{E}} \oplus 4\%$$

(energy E in GeV).

5.2.3 The Muon Detectors

The Central Muon Detector (CMU)

The Central Muon Detector (CMU)[A+88d] consists of drift chambers located immediately behind the CHA, 3.47 m and 4.9 absorption lengths from the beam axis. The CMU has a pseudorapidity range $|\eta| < 0.63$. Each 15° calorimeter wedge supports a muon module which is parallel to the beam axis and spans an angle $\phi = 12.6°$ (see Figure 5.5). Consequently there is a 2.4° gap in muon coverage between wedges. In all, the CMU covers approximately 84% of the solid angle in its η range.

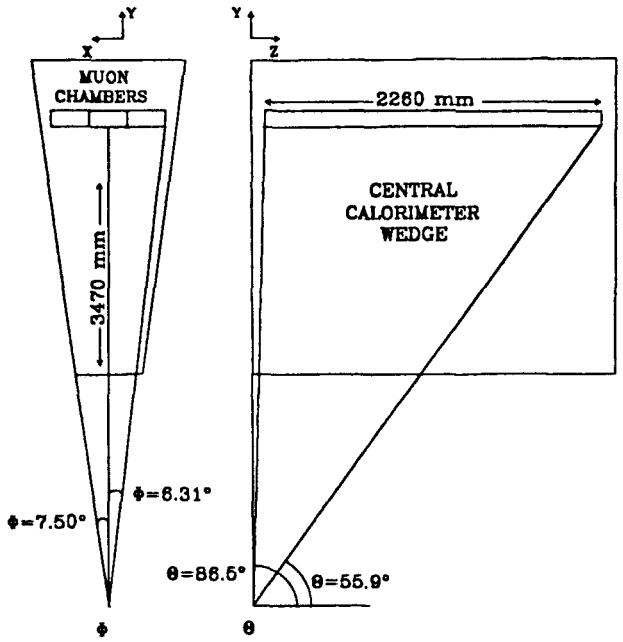

Figure 5.5: Position of the CMU in a calorimeter wedge, end-on and side views.

The muon modules are 2.26 m long and are themselves segmented in ϕ into three chambers of 4.2° each. A chamber consists of four layers of four rectangular drift cells. A 50 μm stainless steel resistive wire is located at the center of each cell. Four wires, one from each layer, make up a muon tower. Two of the wires from a muon tower, from alternating layers, lie on a radial line which passes through the nominal interaction region. The other two are offset from this line by 2 mm at the chamber midpoint (see Figure 5.6).

The CMU uses the standard argon/ethane gas mixture. Charge division is used to determine the z-position of a track along the sense wire. The two-fold ambiguity in the ϕ position of the track is resolved by determining which pair

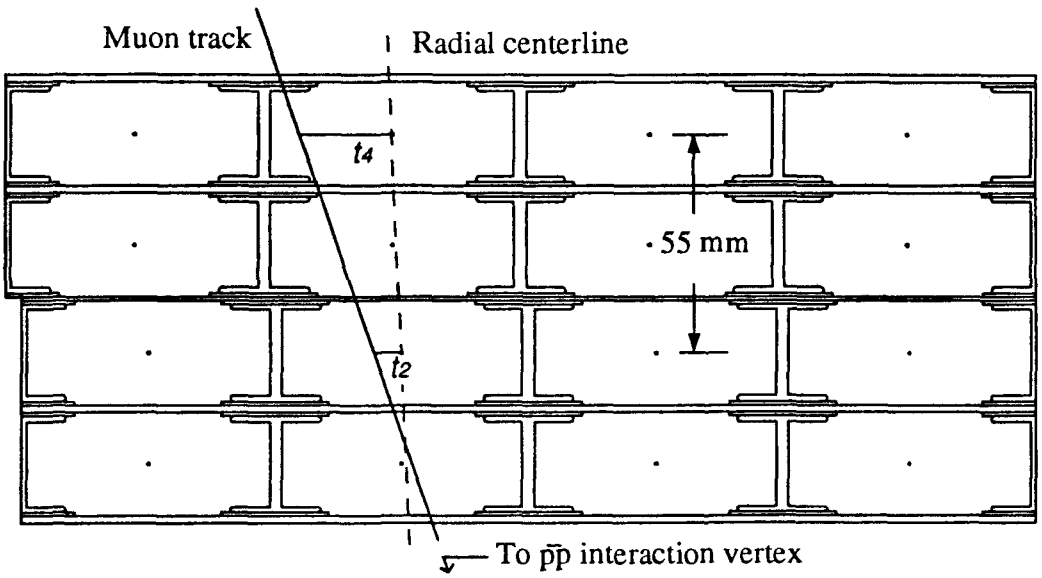

Figure 5.6: A transverse cross section of a central muon chamber.

of sense wires is hit first. Cosmic ray tests have determined the rms resolution of the muon chambers to be 1.2 mm in z and 250 μm in $r - \phi$.

The Central Muon Upgrade (CMP)

The Central Muon Upgrade, or CMP, consists of proportional wire chambers built onto steel walls 30 cm thick surrounding the central calorimeters and the CMU like a box. It was installed for the 1992 run. The purpose of the additional layer of steel between the CMU and CMP is to reduce *punch-through*. Punch-through occurs when high-energy hadronic jets manage to traverse the calorimeters and cause hits in the CMU. The extra steel acts as an absorber, stopping all but 0.6% of $K^{\pm}$ and $\pi^{\pm}$ particles from reaching the CMP.

The CMP chambers are long cells similar in design to the CMU. The rela-

tive offset of the alternating cell layers is half a cell width. There is no charge information available for CMP hits, so that the track position can be determined in the x-y plane only. The CMP covers about 63% of the solid angle in its η range. 53% of the solid angle for this range is covered by both the CMU and CMP[A+94a].

The Central Muon Extension (CMX)

The Central Muon Extension, or CMX, is composed of four free-standing conical arches, one at each of the four corners of the CDF. The CMX provides coverage of about 71% of the solid angle in the region $0.6 < |\eta| < 1.0$, with some gaps in ϕ necessitated by its peculiar design. The arches are lined with four layers of proportional wire chambers which supply track position information; timing information is given by two layers of scintillator counters, whose light is collected in phototubes mounted on the edges of the arches.

5.3 The Plug Region

The Plug, or Endplug, detectors are named for their distinctive shape. They fit neatly into the 30° recesses at the ends of the CDF, butting up against the CTC face and filling the gap in the projective endwall structure. Each plug covers the pseudorapidity range $1.1 < |\eta| < 2.4$. The plug is a gas-gain calorimeter, using 50%/50% argon-ethane as its active medium.

5.3.1 The Plug Electromagnetic Calorimeter (PEM)

Each Plug Electromagnetic Calorimeter (PEM)[F+88b] is a disk-shaped detector with a diameter of 2.8 m and a depth of 53 cm. A concentric conical

10° hole through the middle accomodates the beampipe. The calorimeter is composed of 34 layers of proportional tube arrays alternating with layers of lead absorber 0.27 cm thick. The layers are grouped longitudinally into three projective towers. The proportional tubes are arranged in such a way as to provide a radial geometry in the x-y plane, with segmentation in ϕ of 5°. The readout is provided by cathode pads etched onto the copper plating facing the proportional tube array. In the central tower, strips along the ϕ and radial directions provide additional readout. The pads are more finely segmented at shower maximum, allowing for a precision determination of the shower profiles. The thickness of the PEM ranges from 18 to 21 radiation lengths, increasing somewhat with decreasing $|\eta|$. The PEM resolution was determined to be

$$\frac{\sigma_E}{E} = \frac{28\%}{\sqrt{E}} \oplus 2\%$$

(E in GeV) using 100 GeV test beam electrons.

5.3.2 The Plug Hadronic Calorimeter (PHA)

The cone-shaped Plug Hadronic Calorimeter, or PHA[A+88a], is located right behind the PEM. It is segmented in a similar fashion. The absorber is steel in 5.1 cm layers, alternating with layers of proportional tube chambers with cathode pad readouts. The resolution of the PHA, determined at the test beam, is

$$\frac{\sigma_E}{E} \approx \frac{90\%}{\sqrt{E}} \oplus 4\%.$$

5.4 The Forward Region

The forward detectors of the CDF are physically separated from the main detector and are permanently fixed in the collision hall. They cover the pseudorapidity range 2.2< $|\eta|$ <4.2.

5.4.1 The Forward Electromagnetic Calorimeter (FEM)

The Forward Electromagnetic Calorimeter, or FEM[B+88d], is located approximately 6.5 m in z from the detector center. It is composed of 30 sampling layers of proportional tube chambers with cathode pad readouts, alternating with 0.48 cm-thick layers of absorber made of 94% lead/6% antimony alloy. Here, too, the towers are projective, covering 0.1 in η and 5° in ϕ. The FEM has a thickness of 25.5 radiation lengths. Its energy response is linear up to 160 GeV. Its resolution is

$$\frac{\sigma_E}{E} \approx \frac{25\%}{\sqrt{E}} \oplus 2\%$$

(E in GeV).

5.4.2 The Forward Hadronic Calorimeter (FHA)

The Forward Hadronic Calorimeter, or FHA[C+88], is behind the FEM. It has 27 sampling layers of proportional tube chambers with cathode pad readouts, alternating with 5.1 cm layers of steel absorber. The FHA energy resolution is given by

$$\frac{\sigma_E}{E} \approx \frac{130\%}{\sqrt{E}} \oplus 4\%.$$

5.4.3 The Forward Muon System (FMU)

The Forward Muon System, or FMU[B+88e], consists of two 1 m-thick magnetized steel toroids, massing 395 tons, sandwiched between three sets of drift chambers. The toroids produce a field ranging from 2.0 Tesla at their inner radius of 0.5 m to 1.6 Tesla at a radius of 3.8 m. This field bends the muon's trajectory, allowing for a measurement of its momentum. The drift chambers are segmented into 24 15° ϕ wedges. The chambers are staggered with respect to their neighbors to eliminate detector dead spots at wedge boundaries. Each chamber supports two planes of drift cells, the "coordinate plane", nearest the collision point and composed of 56 cells, and the "ambiguity plane", consisting of 40 cells, which is staggered with respect to the coordinate plane to resolve the left-right ambiguity of a particle track. The two sides of a chamber share a common cathode plane. Each cell contains a 63 μm stainless steel anode wire strung along the chord of a wedge. This wire provides a polar angle measurement of a muon track with a resolution of 130 μm. The overall momentum resolution of the FMU is 13%. The gas used in the FMU is a 50%/50% argon-ethene mixture.

5.5 Summary

The central tracking system, the calorimeters, and the muon chambers are instruments which aid us in our understanding of the nature of high energy events. The detectors collect information. To separate the interesting information from the chaff, we rely on a trigger system that determines which events are recorded for further processing and study.

Chapter 6

The Trigger

It would be an impossible task to record and process all the information provided by the complex detectors that make up CDF. Bunch crossings at the Tevatron occur about 286,000 times per second, but not every crossing results in a hard scattering process. To pick out the events likely to be of interest to the various analyses done at CDF, a three-level trigger system is used. The first two levels[A+88b] consist of specially designed programmable FASTBUS-based hardware and are responsible for the decision to initiate a full detector readout. Level 3 is a software trigger. Each level is a logical OR of a set of triggers designed to identify events containing electrons, jets, muons, or an imbalance of energy indicating the possible presence of a neutrino. For each successive level the trigger decision is based on more complex information from the front-end detector readouts, and consequently takes more time. The goal is to maximize the efficiency of the triggers while minimizing the detector dead time.

6.1 Level 1

To streamline the triggering process, the calorimeters and muon chambers have two types of output. The first, called "fast-out," provides analog information for immediate use. The other is for temporary front-end data storage pending a trigger decision. For the muon system, the fast-out indicates the presence of a track stub (at least 2 of 4 possible hits in a muon tower). The transverse momentum, $p_T = p\sin\theta$, is roughly calculated using the track angle in the chambers, and Level 1 applies a cut at 3.3 GeV/c[A^+88e]. In the calorimeters the transverse energy $E_T = E\sin\theta$ deposited in the EM and HAD components is summed into *trigger towers* of $\Delta\eta = 0.2$ and $\Delta\phi = 15°$. Each trigger tower is composed of two calorimeter towers. The trigger towers convey their energy sum information via the fast-out cables to the trigger electronics. The total E_T deposited in the EM and HAD trigger towers is compared to programmable threshold values at Level 1. This information is combined with the muon fast-outs and the BBC coincidence to reach a Level 1 decision, which is made by the final decision logic board in the trigger room.

If the event fails the requirements for a Level 1 accept, a clear-and-strobe signal is sent to the detector to clear the buffers of data and to wait for the next event. If the event passes Level 1 requirements, the decision logic relays a signal to inhibit the reset of the front-end detector electronics. The event information is then passed on to Level 2 for closer examination. All this takes place within the 3.5 μs interval between bunch crossings and incurs no dead time. The Level 1 accept rate at an instantaneous luminosity of $\mathcal{L} = 5 \times 10^{30}$ $cm^{-2}s^{-1}$ is about 1 kHz.

6.2 Level 2

Detector readout continues while Level 1 is processing the fast-out signals, so that Level 2 has use of much more detailed information to make its decision. Since the processing is more complex, detector dead time of about 10% is incurred at Level 2; a typical trigger decision takes about 10 μs.

In the calorimeters, energies are clustered using a nearest-neighbor hardware cluster-finder. For example, the minimum trigger tower E_T necessary to initiate an electron cluster search is 3 GeV. Additional "shoulder" tower energies are added to this "cluster seed" tower if they have $E_T > 0.1$ GeV. The E_T, ϕ, and η of all the observed clusters are recorded. Muon track stub information becomes available from the central muon detectors. The CTC relays fast timing information to a hardware track processor called the Central Fast Tracker, or CFT[F+88a]. The CFT uses this input to reconstruct stiff tracks in the $r - \phi$ plane with a resolution of

$$\frac{\delta p_T}{p_T} \approx 0.035 p_T.$$

Its efficiency is 93.5 $\pm$ 0.3% for tracks with p_T >10 GeV/c. The reconstructed CFT tracks can be matched to the track stubs in the muon chambers to identify muon candidates, or to highly electromagnetic clusters in the calorimeters to identify electron candidates. The Level 2 accept rate at an instantaneous luminosity of $\mathcal{L} = 5 \times 10^{30}$ cm^{-2}s^{-1} is about 12 Hz.

6.3 Level 3

The Level 3 trigger consists of the same software reconstruction algorithms that are used later in offline analyses, except that the offline database constants

are subject to change as calibrations are updated. Level 3 processes events passing Level 2 using Silicon Graphics multi-cpu Power Servers. Most of the execution time is used for full three-dimensional track reconstruction in the CTC, which provides accurate momentum information for muon, electron and jet identification. Level 3 is used to sort the data by triggers into datasets for use in specific offline analyses (*e.g.*, inclusive electrons, inclusive muons, dijet events). The events are written to magnetic tape at a rate of 5–6 Hz for subsequent offline processing.

Chapter 7

Analysis of the Data

7.1 Introduction

Recent runs at the Tevatron collider have yielded 106 pb^{-1} of $\bar{p}p$ data at $\sqrt{s} = 1.8$ TeV recorded by the CDF detector. From these data we extract 6708 $Z \rightarrow e^+e^-$ events, to date the largest Z^0 sample available from hadron collisions. Using this event sample, we measure the cross sections for Z^0 production as a function of associated hadronic jet multiplicity, and study the kinematic properties of the jets produced in association with the Z^0.

In this chapter we present a detailed description of the method used to calculate the cross sections (Section 7.2). We discuss how we select our data sample (Sections 7.3 and 7.4), measure the acceptances (Section 7.6.1) and the efficiencies (Section 7.6.2), and determine the backgrounds (Section 7.6.3). The final cross section results are presented and compared to QCD predictions in Chapter 9. Also presented there is a comparison between fully reconstructed QCD jet differential spectra and the differential spectra obtained in the data.

7.2 Overview of the Cross Section Measurement

To measure a cross section for a given process precisely, one must understand the detector used to identify the events used in the analysis, and the data sample itself (*i.e.*, efficiencies and backgrounds). Because of the nature of the $\overline{p}p$ interaction and the imperfection of the detector, not to mention human imperfection, all the factors involved in the measurement of a cross section come with an associated systematic uncertainty which reflects how far we are willing to trust the numbers we use.

For $Z \rightarrow e^+e^- + \geq N$ jet events, the standard cross section determination, which we will call the direct method, is given by the equation

$$\mathrm{B}(Z \rightarrow e^+e^-)\sigma(Z+ \geq N \text{ jets}) = \frac{N_N(Z+DY)}{\epsilon_{\mathrm{vertex}} \int \mathcal{L}dt} \times \frac{F_Z}{\epsilon_{\mathrm{mass}}}. \qquad (7.1)$$

$N_N(Z+DY)$ is the number of Z^0 and Drell-Yan e^+e^- events with $\geq N$ jets, $|z_{\mathrm{vertex}}| < 60$ cm and $76 < M_{ee} < 106$ GeV/c^2 (see Figure 7.1 for the vertex and invariant mass distributions of the Z^0); $\epsilon_{\mathrm{vertex}}$ is the efficiency of the vertex cut; ϵ_{mass} is the efficiency of the mass window cut; $F_Z = N_Z/(N_Z + N_{DY})$ is the fraction of Z^0s within the mass window; and $\int \mathcal{L}dt$ is the integrated luminosity of the data sample. Systematic and statistical errors in any one of these factors will influence the final cross section number. Unfortunately the reduction of a systematic errors is not always possible.

Equation 7.1 contains factors which are independent of the number of jets in the event, such as the luminosity and $\epsilon_{\mathrm{vertex}}$. If, instead of calculating the cross section for each jet multiplicity separately using the direct method, we make use of a previous measurement of an inclusive Z^0 cross section to obtain *relative*

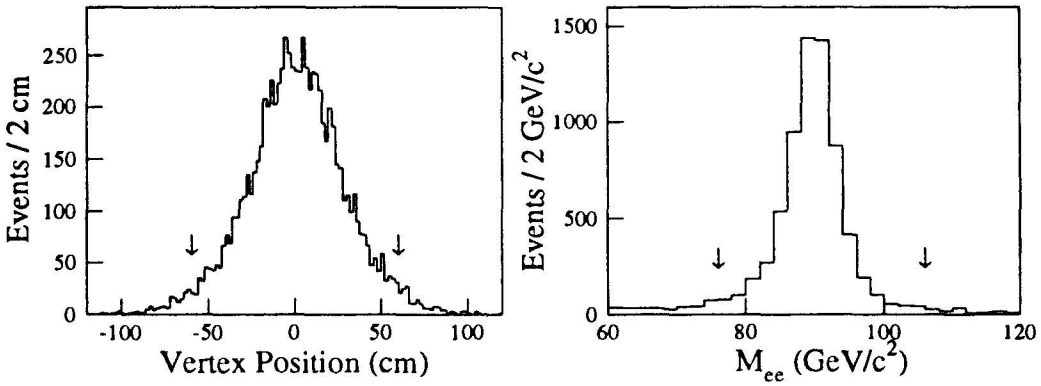

Figure 7.1: The Z^0 vertex distribution and invariant mass of the Z^0 .

$Z^0 + N$ jet cross sections, many of these common factors cancel in the ratio. Any large systematic uncertainties on those factors no longer influence the cross section, except insofar as they are included in the inclusive cross section measurement. We refer to this method as the ratio method, and we use it in our analysis to obtain cross sections with reduced systematic errors. The inclusive cross section of 231 $\pm$ 12 pb for $Z \rightarrow e^+e^-$ is taken from Reference [A$^+$95c]. We obtain the $Z^0 + N$ jet cross section using the ratio method equation:

$$BR \times \sigma(Z+ \geq N \text{ jets}) = \frac{N_N(Z+DY)}{N_0(Z+DY)} BR \times \sigma_{\text{incl}}(Z). \qquad (7.2)$$

If we define $M_N(Z + DY)$ to be the total number of events in each $Z^0 + N$ jet sample after our selection cuts, then

$$N_N(Z+DY) = \frac{M_N(Z+DY) - B_N}{[A_{geom} \cdot A_{kin} \cdot A_{\text{overlap}}]_N \times [\epsilon_{ID} \cdot \epsilon_{trig}]_N}. \qquad (7.3)$$

Here, B_N is the non-Drell Yan background in the data sample, A_{geom}, A_{kin}, and

A_{overlap} are the geometric, kinematic, and lepton-jet overlap acceptances, and ϵ_{ID} and ϵ_{trig} are the efficiencies of the electron selection cuts and the electron trigger, respectively.

7.3 Selection of Z^0 Events

Among the numerous possible decays of the Z^0, the easiest to identify and separate from probable backgrounds are the decays into the charged leptons, electrons and muons. The combined branching fractions of these decays make up only 6.7% of the total width of the Z^0 [Par94]; however, unlike the hadronic decays, which are swamped by huge QCD backgrounds, the leptonic decays are clean and have characteristic signatures which are immediately recognizable. Since it is the purpose of this analysis to extract a cross section for Z^0 production based on the multiplicity of associated hadronic jets, it is important to start with a good Z^0 sample in which hadronic backgrounds are minimal. We have chosen to study the $Z \rightarrow e^+e^-$ decay here. To obtain a clean data sample we require that the decay products of the Z^0 pass stringent quality cuts.

7.3.1 Online Electron Candidate Selection

An electron passing through the detector leaves in its wake a series of characteristic signatures, which are used to determine its quality. At CDF, the signatures one expects to find are a track through at least one of the tracking systems and a well-collimated deposition of electromagnetic energy in a calorimeter. The Level 2 hardware trigger at CDF begins the process of electron identification which is refined in Level 3 and in offline analyses.

An electron cluster consists of a "seed tower" of at least 3 GeV transverse energy, and "shoulder towers" which must have a minimum of 0.1 GeV E_T. Shoulder towers adjacent to the seed tower are incorporated into the cluster until there are no more eligible shoulder towers or until the maximum cluster size has been reached. The maximum cluster size differs from detector to detector; for the central region it is restricted to three towers in η ($\Delta\eta = 0.3$) by one tower in ϕ ($\Delta\phi = 15°$); in the plug, to five η towers by five ϕ towers ($\Delta\eta \times \Delta\phi = 0.5 \times 25°$), and in the forward, to seven η towers by seven ϕ towers ($\Delta\eta \times \Delta\phi = 0.7 \times 35°$). An electron cluster must have an EM E_T of at least 5 GeV, and a ratio of hadronic to electromagnetic E_T (or *HAD/EM*) of less than 0.125[1].

At Level 2, the various electron triggers have different criteria for passing electron cluster candidates, such as different E_T thresholds, minimum track p_T requirements, etc. The events which satisfy any of the Level 2 requirements feed into the Level 3 trigger, from which the final "Inclusive Electron" data set emerges. This set is used in the offline analysis for the final electron event selection.

We require that the events in our final data sample have passed one of the Level 2 and one of the Level 3 *central electron* triggers. Because of the large number of available central electron triggers at CDF, and the correspondingly wide range of individual trigger cuts, this requirement is very loose. The central electron trigger efficiency is discussed in Section 7.6.2.

[1]If $E_T > 100$ GeV, no *HAD/EM* cut is imposed.

7.3.2 Offline Electron and Z^0 Selection

At CDF, good tracking resolution is available only for centrally produced (*i.e.*, transverse) particles. Therefore, the first step in the selection of a clean Z^0 sample is the requirement that one electron from the Z^0 decay be central, within the pseudorapidity range $|\eta| < 1.1$.

Since the knowledge of the mass of the Z^0 provides an additional constraint, it is unnecessary to cut equally tightly on both electrons from the Z^0 . This is useful because it opens up the bulk of the detector fiducial volume to the second electron, increasing the statistics with a relatively small sacrifice in event purity. Since the first electron is always central, the resulting Z^0 dataset can be divided into three categories: the central-central (CC), central-plug (CP), and central-forward (CF) samples.

The cuts imposed on the primary electron are:

- in central calorimeter fiducial volume
- corrected transverse energy $E_T \geq 20$ GeV
- transverse momentum $p_T \geq 13$ GeV/c
- $|z_{vert}| \leq 60.0$ cm
- $HAD/EM \leq 0.055 + 0.00045 \cdot E$
- Isolation(0.4) ≤ 0.1
- $0.5 \leq E/p \leq 2.0$
- $L_{shr} \leq 0.2$
- $\chi^2_{str} \leq 10.0$

- $|\Delta x| \leq 1.5$ cm (track matching cut)
- $|\Delta z| \leq 3.0$ cm (track matching cut)
- conversions removed

A description of these cuts is given below.

Fiducial Volume Cut The electron fiducial volume of the CDF detector is determined from the calorimeter regions for which the electromagnetic energy response is relatively flat. This means that regions near detector cracks and at the edges of modules, and any other uninstrumented areas, are not considered to be within the fiducial volume. Similarly, any regions in which the detector readout was inhibited for any reason are also considered non-fiducial for the affected periods of data-taking.

In the central region, the Central Electromagnetic Strip (CES) shower position of a electron must be within 21 cm of the tower center in the transverse view. This ensures that the shower is fully contained in an active medium. Excluded regions are $|\eta| < 0.05$, where the detector halves join; $0.77 < |\eta| < 1.0$ and $75° < \phi < 90°$, where the cryogenic connections to the solenoid (also referred to as "the chimney") are mounted; and $1.05 < |\eta| < 1.1$, where the depth of the EM calorimeter is small. The fiducial coverage of the central region, defined as $|\eta| < 1.1$, is about 78.9%.

In the plug and forward regions, an electron seed tower must be at least 5° from the quadrant borders. The areas of overlap between detector regions, given by $1.1 < |\eta| < 1.2$ and $2.2 < |\eta| < 2.4$, are excluded, as is the portion of the forward given by $3.6 < |\eta| < 4.2$. The total fiducial coverage of the

CDF detector up to $|\eta| = 3.6$ is 78.5%. Within this volume additional cuts determine the quality of electron candidates.

Electron Transverse Energy and Momentum Cuts The transverse energy and momentum are defined by $E_T = E \sin\theta$ and $p_T = p \sin\theta$. The energy is measured in the calorimeters and is corrected for non-linearities and time- and η-dependent changes in response. The momentum is obtained from the track curvature in the CTC. A track is required so that electromagnetic clusters arising from photon hits, or from the decay $\pi^0 \rightarrow \gamma\gamma$, for example, are not mistakenly identified as electrons.

Vertex Requirement When the electron track is extrapolated back to the beam, the event vertex can be determined. Normally primary event vertices are clustered near the center of the detector with a $\sigma = 30$ cm (see Figure 7.1a.). Events with vertices falling more than $2\sigma = 60$ cm from the nominal collision point at $z = 0$ are removed from consideration.

Electron *HAD/EM* Energy Fraction Electron showers are generally completely contained within the electromagnetic calorimeter, whereas hadronic jets, for example, deposit larger fractions of their energies in the hadronic calorimeter. One way to distinguish between real electrons and tightly collimated hadronic jets is to cut on the fraction of hadronic to electromagnetic energy (*HAD/EM*) in the cluster. Since the "leakage" of electron energy into the HAD calorimeter increases with energy, the cut imposed is a sliding cut. In general, we require that the HAD E_T be less than about 5.5% of the EM E_T for a good electron candidate. The left side of Figure 7.2 shows the *HAD/EM*

spectrum for central electrons to which all the tight cuts except the *HAD/EM* have been applied and for electrons from Z^0 decays passing all the Z^0 selection cuts except the *HAD/EM* cut.

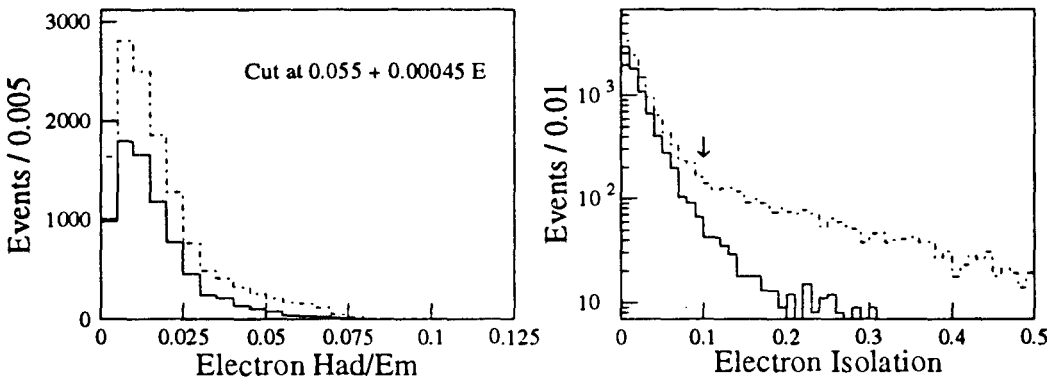

Figure 7.2: *HAD/EM* distribution and isolation distribution for central electrons. The dashed line shows the spectra for inclusive central electrons; the solid line shows those for electrons from Z^0 decay.

Electron Isolation One way to distinguish between electrons from heavy boson decay and electrons from other processes or jets is to require that the candidate be isolated. Isolation is defined as

$$I(0.4) = \frac{{E_T}^{0.4} - E_T}{E_T},$$

where E_T is the transverse energy of the cluster and ${E_T}^{0.4}$ is the total transverse energy contained within a cone of radius $R = 0.4$ about the cluster. The radius is defined in $\eta - \phi$ space as $R = \sqrt{\Delta\eta^2 + \Delta\phi^2}$. A low isolation value indicates that the electron was produced away from hadronic activity, which is expected

for the products of Z^0 decay. The right side of Figure 7.2 shows the isolation spectrum for central electrons passing all but the isolation cut, and for electrons from Z^0 decays.

Electron E/P Since an electron has negligible mass, its momentum and energy should agree well. Small differences between the two may arise due to *bremsstrahlung* as the electron passes through the CTC material, or to mismeasurement of the energy due to cracks in the calorimeter. The ratio E/p is required to be in the range $0.5 < E/p < 2.0$ to eliminate neutral pion photonic decays.

Electron Shower Shapes (L_{shr} and χ^2_{str}) There are several variables which indicate the degree to which an electron cluster conforms with the expected cluster shape determined in test beam runs. One of these, L_{shr}, represents a χ^2 comparison of the transverse profile of a given cluster with a "template" from test beam data. The transverse profile is a measure of the lateral sharing of energy among adjacent cluster towers. L_{shr} is defined as

$$L_{shr} = 0.14 \cdot \sum_i \frac{E_i^{adj} - E_i^{exp}}{\sqrt{(0.14)^2 \cdot E + (\sigma E_i^{exp})^2}},$$

where E_i^{adj} refers to the energy in a tower adjacent to the seed tower, E_i^{exp} is the expected energy in that tower, $0.14\sqrt{E}$ is the error on the measured energy and σE_i^{exp} is the error on the expected energy. E_i^{exp} is determined from a test beam shower profile parametrization. Another variable, χ^2_{str}, is a χ^2 comparison between the measured pulse height shape in z in the CES and the equivalent shape from test beam data. Cuts on χ^2_{str} and L_{shr} ensure that the electron candidates exhibit the characteristics of their test beam counterparts.

Electron Track Position Matching (Δx and Δz) When the highest-momentum CTC track pointing to an electron cluster is extrapolated to the cluster, its position in the Central Electromagnetic Strip (CES) chamber, which is embedded in the central EM calorimeter at shower maximum, can be compared to the measured CES shower position to obtain the track-matching variables Δx and Δz. Here, Δx is the separation between extrapolated track and CES cluster position in the $r - \phi$ view; Δz is the equivalent separation in the z direction. Requiring close agreement between track and shower positions reduces backgrounds from overlapping charged and neutral hadrons. Figure 7.3 shows the Δx and Δz distributions for the inclusive central electron sample and for electrons from Z^0 decay, where all cuts have been applied except the Δx and Δz cuts.

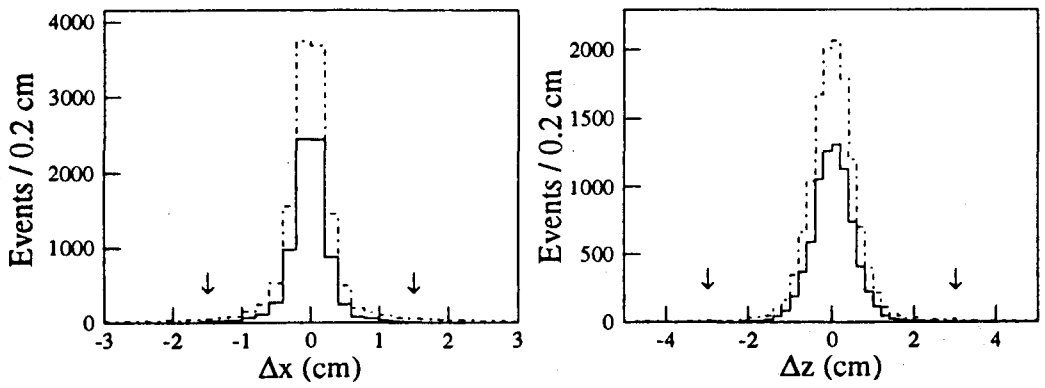

Figure 7.3: Δx and Δz track matching distributions for inclusive central electrons (dashed line) and for electrons from Z^0 decay.

Conversion Electron Removal After applying all of the above quality cuts one can be fairly certain that one is dealing with an electron. However, the possibility remains that the electron is not prompt. One of the major sources of non-prompt electrons is pair-production, which stems from the interaction of a photon with the material in the tracking chambers. This is referred to as a "conversion." Conversions are identified by searching for electrons which have no associated track in the VTX and for which an oppositely charged track lies nearby within the CTC volume. If these criteria are met by an electron candidate it is removed from the event sample.

The sample of events that survives the tight primary electron cuts is referred to as the "good central electron" set to differentiate it from the inclusive electron sample. The Z^0 sample is a subset of the good central electron events in which there is an additional electron passing the following less stringent requirements:

- in central calorimeter fiducial volume
- corrected transverse energy $E_T \geq 20$ GeV
- $HAD/EM \leq 0.125$
- Isolation(0.4) ≤ 0.1
- conversions removed

or

- in plug calorimeter fiducial volume

- corrected transverse energy $E_T \geq 15$ GeV [2]
- Isolation(0.4) ≤ 0.1
- $\chi^2_{3\times3} \leq 3.0$
- conversions removed

or

- in forward calorimeter fiducial volume
- corrected transverse energy $E_T \geq 10$ GeV
- Isolation(0.4) ≤ 0.1.

Plug Electron Shower Profile $\chi^2_{3\times3}$ $\chi^2_{3\times3}$ is a plug electron variable analogous to χ^2_{str} in the central region. It is a χ^2 fit to test beam data for lateral energy sharing in a cluster of 3 towers in η by 3 towers in ϕ.

If the charges of the two electrons are well-measured, *i.e.*, if the tracking is good for the regions in question, they must have opposite signs. Finally, the invariant mass of the electron pair must lie within the mass window given by 76 GeV/c^2 $< M_{ee} <$ 106 GeV/c^2. The resulting $Z \rightarrow e^+e^-$ dataset used in this analysis contains 6708 events. In Table 7.1 we list the events divided up by type (CC, CP, CF) before and after the invariant mass cut is applied. Figure 7.4 shows the final invariant mass distributions for the three cases. In Figure 7.5 we present the transverse momentum distribution of the Z^0 events.

[2]The energy corrections for the plug and forward electrons are based on scales set using central-plug and central-forward $Z \rightarrow e^+e^-$ decays, where the Z^0 mass was reconstructed to be 91.18 GeV/c^2.

Table 7.1: Distribution of Z^0 events among detector types.

Mass Cut	CC	CP	CF	All Z^0 Events
$M_{e^+e^-} > 50$ GeV/c^2	3263	3405	699	7367
$76 < M_Z < 106$ GeV/c^2	2952	3127	629	6708

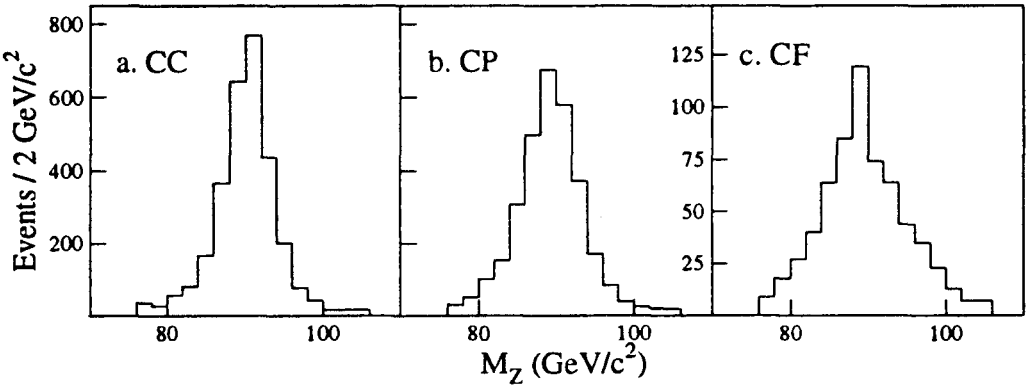

Figure 7.4: The Z^0 invariant mass in a.) central-central, b.) central-plug, and c.) central-forward Z^0 events.

7.4 Jets in the $Z \rightarrow e^+e^-$ Sample

The $Z \rightarrow e^+e^-$ dataset selected in Section 7.3 is an inclusive set that includes all reconstructed Z^0 bosons regardless of the number of associated jets. The next paragraphs describe how jets are clustered, corrected, and selected in the Z^0 sample, and how jet-counting systematic uncertainties are determined for the resulting multiplicities.

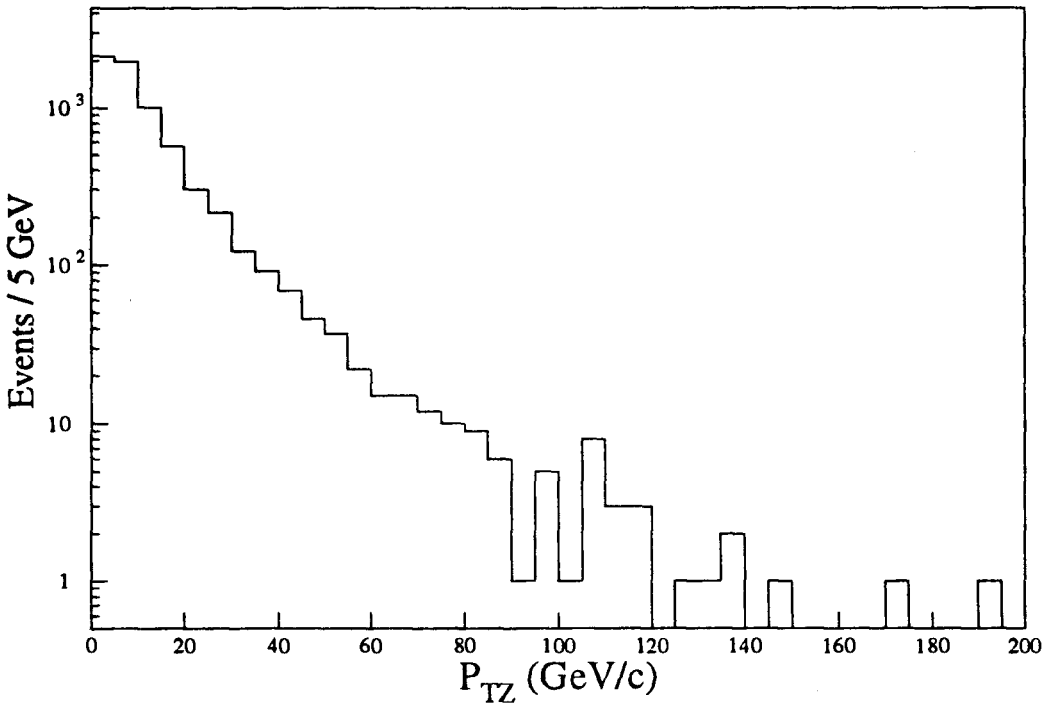

Figure 7.5: The transverse momentum distribution of the $Z \rightarrow e^+e^-$ events.

7.4.1 Jet Clustering

Jets are clustered in the CDF calorimeters starting with "seed towers" of at least 1 GeV transverse energy. These towers span 15° in ϕ, so in the plug region three physical towers are grouped together to form a clustering tower. Contiguous seed towers are ganged together to form preclusters. If a tower is outside the 7×7 window surrounding the seed, it is used to form a new precluster. Electromagnetic and hadronic energies are summed separately.

The jet-finding algorithm finds the E_T-weighted centroid of the precluster and forms a cone in $\eta - \phi$ space around it. The cone can have a radius of

$R_j = \sqrt{\Delta\eta^2 + \Delta\phi^2} = 0.4$, 0.7, or 1.0. In this analysis, we use $R_j = 0.4$. Inside the cone, the algorithm searches for towers with $E_T > 100$ MeV whose centroids lie within R_j, and adds their energies to the cluster. When this phase is completed, a new E_T-weighted centroid is computed for the cluster, a cone of R_j is formed about it, and the whole process is repeated. This continues until the list of towers within the cone remains stable.

A description of the jet-clustering algorithm as well as a discussion of the use of different cone sizes can be found in Reference [A+92].

7.4.2 Jet Energy Corrections

The uncorrected energies of the jets identified by the clustering algorithm are simply the raw calorimeter energies. They can be very different from the energies of the initial parton before fragmentation, for several reasons. A few of the differences arise from fundamental physics processes; others are the result of the inherent limitations of the detector. Some of the sources of jet energy uncertainties are given below.

- Energy not associated with the hard-scattering process, called "underlying event energy," is included within the clustering cone.
- Some spreading of the jet due to fragmentation may push particles out of the clustering cone. Their energy is referred to as "out-of-cone" energy.
- Muons and neutrinos in the jet interact little or not at all with the calorimeter medium; their energies are unaccounted for.
- Jets may strike regions of the detector with degraded response, such as module boundaries and overlap areas between detector subsytems,

causing an underestimate of their energies.

- The response of the calorimeter is nonlinear at low energies ($E_T < 10$ GeV)[A+92].

- Because of the magnetic field in the tracking volume, a particle with $p_T < 400$ MeV does not reach the calorimeters. The field bends the trajectories of particles with slightly higher momenta enough so that they may fall outside the jet cone.

Jet energies at CDF are corrected with a special routine which takes into account these effects[KF91, Ton93]. The correction utilizes a map of the detector response which is a function of the η and E_T of the jets. In the central region this response map is generated with the aid of CTC[3] momentum determinations. Extensions of the map to the regions where tracking is not available are made using jet-balancing techniques, where the E_T of central jets is required to balance the E_T of jets in the plug and forward regions.

Recently the jet correction routine has been augmented to include the effects of additional interactions[Ton93], which become significant at high instantaneous luminosities. The average energies contributed for a given cone size by these extra interaction vertices are determined from a study of minimum bias events. The resulting (luminosity, cone size, extra vertex) matrix contains constants which are combined with an overall underlying event energy scale factor to yield the excess energy per jet. The routine subtracts the excess energy on an event-by-event basis.

The overall effect of the jet corrections on jet energies is shown in Figure 7.6.

[3]Central Tracking Chamber

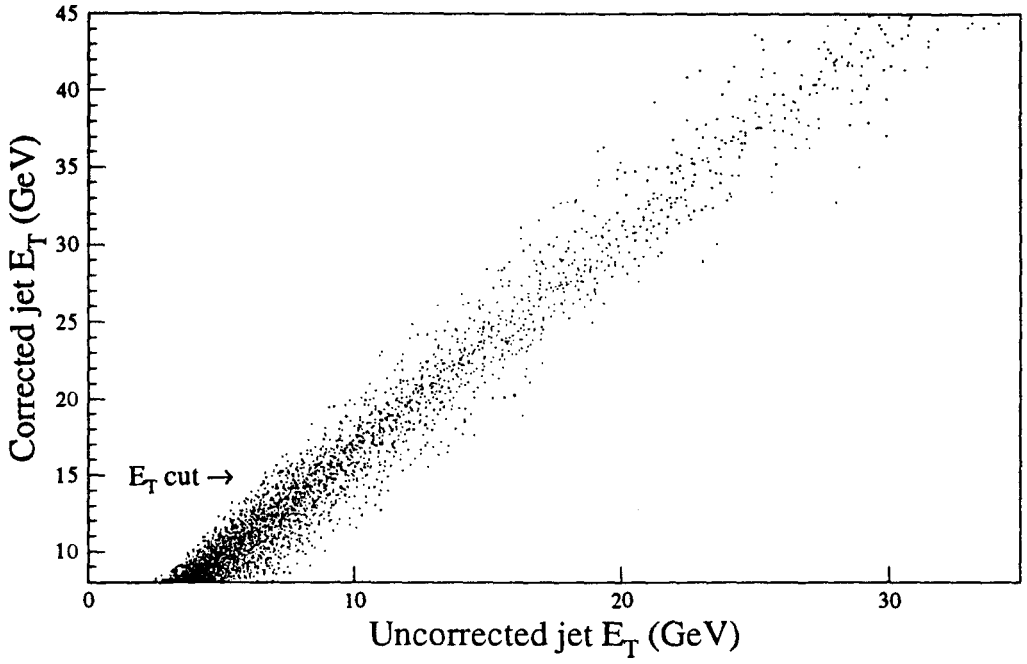

Figure 7.6: Scatterplot of corrected versus uncorrected jet E_T.

7.4.3 Jet Selection

Within our Z^0 event sample we look for events containing jets. To differentiate real hadronic jets from the smaller showers and underlying event phenomena typical to high-p_T interactions, we require the jet clusters to pass cuts on their position and energy. Initially we select jet objects which have at least 12 GeV corrected E_T and lie within $|\eta_d| < 2.4$, where η_d is the η measured with respect to the detector center at $z = 0$. We demand that any two of the jets passing these cuts be separated by a distance $\Delta R_{jj} > 1.3 \cdot R_j$. The factor 1.3 was determined in jet-mixing studies to describe the separation at which $\simeq 90\%$ of all $R = 0.7$ jet pairs were resolved[A+92]. We use this same factor for our

0.4-clustered jets.

If the minimum separation is not achieved, the two jets are merged, their energies are combined, and their weighted average position is taken to be the position of the new jet. When this process is completed, we impose the final jet cuts:

- E_{Tj} (corrected) > 15 GeV
- $|\eta_d| < 2.4$.

Jets that pass these cuts are considered "good" jets and contribute to the "jet multiplicity" of a given event. We call the Z^0 event samples with $\geq N$ jets, where $N = 0$, 1, 2, 3, and 4, *inclusive jet multiplicity* samples. Samples with exactly N jets constitute *exclusive jet multiplicity* samples. Because the inclusive multiplicities are the ones we require for our ratio-method cross section determination, the words "jet multiplicity" in the remainder of this analysis will refer to *inclusive* multiplicity unless otherwise stated. Table 7.2 shows both the inclusive and exclusive multiplicities for our Z^0 event sample. The exclusive jet multiplicity distribution is shown in Figure 7.7.

7.4.4 Jet Counting Uncertainties

Because of the uncertainties in the details of the detector response to jets due to the jet energy scale, detector η boundaries, etc., and because of the effects of the underlying event energy and energy which comes from possible additional vertices in the event, there are various systematic uncertainties associated with jet counting. We divide the sources of these uncertainties up into two broad categories: 1) systematics arising from the jet selection cuts and from the

Table 7.2: Jet Multiplicities Associated with Z^0 Production

Event Sample	N_Z	Fraction
$Z + 0$ jets	5402	0.8053
$Z + 1$ jet	1025	0.1528
$Z + 2$ jets	224	0.0334
$Z + 3$ jets	46	0.0069
$Z + 4$ jets	6	0.0009
$Z + 5$ jets	3	0.0004
$Z + 6$ jets	1	0.0001
$Z + 7$ jets	1	0.0001
$Z+ \geq 0$ jets	6708	1.0000
$Z+ \geq 1$ jet	1306	0.1947
$Z+ \geq 2$ jets	281	0.0419
$Z+ \geq 3$ jets	57	0.0085
$Z+ \geq 4$ jets	11	0.0016
Total	6708	1.0000

underlying event corrections, and 2) systematics due to additional interaction vertices not associated with the Z^0 production vertex.

To estimate the jet counting uncertainty due to our selection cuts, we vary the cuts imposed on the jet sample as follows:

- E_{Tj} (corrected) > 15 GeV $\pm$ 0.75 GeV
- $|\eta_d| < 2.4 \pm 0.2$
- underlying event absolute energy scale factor: $\pm 50\%$

and redetermine the jet multiplicities. Of these variations the variation in the E_T requirement contributes by far the most to the jet counting uncertainty.

The determination of the jet counting uncertainties due to additional interactions in the event is more complex. We expect the jet correction routine (see

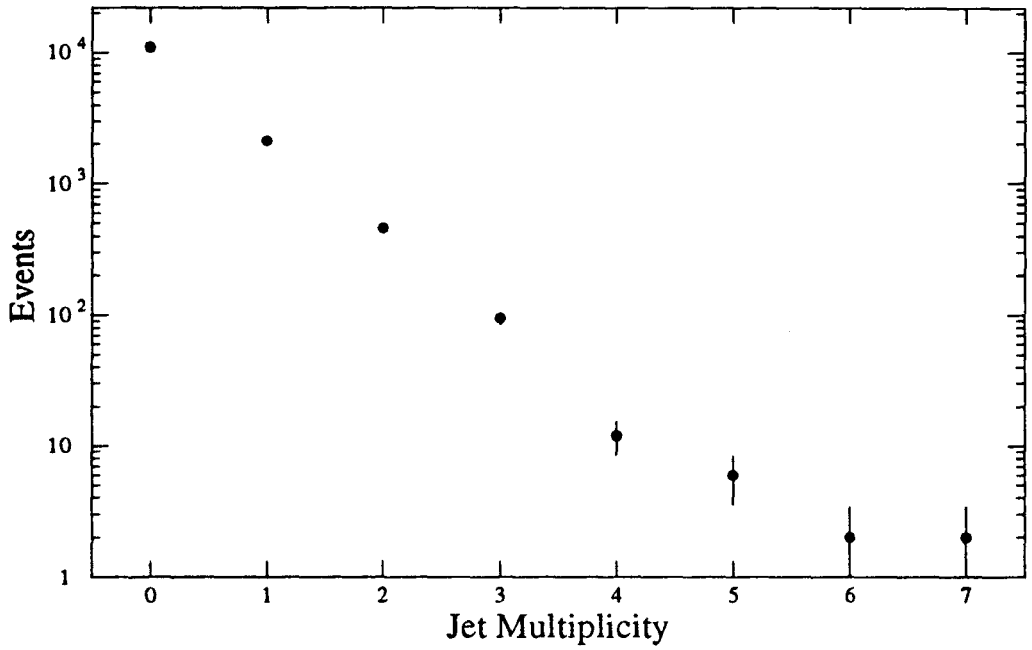

Figure 7.7: The exclusive jet multiplicity distribution for the $Z \rightarrow e^+e^-$ data sample.

Section 7.4.2) to correct for some of the calorimeter energy coming from extra interactions in the same crossing as the Z^0 event. However, at high instantaneous luminosities, a number of real jets will be formed from these additional interactions. These jets, which we dub X-jets, may combine with low-E_T jets produced with the Z^0 boson to bring them above the E_T cut threshold; a small number of X-jets can pass our jet selection cuts directly. We have investigated these effects using several different methods, one of which (the "minimum bias" method) we use to make a correction. The results are presented in Table 7.3. The details of the X-jet analysis are given below.

Table 7.3: Results of the "minimum bias method" for estimating the effect of X-jets on the Z^0 + jet data sample.

Event Sample	X-jet Correction in %
Z^0 + 0 jets	0.80 ± 0.72
Z^0 + 1 jet	-3.0 ± 3.0
Z^0 + 2 jets	-4.6 ± 3.3
Z^0 + 3 jets	-4.7 ± 3.4
$Z^0 + \geq 4$ jets	-5.2 ± 3.7

The most straightforward method we use to estimate the number of additional jets in our sample is to count jets in minimum bias events that pass our selection cuts[4]. We refer to this as the "minimum bias" method. We have produced a sample of minimum bias events with the same instantaneous luminosity distribution as that of our Z^0 dataset. These events are scanned for high-quality vertices, which we interpret as interaction vertices. Two methods are used to estimate the number of jets due to these vertices. In the first method, the 6030 minimum bias events in the sample with *exactly one* high-quality vertex each are examined. We find a total of 60 1-jet events and 9 2-jet events in this subsample. In the second method, we check the entire luminosity-weighted minimum bias sample containing a total of 13399 high-quality vertices. Using this method, we find 148 1-jet events, 15 2-jet events, and 1 3-jet event. In order to normalize to our Z^0 sample, we scale the average of these two results to the number of extra (*i.e.*, non-Z^0) high-quality vertices in our Z^0 dataset, which we measure to be 4564. We estimate that 48 events in our data sample have one additional jet, and 6 events have two additional jets.

[4]Minimum bias events are collected by requiring a beam-beam counter coincidence hit.

Applying this result to the number of Z^0 events in our data sample, we obtain the probability $P_1 = 0.0071$ that a single X-jet passing our selection cuts is produced in addition to the jets associated with the Z^0 boson, and $P_2 = 0.00089$ that two X-jets are produced in addition to the Z^0 jets. Because these probabilities are small, we can approximate the true jet multiplicity distribution (M) from the observed jet multiplicity distribution (N) with the following formulas:

$$M_0 \simeq N_0 + N_0P_1 + N_0P_2$$

$$M_1 \simeq N_1 + N_1P_1 + N_1P_2 - N_0P_1$$

$$M_2 \simeq N_2 + N_2P_1 + N_2P_2 - N_1P_1 - N_0P_2$$

and so forth. This correction leads to the percent changes in the $Z^0 + N$ jet samples given in Table 7.3.

In order to assign uncertainties to these numbers, we use several other methods to estimate the contamination of our jet sample due to extra interactions. In one method we select a subsample of 1-jet events and measure the angle between the direction of the Z^0 p_T and the p_T of the recoil jet. Whereas the signal peaks at 180°, we expect to obtain a flat distribution for events in which the Z^0 and jet are uncorrelated. We use fully simulated Monte Carlo events to subtract the "true" jet contribution from the flat X-jet background. This method gives an upper limit of 8% X-jets in our $Z^0 + 1$ jet sample.

In another method, we measure the increase in the number of jets from additional interactions by mixing clean Z^0 events with minimum bias events at the calorimeter tower level. We select clean Z^0 events from our final event sample by requiring absolutely no additional vertices in the event, thereby rejecting essentially all events containing additional interactions. The calorimeter banks

of these clean Z^0 events are mixed with the calorimeter banks in luminosity-weighted minimum bias events to produce a mixed data sample which models our actual Z^0 sample. By counting jets in the mixed sample we obtain estimates of how many events are promoted in jet multiplicity. We find that 4.8% to 8.1% of the Z^0 + 1 jet events are actually promoted 0-jet events, where the range in values reflects the uncertainty in counting the number of vertices for the underlying event correction.

A third estimate of the jet excess from additional interactions is obtained by studying the z vertex positions of jet tracks. Sixty percent of the 1663 jets in the Z^0 data sample contain at least one CTC[5] track, and we define the vertex of these jets to be the z vertex of the highest-p_T track in the jet. In the 1002 jets with CTC tracks, we observe that 3.7% of jet vertices lie more than 5 cm from the Z^0 boson vertex. If we assume that these jets originate from additional interactions, and the same percentage of jets without CTC tracks come from additional interactions, we estimate that roughly 3–4% of 1-jet Z^0 events are promoted 0-jet events.

Since the average number of interactions per beam crossing increases with instantaneous luminosity, we expect an excess of X-jets at high luminosity relative to a low-luminosity control sample. As a final check, we examine both the Z^0 and W datasets for excess jets in the high instantaneous luminosity events. We observe a deficit of Z^0 + 1 jet events at high luminosities (deficits in the Z^0 + 2 and Z^0 + 3 jet samples are not statistically significant). However, this method does not isolate the effect of X-jets from other effects which are luminosity-dependent. For example, the efficiency for finding Z^0 + jet events appears to drop with increasing luminosity, though the decrease is difficult

[5]Central Tracking Chamber

Table 7.4: $Z^0 + \geq N$ jet cross section errors due to jet counting uncertainties.

Jet Multiplicity	% error on B($Z \rightarrow e^+e^-$)σ
$\geq$0	0%
$\geq$1	$\pm$ 11%
$\geq$2	$\pm$ 17%
$\geq$3	$\pm$ 23%
$\geq$4	$\pm$ 23%

to quantify due to limited statistics. For comparison we use a high statistics W sample to look for excess jets at high luminosity. We suspect that the W jet multiplicity efficiency is less dependent on instantaneous luminosity, since this dependence for the Z^0's seems to come largely from the second electron selection efficiency. The results for the W show an excess of jets at high luminosity, as expected.

The above approaches give a range of estimates of the number of excess jets in our Z^0 + jet sample. We use the "minimum bias" method to make our jet multiplicity corrections. To be conservative, we include 100% uncertainties on our correction probabilities P_1 and P_2. The results are summarized in Table 7.3.

In Table 7.4 we summarize the combined systematic uncertainties in the $Z^0 + \geq N$ jet cross sections due to the jet counting errors enumerated above.

7.5 Tagging b Jets

The presence or absence in the jet sample of secondary decay vertices from b quark decay has no impact on the cross section calculation. We include a search for such vertices, also known as b tags, here, since some understanding

of jet identification methods is a prerequisite. The results of the b-tagging study are of peripheral importance to the overall purpose of this analysis, but may prove interesting in the search for non-Standard Model processes. Various studies[A+94b, A+94a] have shown that the CDF algorithm used to identify b secondary decay vertices is reliable. The Standard Model predicts that few such tags should be present in a Z^0 event sample. If the tagging algorithm finds an excess number of tags in our Z^0 dataset, this may indicate the presence of new physics.

The search for b tags in our Z^0 + jets sample proceeds in two parts. First, we establish a baseline value for the number of b tags we expect in the sample. To do this we run the tagging algorithm on a control sample consisting of inclusive jet events collected with the jet triggers. Not all the jets in these events are suitable for tagging. A "taggable" jet has the following characteristics:

- uncorrected $E_T > 15$ GeV
- $|\eta| < 2.0$
- at least two tracks with hits in the SVX[6].

The tagging procedure is run on the taggable subset of jets and yields the expected number of both positive (*i.e.*, physical) and negative (*i.e.*, unphysical) tags[7].

The same procedure is now repeated for the Z^0 sample. Of the total of 1663 jets, 442 are found to be taggable. Table 7.5 shows the number of positive and negative tags found in the Z^0 sample as a function of jet multiplicity, together

[6]Silicon VerteX detector

[7]An unphysical tag flags a jet in which a secondary vertex is reconstructed on the wrong side of the event vertex.

with the expected number of tags. We find no excess of b tags in our Z^0 event sample, in agreement with Standard Model predictions.

Table 7.5: Actual and expected b-tags in the Z^0 + jets sample.

Jets	Positive Tags	Pos. Tags Expected	Negative Tags	Neg. Tags Expected
= 1	2	3.32 ± 0.07	0	0.51 ± 0.03
= 2	3	1.85 ± 0.05	0	0.26 ± 0.02
≥3	1	1.17 ± 0.04	0	0.19 ± 0.02
all	6	6.34 ± 0.10	0	0.96 ± 0.04

7.6 The Z^0 + N Jets Data Sample

7.6.1 Acceptances

If this were a perfect world, we would be able to reconstruct every Z^0 produced in a $\overline{p}p$ interaction in our detector. In that case our acceptance, the ratio of detected Z^0s to produced Z^0s, would be 1. As it is, many factors conspire to complicate the detection of Z^0 bosons[8]. These factors can be geometric, pertaining to the probability that the Z^0 decay products will hit fiducial regions of the detector, and kinematic, pertaining to the probability that they will be produced with the requisite amount of momentum. There is another factor which affects this particular analysis especially, because it is related to the production of jets in the event. It has to do with the probability that one or both of the Z^0 decay products, though they may fall within the geometric and kinematic acceptances, will be obliterated or obscured by a nearby jet

[8]Note that we differentiate here between *detecting* the Z^0 and *selecting* the Z^0 . The first must occur for the second to be possible. The loss of Z^0 bosons due to the selection process is taken into account as an efficiency, which is described in Section 7.6.2.

and will not be reconstructed correctly. We refer to the efficiency due to this special case as the "lepton-jet overlap" acceptance. The overall acceptance A_Z is composed of the geometric, kinematic, and lepton-jet overlap acceptances.

Geometric and Kinematic Acceptances

In the determination of A_Z we use two programs which generate Z^0 bosons. The first of these is a Born-level Z^0 generator, which is used to measure the acceptance for Z^0 events with *no* jets. A Monte Carlo simulation is run on the generator output. The Monte Carlo smears the event vertex with a σ of 25.6 cm and an offset from $z = 0$ of -1.44 cm. This vertex distribution corresponds to that of the Run 1A data. The electron transverse momenta are smeared with a resolution of $0.002p_T$, and their energies are smeared with the resolution $(13.5\%\sqrt{E})^2 + (2\%E)^2$ for central electrons and $(28\%\sqrt{E})^2 + (2\%E)^2$ for plug and forward electrons. Since the Z^0 + 0 jet generator does not include a p_T boost, the Monte Carlo adds one. The p_T boost distribution used in the Monte Carlo is derived from the transverse momentum spectrum of W events from data[A+91c].

To determine the acceptances for events *with* jets, we use the leading-order matrix element calculation called VECBOS[BKTG91] to generate $Z^0 + N$ jet event samples, where $N = 1 - 3$. The events are unweighted, fragmented, and run through a full detector simulation, after which they are processed with the data analysis code (for the details of this procedure, see Chapter 8). Though we do not apply lepton or boson selection cuts to the generated events, we select jets using the criteria outlined in Section 7.4.3. We reject "feed-down" events, in which fewer jets are reconstructed than were generated.

The geometric and kinematic acceptance cuts are applied to the electrons in

the resulting 0-jet and N-jet samples. For the geometric acceptance we require that both electrons be in the fiducial volume of the detector and that at least one be in the central region. For the events passing the geometric acceptance requirements we check that the central electron has $E_T \geq 20$ GeV and $p_T \geq 13$ GeV, and that the second electron has $E_T \geq 20$ GeV if it is central, $E_T \geq 15$ GeV if it is in the plug region, and $E_T \geq 10$ GeV if it is forward.

Lepton-Jet Overlap Acceptance

Lastly, we turn to the determination of the lepton-jet overlap acceptance. Here, our approach changes somewhat—we use real data events as much as possible to preserve the true nature of the jet and underlying event structures which might interfere with the detection of the electron. Of course there is a rub: we cannot use the Z^0 events as they are, because the Z^0 bosons have already been identified. The method we employ to circumvent this problem is described here.

Using the Z^0 sample selected in Section 7.3, we record information on the Z^0 and on all jets and showers in the events in a data file. The quantities we record are: the momentum four-vector of the Z^0, the number of jets in the event (where no η or E_T cuts are imposed on the jets), the jet multiplicity as defined in Section 7.4.3, where only "good" jets are counted, the position of each jet in $\eta - \phi$ space, and its transverse energy. The final acceptance numbers are determined as a function of the "good" jet multiplicity, but the additional jets in the event are included in the study of overlap effects.

For each jet multiplicity, for both the inclusive ($Z+ \geq N$ jets) and exclusive ($Z + N$ jets) case, the Z^0 is boosted to its rest frame and decayed there into an electron-positron pair. Each Z^0 is decayed often enough for the resulting event

sample to contain about 50,000 events. The exact number of re-decays depends on the number of events in the input sets; for the high-statistics $Z+ \geq 0$ jets case, for example, each event is decayed approximately 10 times, whereas the low-statistics $Z+ \geq 4$ jets case requires each Z^0 to undergo about 5,000 decays. Unfortunately this means that for the higher jet multiplicities, there are fewer overall variations in the jet event geometries.

The decay products of the Z^0 are boosted back into the lab frame and are subjected to the geometric and kinematic acceptance cuts described above. This leaves approximately 25,000 events for the overlap study. The new electron and positron positions can now be compared to the positions of the jets and showers in the real event.

We divide the overlap study into two parts. In the first, we investigate the effects of requiring a minimum separation ΔR_{ej} between "good" jets and electrons. We demand that $\Delta R_{ej} > 1.3 \cdot R_{av}$, where $R_{av} = (R_e + R_j)/2$. For 0.4-clustered jets, $\Delta R_{ej} > 0.52$[9]. In the second part, we attempt to determine how often a nearby jet of *any* magnitude interferes with the detection of the electron. To do this, we look for a jet or shower within R_e of the electron position. If $E_{Tj} > 0.15 E_{Te}$ for such a jet, we consider the electron to have been "obliterated" by it, and the Z^0 to have been lost.

We obtain our baseline acceptance values for the lepton-jet overlap study by assuming that the Z^0 is polarized, and by applying the above cuts to the decay electrons. To determine the systematic uncertainties in this measurement we vary two parameters:

1. the polarization of the Z^0 (assume it is unpolarized);

[9]Because of the highly collimated nature of electron showers, we define $R_e = 0.4$.

2. the obliteration requirement: $E_{T_j} > (0.15 \pm 0.05)E_{T_e}$.

For each variation, half of the largest deviation from the baseline value is taken to be the error, and the two errors are added in quadrature to arrive at a systematic uncertainty.

Note that for any change in the baseline parameters the acceptances for all jet multiplicities will increase or decrease in a highly correlated manner. Therefore the systematic uncertainties for the *ratios* of acceptances (which is the way they enter into our cross section calculations) must be determined differently. Let A_N^{base} denote the baseline overlap acceptance for N jets, A_N^{unp} the acceptance for the case in which the Z^0 is unpolarized, A_N^{ob+} the acceptance for a tightening of the obliteration cut, and A_N^{ob-} the acceptance for a loosening of the obliteration cut. Then the positive systematic error σ^+ on the acceptance ratio for jet multiplicities K and N is given by

$$(\sigma^+)^2 = (\frac{A_K^{base}}{A_N^{base}} - \frac{A_K^{unp}}{A_N^{unp}})^2 + (\frac{A_K^{base}}{A_N^{base}} - \frac{A_K^{ob-}}{A_N^{ob-}})^2$$

Similarly,

$$(\sigma^-)^2 = (\frac{A_K^{base}}{A_N^{base}} - \frac{A_K^{unp}}{A_N^{unp}})^2 + (\frac{A_K^{base}}{A_N^{base}} - \frac{A_K^{ob+}}{A_N^{ob+}})^2$$

Of these errors, we choose the larger and assign a symmetric error of that magnitude to the obliteration acceptance ratios. These are the systematic uncertainties which enter into the cross section calculation. See Table 7.6 for a summary of the ratios and associated systematic errors.

Z^0 + Jet Acceptance Summary

The total acceptance A_Z for our Z^0 events is the product $A_{geom}A_{kin}A_{overlap}$ of the geometric, kinematic, and overlap acceptances. Table 7.7 shows these

Table 7.6: Electron-Jet Overlap Efficiency Ratios and Associated Systematic Errors.

Jet Mult. Ratio	Efficiency Ratio	Systematic Uncertainty
$\geq 0/\geq 1$	1.0589	0.0058
$\geq 0/\geq 2$	1.119	0.012
$\geq 0/\geq 3$	1.160	0.028
$\geq 0/\geq 4$	1.252	0.070

acceptances for Z^0 events as a function of associated jet multiplicity.

Table 7.7: Acceptances in $Z^0 + \geq N$ Jet Events (statistical errors only). A_{geom} and A_{kin} were not computed directly for the ≥ 4 jets case; the ≥ 3 values were used.

N	A_{geom}	A_{kin}	$A_{overlap}$	Combined A_Z
0	0.4446 ± 0.0016	0.9037 ± 0.0015	0.9135 ± 0.0018	0.3670 ± 0.0016
1	0.4488 ± 0.0029	0.9006 ± 0.0026	0.8627 ± 0.0022	0.3487 ± 0.0026
2	0.472 ± 0.010	0.8801 ± 0.0095	0.8164 ± 0.0025	0.3391 ± 0.0081
3	0.503 ± 0.018	0.882 ± 0.017	0.7872 ± 0.0027	0.349 ± 0.014
4	0.503 ± 0.018	0.882 ± 0.017	0.7298 ± 0.0029	0.324 ± 0.013

7.6.2 Efficiencies

Once a Z^0 event can be seen, at least in principle, in the detector, any subsequent loss of events is due to the quality cuts imposed on the decay products of the Z^0 and falls under the heading of an efficiency. The reasons for making stringent requirements are to minimize backgrounds; it is imperative, however, that the cuts remove as few real signal events as possible in the process.

Two types of efficiencies are determined in our analysis: the efficiency of our electron selection, or identification, cuts, and the central electron trig-

ger efficiency. For both of these we use events containing high-p_T electrons which are unbiased by the ID or trigger cuts whose efficiencies we want to measure[A+94c]. We use electrons stemming from W or Z^0 decay, but the selection of these events is different from that described in Section 7.3.

Electron Identification Efficiencies

The electron ID efficiency samples are taken from Z^0 events in which no electron selection (ID) cuts have been applied to the second leg of the Z^0. The events are chosen by requiring tight cuts on the primary central electron, and the presence of a second fiducial EM cluster with a minimum amount of energy in accordance with the kinematic acceptance requirements. The second electron candidate must form an invariant mass with the primary electron which falls within a tight window about the nominal Z^0 mass: $81 < M_{ee} < 101$ GeV/c^2. Four different efficiencies are measured: the efficiency for

1. a central electron to pass the tight central cuts (ϵ_{ct});
2. a central electron to pass the loose central cuts (ϵ_{cl});
3. a plug electron to pass the loose plug cuts (ϵ_p); and
4. a forward electron to pass the loose forward cuts (ϵ_f).

In each of these cases we apply the appropriate ID cuts to the unbiased second leg of the Z^0 , and obtain the fraction of events which pass the requirements.

In using this method we make the implicit assumption that the Z^0 s in the efficiency sample are 100% pure. This is not actually the case, as there is a small QCD background under the Z^0 peak even for the tight invariant mass requirement that we impose (for details on Z^0 backgrounds, see Section 7.6.3).

If we assume that the electron ID cuts are as efficient for jets as for electrons, then our ID efficiency results are correct. However, since by design the cuts are less efficient for jets, our results tend to underestimate the true electron ID efficiency ϵ_e, where

$$\epsilon_e = \frac{\epsilon_{calc} - F_{jet}\epsilon_{jet}}{F_e}.$$

F_e and F_{jet} denote the electron and jet fractions, respectively. Assuming the 1σ upper limit QCD background in the $Z^0 + \geq 0$ jet sample, and $\epsilon_{jet} = 0$ (a worst-case scenario), the underestimate of the true electron ID efficiency amounts to a 1% effect for the tight central electron cuts.

For the four efficiency samples the cuts on the primary electron are the same. We apply all the tight electron cuts listed in Section 7.3, and add the requirements $I(0.4) < 0.05$ and $HAD/EM < 0.05$ to enhance event purity. The second EM cluster must fall within the geometric and kinematic acceptances and be separated from any high-E_T jets in the event by $\Delta R_{ej} > 0.52$ (see Section 7.6.1). For each efficiency sample some additional requirements may be made on the second EM cluster; these are given below. The samples are grouped by exclusive jet multiplicity. As the jet multiplicity rises, the corresponding efficiency sample size necessarily diminishes. Table 7.8 shows the number of events N in the central, plug, and forward efficiency samples for each jet multiplicity.

Tight Central ID Efficiency The central efficiency sample N_C has two additional requirements on the second central EM cluster: an associated track with $p_T > 5$ GeV/c and a charge opposite to that of the primary electron. There are a total of 2237 events which satisfy these requirements.

Table 7.8: Number of Events N in the Central, Plug, and Forward Efficiency Samples.

Event Sample	Central N_C	Plug N_P	Forward N_F
$Z + 0$ jets	1920	2247	521
$Z + 1$ jet	266	342	67
$Z + 2$ jets	46	48	8
$Z + \geq 3$ jets	5	9	5
Total	2237	2646	601

We apply the tight central electron cuts to the second electron cluster in each event, and record how many events pass each cut. The efficiency ϵ_{ct} is calculated taking into account the fact that a CC Z^0 has two chances of making it into the sample; therefore the proper efficiency is given by

$$\epsilon_{ct} = \frac{2N_t}{N_t + N_C},$$

where N_t is the number of electrons which pass the tight cuts. The derivation of this equation is given in Appendix A.

Since a track is required for the tight central electron, we also determine the track reconstruction efficiency. To do this we choose events in which the second EM cluster must pass all the central efficiency sample cuts above except for the track-related cuts, *i.e.*, the p_T and opposite-charge cuts. If an event in this tracking efficiency sample does not have a 3-D track pointing to the second central cluster, it is considered a tracking failure. The resultant tracking efficiency is factored into the overall ϵ_{ct} efficiency.

The individual efficiencies for each of the tight central cuts in a sample with $N = 0$ jets are shown in Table 7.9. The overall efficiencies ϵ_{ct} as a function of

jet multiplicity are given in Table 7.13, along with the efficiencies ϵ_{cl}, ϵ_p, and ϵ_f.

Table 7.9: ID efficiencies for tight central electron cuts.

Z^0 + 0 jets, 1920 Events in Sample		
Cut	Events Passing	Efficiency
Conversion	1887	0.9913 ± 0.0015
HAD/EM	1886	0.9911 ± 0.0015
E/P	1763	0.9574 ± 0.0034
L_{shr}	1894	0.9932 ± 0.0013
χ^2_{str}	1793	0.9658 ± 0.0030
$\|\Delta x\|$	1764	0.9577 ± 0.0034
$\|\Delta z\|$	1894	0.9932 ± 0.0013
Isolation	1878	0.9889 ± 0.0017
all ID cuts	1495	0.8755 ± 0.0060
Tracking		1.0
ϵ_{ct}	1495	0.8755 ± 0.0060

Loose Central ID Efficiency Using the identical central efficiency sample as for the tight central ID efficiency (N_C = 2237 events), we apply loose central cuts to the second cluster. No tracking efficiencies are factored in. The efficiency for a central electron to pass the loose cuts is given by

$$\epsilon_{cl} = \frac{N_t + N_l}{N_t + N_C},$$

where N_l is the number of electrons passing the loose cuts. This equation is derived in Appendix A. The resulting ϵ_{cl} efficiencies are tabulated in Table 7.10.

Plug Electron ID Efficiency For the plug efficiency sample, we require that the second EM cluster be in the fiducial plug region, with $E_T > 15$ GeV and $HAD/EM < 0.05$. There are a total of N_P = 2646 events in the plug

Table 7.10: ID efficiencies for loose central electron cuts.

Z^0 + 0 jets, 1920 Events in Sample		
Cut	Events Passing	Efficiency
Conversion	1887	0.9913 ± 0.0015
HAD/EM	1920	1.0
Isolation	1878	0.9889 ± 0.0017
ϵ_{cl}	1845	0.9780 ± 0.0025

efficiency sample; see Table 7.8 for a breakdown by jet multiplicity. We apply the loose plug electron ID cuts to the sample to obtain ϵ_p, where

$$\epsilon_p = \frac{N_{pass}}{N_P}.$$

The efficiencies for each cut are shown in Table 7.11.

Table 7.11: ID efficiencies for loose plug electron cuts.

Z^0 + 0 jets, 2247 Events in Sample		
Cut	Events Passing	Efficiency
Conversion	2005	0.8923 ± 0.0065
$\chi^2_{3\times3}$	2247	1.0
Isolation	2164	0.9631 ± 0.0040
ϵ_p	1930	0.8589 ± 0.0073

Forward Electron ID Efficiency The forward efficiency sample is the same as the plug sample except that we require a forward EM cluster with $E_T > 10$ GeV and with an associated VTX occupancy of more than 0.25. There are a total of $N_F = 601$ events in the sample. We apply the forward ID cuts to the

second EM cluster to determine ϵ_f, given by

$$\epsilon_f = \frac{N_{pass}}{N_F}.$$

The efficiencies for each cut are shown in Table 7.12. In this sample, unlike the other three, there is no electron-jet separation requirement because jets beyond the plug are not considered. Therefore, the forward ID cuts show a marked dependence on the presence of jets.

Table 7.12: ID efficiencies for loose forward electron cuts.

Z^0 + 0 jets, 521 Events in Sample		
Cut	Events Passing	Efficiency
Isolation	447	0.858 ± 0.015
ϵ_f	447	0.858 ± 0.015

Electron ID Efficiencies — Summary It is apparent that in all cases except the forward, the ID cut efficiencies are independent of jet multiplicity. We expect this to be the case because we have taken into account any explicit jet-related dependences in the lepton-jet overlap study (Section 7.6.1). Because of the large errors resulting from the limited statistics at high jet multiplicities, we calculate the efficiencies for the inclusive ($\geq$ 0 jet) samples; these numbers are used for all jet multiplicities for the central and plug cases. For the forward, we calculate efficiencies for events with no jets and events with one or more jets, and we use the $\geq$ 1 efficiency for all events containing jets. We artificially inflate the true statistical errors for these "averaged" cases by doubling them, to account for any jet multiplicity dependence unobserved due to the limited

statistics. The contribution of the errors to the cross section is negligible in either case. The efficiency results are shown in Table 7.13.

Table 7.13: Overall ID efficiencies as a function of jet multiplicity N. The efficiencies used in the cross section calculation are indicated in bold face.

N	ϵ_{ct}	ϵ_{cl}	ϵ_p	ϵ_f
=0	0.876 ± 0.006	0.978 ± 0.003	0.859 ± 0.007	**0.858 ± 0.015**
=1	0.873 ± 0.016	0.973 ± 0.008	0.848 ± 0.019	0.582 ± 0.060
=2	0.905 ± 0.034	0.976 ± 0.017	0.854 ± 0.051	0.63 ± 0.17
≥3	0.75 ± 0.17	1.0 ± 0.0	0.89 ± 0.10	0.40 ± 0.22
≥0	**0.876 ± 0.011**	**0.977 ± 0.004**	**0.858 ± 0.014**	
≥1				**0.58 ± 0.11**

Central Electron Trigger Efficiencies

Since the Z^0 sample is extracted from an inclusive electron dataset which, by definition, has passed the Level 3 central electron trigger requirements, we cannot use it to determine the trigger efficiency for central electrons. We instead take W events which have come in on a different trigger, the missing E_T trigger[10]. We demand that the electron in the event pass our tight central electron cuts and that the missing E_T be greater than 25 GeV. In the resulting efficiency sample we determine how many events pass the Level 2 and Level 3 trigger requirements on the electron. This gives us the trigger efficiency ϵ_T for our central electron sample, shown broken down by jet multiplicity in Table 7.14. For the sake of consistency, and because there appears to be no dependence on jet multiplicity, we use the inclusive (≥ 0 jet) efficiency in our cross section measurement.

[10]Missing E_T refers to a transverse energy imbalance in the detector from which the presence of a neutrino is inferred.

Table 7.14: Central Electron Trigger Efficiencies.

Jet Mult.	Events in Sample	Efficiency	
		Level 2	Level 3
= 0	30068	0.9936 ± 0.0005	1.0000
= 1	5497	0.9969 ± 0.0007	1.0000
= 2	1132	0.9947 ± 0.0022	1.0000
= 3	242	0.9959 ± 0.0041	1.0000
≥ 4	60	0.9667 ± 0.0232	1.0000
≥ 0	36999	**0.9941 ± 0.0004**	**1.0000**

7.6.3 Backgrounds

Although we have ensured that the events we select are very clean by imposing quality cuts on the Z^0 decay products, some backgrounds remain which must be taken into account.

By far the largest background stems from QCD jet events in which the jets mimic electrons in the calorimeters. The misidentified jets must have an invariant mass which lies within the Z^0 mass window. This conjunction of coincidences, though relatively rare, is not negligible, because of the huge number of dijet events that are normally produced in $\bar{p}p$ interactions. Other, smaller backgrounds to our sample come from $W \rightarrow e\nu$ + jet events[11] in which one of the jets mimics an electron, or from $Z^0 \rightarrow \tau^+\tau^-$ decays. If a τ decays leptonically into an electron or muon and two neutrinos, the charged lepton will likely fail the minimum E_T cut of 20 GeV and thus be excluded from our sample. If it decays hadronically, however (*e.g.*, $\tau^- \rightarrow \pi^-\nu_\tau$, $\tau^- \rightarrow \pi^0\pi^-\nu_\tau$), it can deposit well-collimated energy in the calorimeters, and hence be misidentified as an electron.

[11]The W event sample is approximately ten times as large as the equivalent Z^0 sample.

In all the above background processes, one or both of the decay products of the fake Z^0 are actually jets misidentified as electrons. Thus the method we outline in this section for estimating the hadronic backgrounds to Z^0 production includes not only pure QCD backgrounds, but also hadronic decay processes in in which an electron is mimicked in some way. The backgrounds we quote can be taken to be overall backgrounds to our Z^0 event sample.

We begin by obtaining an event sample in which all the Z^0 selection cuts described in Section 7.3 are applied except for the electron isolation cuts and the Z^0 mass window cut. From this sample we select two subsets: the *isolated* set, where both electrons are well isolated ($I(0.4) < 0.1$), and the *anti-isolated* set, in which neither electron is isolated ($I(0.4) > 0.1$). In the following paragraphs, the isolated set will be denoted by a superscripted I, and the anti-isolated set by a superscripted A. Our final Z^0 sample is fully contained in the isolated set, whereas there should be essentially no contribution from Z^0 decays in the anti-isolated set. This assumption is borne out by the absence of a Z^0 signal peak in the anti-isolated M_{ee} spectrum, as can be seen in Figure 7.8.

In the M_{ee} spectra of the isolated and anti-isolated sets, we define two regions: the *Z-peak* region, where $76 < M_{e^+e^-} < 106$ GeV/c^2, and the *sidebands*, where $50 < M_{e^+e^-} < 70$ GeV/c^2 or $110 < M_{e^+e^-} < 150$ GeV/c^2. These regions henceforth will be indicated by subscripted Z and S, respectively. In our event sample, we find the number of events N in each category: $N_Z^I = 6708$, $N_Z^A = 207$, $N_S^I = 409$, and $N_S^A = 330$.

We assume that the shape of the M_{ee} distribution for QCD background events (*i.e.*, events in which jets mimic electrons), is independent of the "elec-

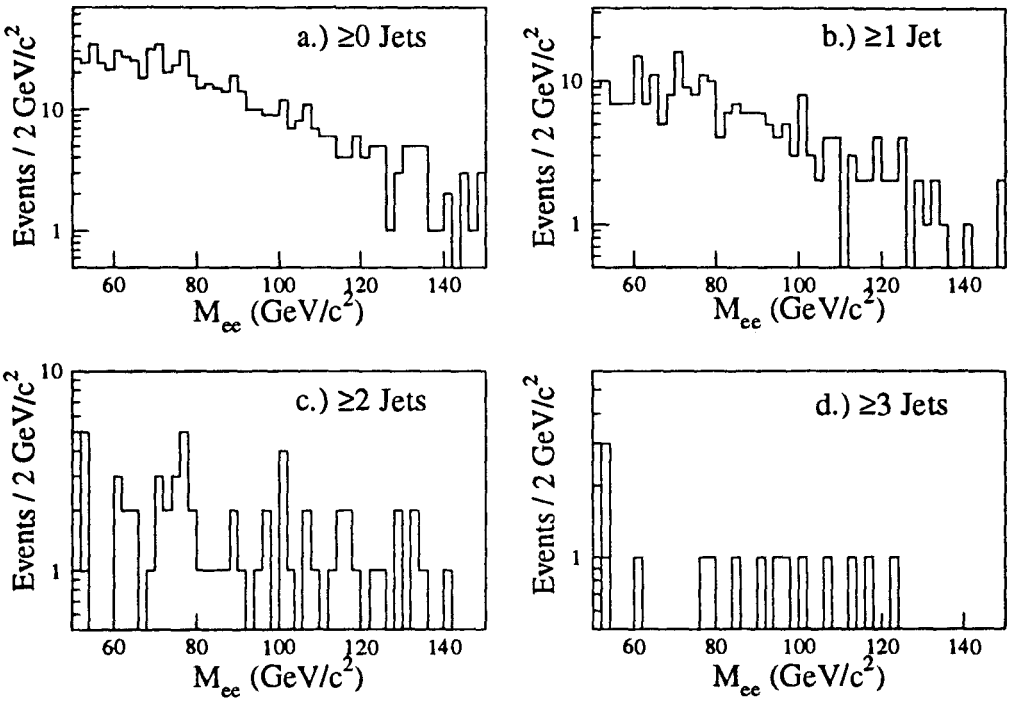

Figure 7.8: Invariant mass distributions of anti-isolated electron pairs in a.) ≥ 0, b.) ≥ 1, c.) ≥ 2, and d.) ≥ 3 jet events.

tron" isolation. Given this assumption, we estimate the QCD background B_Z in the isolated *Z-peak* region N_Z^I by scaling the number of events in the anti-isolated *Z-peak* region as follows.

Using a Z^0 + Drell-Yan Monte Carlo algorithm, we obtain the ratio f of $Z + DY$ events in the sidebands to $Z + DY$ events in the *Z-peak*. The expected number of $Z + DY$ events in the isolated *sidebands* is given by

$$S = f \times (N_Z^I - B_Z). \tag{7.4}$$

This number agrees with what is observed in the data, allowing for a small

excess in the data due to the QCD background, B_S, which is given by

$$B_S = N_S^I - S. \tag{7.5}$$

To get B_Z, we use the fact that the background fraction in the anti-isolated *sidebands* is the same as in the anti-isolated *Z-peak*:

$$B_Z = \frac{N_Z^A}{N_S^A} \times B_S. \tag{7.6}$$

Combining Equations 7.4, 7.5 and 7.6 and solving for B_Z, we obtain

$$B_Z = \frac{N_S^I - f N_Z^I}{\frac{N_S^A}{N_Z^A} - f}. \tag{7.7}$$

Equation 7.7 yields the expected number of QCD background events in the Z^0 signal sample selected in Section 7.3. Since we are interested in the backgrounds as a function of the inclusive jet multiplicity associated with the production of the Z^0, we use the same method for Z^0 samples with $\geq N$ jets, for N = 0–3. To calculate the uncertainty on the resulting background numbers, 200,000 Monte Carlo events are generated in which the values for N_Z^I, N_Z^A, N_S^I, and N_S^A are randomly selected from Poisson distributions centered on the appropriate data values. The results are given in Table 7.15.

The background determination above is concerned with the purity of the Z^0 bosons in our event sample. We must consider the fact that there are a few processes which will contribute fake *jets* to our Z^0 + jets dataset. These processes are $\overline{p}p \rightarrow Z^0 + \gamma$, where the γ is identified and corrected as a jet, and $\overline{p}p \rightarrow Z^0 + W$ or $Z^0 + Z^0$, where the second boson decays hadronically. The backgrounds from diboson sources are small compared to the jet-counting systematics. We estimate a total background of about 35 $\geq$ 1 jet events from

Table 7.15: Results of QCD Background Studies in the Z^0 + Jets Sample

Jet Mult.	Background Events	Background (%)	1-σ Upper Limit (%)
≥ 0	$55.4^{+15.4}_{-14.9}$	0.8	1.1
≥ 1	$22.0^{+8.5}_{-8.1}$	1.7	2.3
≥ 2	$4.5^{+4.0}_{-3.7}$	1.6	3.0
≥ 3	$0.3^{+2.0}_{-0.3}$	0.5	4.0

$Z^0 + \gamma$, $0.7 \geq 2$ jet events from $Z^0 + Z^0$, and $1.6 \geq 2$ jet events from $Z^0 + W$ production.

Chapter 8

The QCD Predictions

8.1 Overview

To test our ability to model the production of Z^0 + jets correctly, we compare the results we obtain from the data to results obtained from a QCD Monte Carlo algorithm. The program we use for this purpose is a leading-order tree-level matrix element calculation called VECBOS[BKTG91]. There are two types of comparisons we can make between the data and the QCD predictions obtained through VECBOS. The first is a comparison of the cross sections we calculate for $Z^0 + N$ jet production. The second is a test of how well VECBOS models the kinematic properties of $Z^0 + N$ jet events, such as the E_T spectra of the jets, the p_T of the Z^0, and correlated jet quantities such as the dijet mass spectrum. The two types of comparisons require slightly different approaches in the way the VECBOS output is handled. The results of our study give us a very good picture of where the strengths and weaknesses of the theory underlying the QCD predictions lie.

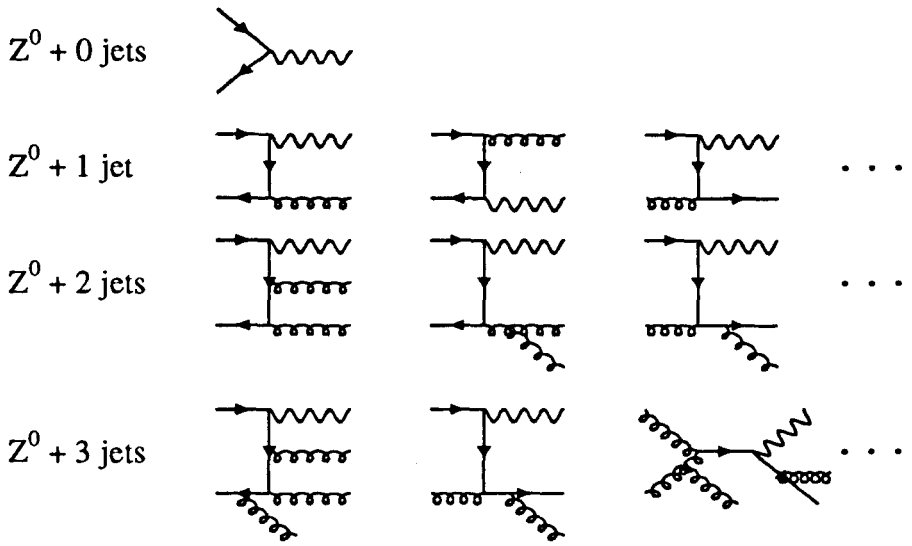

Figure 8.1: Some of the tree-level diagrams which contribute to the LO QCD calculations. The arrows represent quarks, the wavy lines are Z^0 bosons, and the curly lines are gluons.

8.2 The Leading-Order QCD Diagrams

In the leading-order QCD calculation which we employ, the contributing diagrams are tree-level diagrams, a selection of which is shown in Figure 8.1. There are additional diagrams which correspond to "double-parton" interactions. These are not explicitly included in our QCD predictions.

8.3 The Matrix Element Calculations

The effective QCD coupling α_s decreases as the momentum transfer of an interaction increases. At large Q^2, in our case on the order of M_Z^2, α_s is small enough to allow precision tests of QCD to be performed using perturbation theory. A perturbative expansion of a QCD cross section is given by the equation[Par94]

$$\sigma = A_1\alpha_s + A_2{\alpha_s}^2 + A_3{\alpha_s}^3 + ..., \tag{8.1}$$

where the coefficients A_1, A_2, etc., include the effects of the parton distribution functions (PDFs) and the matrix elements calculated using the Feynman diagrams appropriate for the given order of α_s. Of course, in the case of heavy boson production, the cross section expansion contains a zeroth-order QCD term A_0 corresponding to the Born-level process.

The divergences which arise in calculations of QCD cross sections are regulated by renormalizing. The most commonly used renormalization scheme (RS) is the modified minimal subtraction scheme, denoted by $\overline{\text{MS}}$. Although the full expansion of σ to all orders of magnitude, corresponding to the physical observable, is independent of the RS, for truncated expansions the coefficients A_n are implicitly dependent on the renormalization scheme used. They also rely explicitly on a mass scale, Q_r, which is introduced during renormalization to preserve the dimensionless nature of the coupling. The mass scale determines the dependence of a calculation on the RS used, but there is no way to be certain which Q_r is the correct choice. Higher-order corrections serve to make predictions less sensitive to the choice of Q_r, but do nothing to fix its value[Par94]. However, at leading order, which corresponds to the term $A_1\alpha_s$ of the cross section expansion, the dependence on Q_r resides *entirely* in α_s; that

is, A_1 is independent of Q_r and depends only on the PDF and the factorization scale used.

The dependence of the n-loop QCD coupling α_s on the renormalization scale is given by[GGY95]

$$\alpha_s(Q_r) = \frac{\alpha_s(Q_0)}{1 + \alpha_s(Q_0)L^{(n)}(\frac{Q_r}{Q_0})}, \tag{8.2}$$

where

$$L^{(1)} = b_0 \ln(\frac{Q_r}{Q_0}), \tag{8.3}$$

$$L^{(2)} = (b_0 + b_1\alpha_s(Q_0)) \ln(\frac{Q_r}{Q_0}), \tag{8.4}$$

$$L^{(3)} = (b_0 + b_1\alpha_s(Q_0) + b_2^{\overline{MS}}{\alpha_s}^2(Q_0)) \ln(\frac{Q_r}{Q_0}) - \frac{b_0 b_1}{2}{\alpha_s}^2(Q_0) \ln^2(\frac{Q_r}{Q_0}). \tag{8.5}$$

The coefficients b_n are derived from the Callan-Symanzik β-function. They depend explicitly on the number of flavors N_f present in the calculation. Quarks with masses $M_q > Q_r$ are not included in the determination of b_n. At flavor boundaries (*e.g.*, near the b-quark mass), there is a discontinuous change in the b_n values. This circumstance necessitates a complementary adjustment in the value used for Q_0, in order to force $\alpha_s(Q_r)$ to be continuous across flavor thresholds. If $Q_r = M_Z$, for example, $N_f = 5$. While the constants b_0 and b_1 are independent of the RS used, higher-order terms are not, and are generally given in the $\overline{\text{MS}}$ scheme.

We obtain our matrix element calculations for $Z^0 + N$ Jet production (where N ranges from 1 to 3) using the leading-order (LO) generator VECBOS. As mentioned above, the dependence on Q_r at leading order resides in α_s. In generating our events we assume a 2-loop α_s evolution, which means that we

substitute the term for $L^{(2)}$ (Equation 8.4) into Equation 8.2. Figure 8.2 shows the behavior of α_s as a function of Q_r.

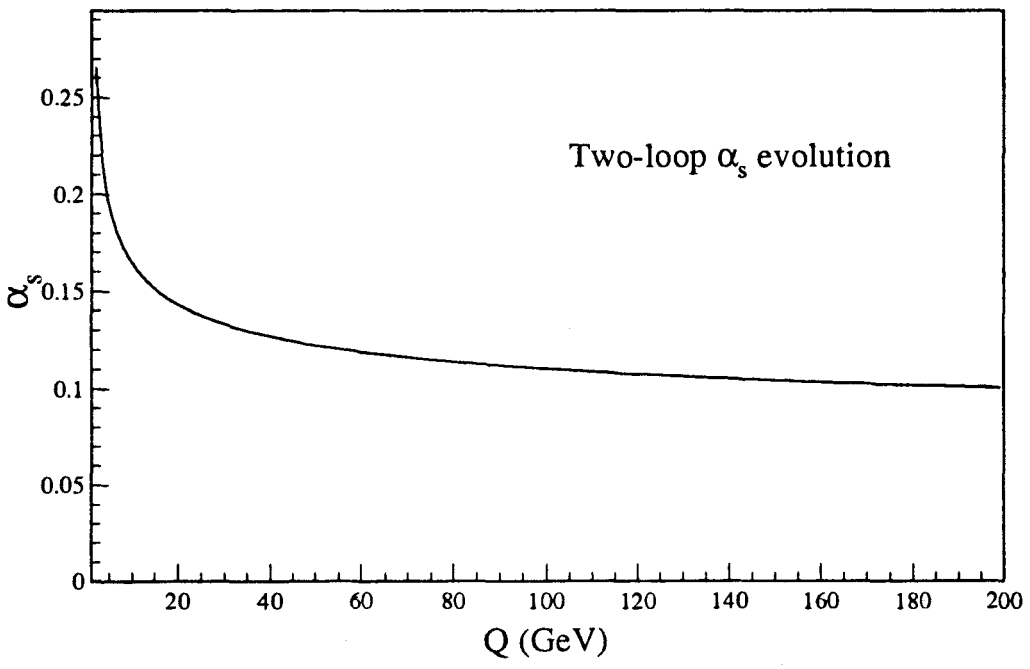

Figure 8.2: A plot of α_s shown as a function of Q_r.

VECBOS allows the user to fix Q_r at some desired quantity. The two mass scales we investigate in our analysis are given by the expressions

$$Q^2 = \langle p_T \rangle^2,$$

where p_T refers to the transverse momentum of the partons produced along with the Z^0, and

$$Q^2 = M_Z^2 + p_{TZ}^2.$$

The factorization mass scale is set to the same value as Q_r in each case. For our final QCD event samples we use the CTEQ 3M parton distribution functions. Comparison with samples generated using MRSD0′ indicate that the systematic uncertainty due to different PDFs is $< 5\%$.

The most natural mass scale to use for processes involving intermediate vector boson production would seem to be something approximating the mass of the boson. To test this assumption, we employ the $Z^0 + 1$ jet event generator DYRAD[GGK93]. DYRAD is a next-to-leading order matrix element calculation, but it can be used at leading-order, also. Using a Q^2 scale of $\langle p_T \rangle^2$, we find that both VECBOS and the DYRAD LO calculation give the same results within statistical errors, as expected: $\mathrm{B}(Z \to e^+e^-)\sigma_{VEC,LO} = 35.8 \pm 0.51$ and $\mathrm{B}(Z \to e^+e^-)\sigma_{DYR,LO} = 36.7 \pm 0.51$. However, when the DYRAD cross section is calculated to NLO, we find that the agreement between DYRAD and VECBOS is poor unless the Q^2 scale is raised. At $Q^2 = M_Z^2 + {p_T}_Z^2$, we obtain $\mathrm{B}(Z \to e^+e^-)\sigma_{DYR,NLO} = 35.6 \pm 0.9$, once again in excellent agreement with the LO value (recall that for all these calculations we use the 2-loop α_s evolution). In short, we find

$$ {\alpha_s}^{2\text{-loop}}(Q = \langle p_T \rangle)\, |\mathcal{M}|^2_{LO} \simeq {\alpha_s}^{2\text{-loop}}(Q = \sqrt{M_Z^2 + {p_T}_Z^2})\, |\mathcal{M}|^2_{NLO}. $$

We have no NLO calculation for the 2 and 3 jet cases, so we cannot determine whether this holds in those cases, also. We make the assumption that it does. Thus, it appears as though the results of a NLO calculation at high Q^2 can be approximated at LO by lowering the Q^2 value used at the generator level.

In the generation of the Z^0 boson no restrictions are placed on the p_T or pseudorapidity η of the leptons into which the Z^0 decays. However, to avoid the infrared divergences which occur when generating low-p_T partons, and

the collinear divergences which arise from cases in which two partons lie close together, we impose several kinematic cuts on the partons produced along with the Z^0. We demand that partons be generated with

- $p_T > 8$ GeV/c
- $|\eta| < 3.5$
- $\Delta R_{pp} > 0.4$, where $\Delta R = \sqrt{\Delta\eta^2 + \Delta\phi^2}$.

The p_T cut is well away from the low-p_T region where divergences become troublesome. It is low enough, however, for the turn-on effects to be negligible once the final analysis cut of $E_T > 15$ GeV is applied to the VECBOS-generated jets[1].

Because of the steeply falling E_T spectrum of the generated partons, a large fraction of them fail to pass the final jet cuts. This means that for events in which two partons are generated, often fewer than two will pass the jet E_T requirements. This phenomenon is termed "feed-down," because high-multiplicity generated events potentially contribute entries to lower-multiplicity event samples. We prevent this occurrence in our QCD event samples by accepting only events in which as many partons pass the jet cuts as are initially generated. A related phenomenon, in which more jets are reconstructed than are generated, is called "feed-up"; this will be discussed in Section 8.5.

The output created by VECBOS is an event list containing the weight of the event and the momentum 4-vectors of the Z^0 decay products and the associated partons. This information can be used to determine parton-level cross sections,

[1]If the parton p_T cut is lowered, we do see some additional contributions due to unlimited *gluon radiation* introduced during fragmentation. See Section 8.4 for a description of the fragmentation process.

Table 8.1: Parton-Level Cross Sections B($Z \rightarrow e^+e^-$)$\sigma(\bar{p}p \rightarrow Z^0 + N$ partons), in pb.

Jet Mult.	$Q^2 = \langle p_T \rangle^2$	$Q^2 = M_Z^2 + {p_T}_Z^2$
≥ 1	35.8 ± 0.51	28.2 ± 0.40
≥ 2	8.31 ± 0.29	4.76 ± 0.13
≥ 3	1.75 ± 0.15	0.777 ± 0.058

for which the jet selection cuts described in Section 7.4 are applied directly to the partons. The weights of the events passing the jet criteria are added; their sum represents the cross section of the process for the given jet multiplicity. Table 8.1 shows the parton-level cross sections for the various jet multiplicities.

There has been much discussion[Bar, Gie] concerning the issue of whether the output of the N-parton generator VECBOS should be regarded as inclusive over higher multiplicities, or exclusive. The LO matrix element calculation uses diagrams where the primary production is of order ${\alpha_s}^N$ (where N denotes the number of partons produced), and ignores diagrams corresponding to higher orders of α_s. The calculation *does* include diagrams in which a gluon emitted from an initial or final state parton is counted as one of the N generated partons. This introduces some dependence on higher-order diagrams. Within the limitations imposed by a leading-order calculation, VECBOS $Z^0 + N$ parton production is *inclusive* over higher jet multiplicities, *i.e.*, using N-parton VECBOS output yields ($\geq N$) results at reconstructed jet level.

Parton-level cross sections, though useful for comparisons to fully reconstructed jet-level QCD cross sections, cannot be compared to cross sections derived from the data analysis. Real events have clearly undergone fragmentation and have been subjected to underlying event and detector-related effects.

For jet-level cross section numbers and for differential distribution plots which we can compare directly to our data, several additional steps are necessary in the development of a QCD event sample.

8.4 Fragmentation

Events emerging from VECBOS are passed into a fragmentation algorithm derived from HERWIG[MW88, M+92]. Depending on the purpose of the sample in question, before being run through the HERWIG routine it may first be unweighted, yielding a set of events with integer weights. The unit-weight events are used to examine the differential distributions of the Z^0 and jets in generated events. The much smaller size of the unweighted sample greatly reduces processing time but can introduce statistical fluctuations. Unweighting is *not* necessary for samples used in cross section calculations, where event weights and large sample sizes are desired.

HERWIG continues the evolution of events in the sample by adding initial and final state gluon radiation, fragmenting the quarks and gluons into jets of hadronic particles, and providing an underlying event. All of these facets impact the eventual determination of jet energies and multiplicities in ways not apparent at parton level. By default HERWIG uses the mass scale Q_r passed to it by VECBOS (though it is possible to change the Q_r value manually) to place an upper limit on the magnitude of the allowed gluon radiation. Especially at higher jet multiplicities, changing the magnitude of the allowed gluon radiation has a large effect on the jet-level cross section determinations when jet selection cuts are applied.

There is no definitive indication that one Q_r is to be preferred over an-

other in HERWIG[Man, Gos]. Though there is no *a priori* reason to place an arbitrary limit on initial or final state gluon radiation, there is some concern that the absence of such a limit, in particular at high multiplicities, would lead to the double-counting of effects which have supposedly already been summed over at the VECBOS level (see Section 8.3). This conundrum has led to an exhaustive survey of different combinations of generator- and HERWIG-level Q_r values[GHRZ95]. The use of another fragmentation algorithm called SETPRT, which is derived from ISAJET[PP93], is also of value. SETPRT uses the jet fragmentation parametrization of Field and Feynman[FF78], which has been tuned to inclusive jet data. It does not include initial state gluon radiation and consequently does not depend on Q_r, so it provides a natural baseline to which the effects of changes in Q_r in HERWIG can be compared.

The output of HERWIG is in the form of the momentum four-vectors of the hadronized particles as well as the additional particles from the initial and final state radiation and the underlying event. Also included are the properties of the particles (such as lifetime, decay modes, etc.) and the particle history (*e.g.*, the parent particles). These banks are passed along to the next stage of event processing, the detector simulation.

8.5 Detector Simulation

To examine the response of the detector to the generated particles we use the CDF detector simulation algorithm QFL[S+92]. This program creates an event vertex, reconstructs the charged particle tracks in the tracking chambers, and calculates energy deposition in the calorimeters according to the resolutions given by test beam results. The QFL output banks are indistinguishable from

actual data production banks and can be analyzed with the same code.

QFL simulates all parts of the event that are passed along by HERWIG, including all the particle showers resulting from the underlying event and initial state gluon radiation created by HERWIG. The jet clustering algorithm may therefore find jets which were not generated by VECBOS. Similarly, additional energy arising from HERWIG-produced particle showers may be combined with the energy of VECBOS-generated parton jets, resulting in jets of higher energy than were initially generated. This means that, on occasion, an event for which the generated jet fails the jet cut will pass due to a high-energy HERWIG-produced jet. The jet-level cross sections will thus include contributions from effects not generated by VECBOS.

The simulation of a HERWIG output event may result in a phenomenon known as "feed-up," in which an event with N generated jets is reconstructed with $> N$ jets. Because we interpret VECBOS N-jet output to be inclusive over higher ($\geq N$-jet) multiplicities, we allow feed-up events to remain in our samples.

8.6 QCD Jet-Level Cross Sections

We obtain jet-level (post-simulation) cross sections for QCD $Z^0 + N$ jet events after allowing the weighted generated events to undergo fragmentation and detector simulation. For the cross section determination we assume that all the Z^0 bosons generated are actually reconstructed. In other words, when running the data analysis code on the QCD output banks, we make no cuts on the quality of the leptons or the Z^0. This presents a technical problem, because the proper counting of jets is dependent on the prior identification of electrons

arising from Z^0 decay. The similarity of jet and electron clustering methods makes it necessary to remove electron candidates by hand from the potential jet sample. To circumvent this difficulty we use VECBOS $Z^0 \rightarrow \nu_e\overline{\nu_e}+N$ jet events for our cross section measurement, adjusting for the difference in branching fraction by dividing the resulting number by the measured ratio[Par94]

$$\frac{\Gamma(Z^0 \rightarrow \nu_e\overline{\nu_e})}{\Gamma(Z \rightarrow e^+e^-)} = 1.98 \pm 0.05. \tag{8.6}$$

The neutrinos are noninteracting and therefore do not interfere with jet counting. The cross section result is scaled by the vertex cut efficiency, with the requirement $|z| < 60$ cm.

An event is considered for the cross section determination if the number of jets reconstructed, and passing the "good jet" cuts given in Section 7.4, equals or exceeds the number of partons generated. The weights of these events are added, and the resulting sum is divided by the branching fraction ratio given in Equation 8.6 and by the vertex efficiency. The cross sections thus obtained are tabulated in Table 8.2. They are compared to CDF data in Section 9.2.3.

8.7 QCD Differential Distributions

To obtain QCD events in which the Z^0 and jets can be compared directly to data, the unit-weight $Z \rightarrow e^+e^-$ + hadron events generated by the VECBOS-HERWIG Monte Carlo calculation are processed through the QFL simulation of the CDF detector. The response of the detector to the electrons and hadrons is recorded in the same format as the experimental data. The analysis program used to select the Z^0 boson and jets from the data is applied to the QCD-simulated $Z \rightarrow e^+e^-$ + jet events. Those QCD events passing the Z^0 selection

Table 8.2: Jet-Level Cross Sections $B(Z \to e^+e^-)\sigma(\bar{p}p \to Z^0 + \geq N$ jets), in pb

	$B(Z \to e^+e^-)\sigma$ (pb)		
N Jets	no gluon radiation	limited gluon radiation $< \langle p_T \rangle$	unlimited gluon radiation $< \sqrt{M_Z^2 + p_{TZ}^2}$
VECBOS $Q^2 = \langle p_T \rangle^2$			
≥ 1	29.39 ± 0.50	30.3 ± 0.47	35.16 ± 0.54
≥ 2	6.58 ± 0.24	7.97 ± 0.29	10.53 ± 0.38
≥ 3	1.50 ± 0.14	1.98 ± 0.13	2.44 ± 0.17
VECBOS $Q^2 = M_Z^2 + p_{TZ}^2$			
≥ 1	23.23 ± 0.37	24.0 ± 0.37	26.82 ± 0.40
≥ 2	3.97 ± 0.13	4.75 ± 0.14	5.77 ± 0.16
≥ 3	0.785 ± 0.081	1.05 ± 0.08	1.229 ± 0.084

cuts are written to a final data summary file which includes jets as defined for the data (see Section 7.4.3).

This procedure is costly in that many generated events are lost in 1) the unweighting, 2) the selection of good electrons, 3) the identification of the Z^0 and 4) the requirement that the number of reconstructed jets must match or exceed the number of partons generated. The relative number of events lost grows as the jet multiplicity increases, so that larger samples must be generated to obtain adequate statistics for $N \geq 3$ jets. However, once this is done the comparison of the QCD predictions to the data is extremely straight-forward. If the data sample has $\geq N$ jets, we use the QCD sample with $\geq N$ jets from N generated partons, as dictated by our interpretation of VECBOS calculations as inclusive over higher multiplicities. In Chapter 9 we show plots of various differential distributions as seen in the data and as predicted by QCD, using $Q^2 = \langle p_T \rangle^2$ in VECBOS and a limit on the magnitude of gluon radiation given

by $< \sqrt{M_Z^2 + p_{T_Z}^2}$ in HERWIG. For each plot we normalize the QCD prediction to the number of events in the appropriate data sample.

In order to show the sensitivity of the QCD predictions to the allowed level of gluon radiation in fragmentation, we calculate the Z^0 + 1 jet QCD predictions for different fragmentation processes. We choose three cases:

1. $Q^2{}_{VEC} = \langle p_T \rangle^2$,
   gluon radiation $< \langle p_T \rangle$.

2. $Q^2{}_{VEC} = \langle p_T \rangle^2$,
   gluon radiation $< \sqrt{M_Z^2 + p_{TZ}^2}$.

3. $Q^2{}_{VEC} = \langle p_T \rangle^2$,
   no gluon radiation.

Figure 8.3 shows the resulting E_T spectrum of the leading jet for each case. We find that the shape of the distribution corresponding to no allowed gluon radiation is somewhat softer than the other two and is in fact in very poor agreement with the distribution with unlimited radiation, with a $\chi^2 = 46.2/13$ $d.o.f.$ The distribution for events with unlimited radiation has a comparative deficiency of entries in the low-E_T region. Nevertheless, the two distributions with allowed gluon radiation are in overall good agreement, yielding $\chi^2 = 15.4/13$ $d.o.f.$

Figure 8.4 shows a comparison of the $|cos\Theta^*|$ distributions for the three fragmentation schemes. The angle Θ^* is the angle between the Z^0 and the bisector of the p and $-\bar{p}$ directions in the center-of-mass frame of the Z^0 and the leading jet in the event. Here we perceive a considerable difference between

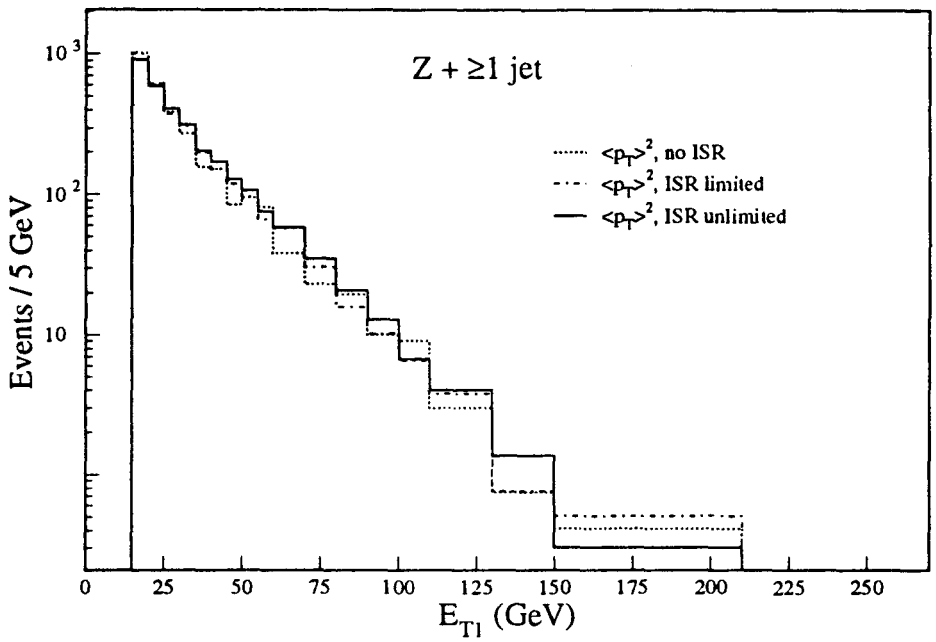

Figure 8.3: Transverse energy E_T of the leading jet in QCD events with three levels of allowed gluon radiation at fragmentation.

the three distributions, with the forward (high-$|cos\Theta^*|$) region much more populated for events with full gluon radiation. As the permitted gluon radiation is reduced, the distribution flattens, actually turning over at large $|cos\Theta^*|$ for the sample with no gluon radiation. As will be seen in Chapter 9, Figure 9.5, the data are in excellent agreement with the full-gluon-radiation distribution and do not exhibit the behavior of the limited- or no-gluon-radiation QCD samples.

Finally, in Figure 8.5, we present the pseudorapidity distribution of the leading jet for the three fragmentation samples. Although the two distributions corresponding to allowed gluon radiation agree very well ($\chi^2 = 15.7/19$ $d.o.f.$), the shape of the distribution with no gluon radiation is much more sharply peaked

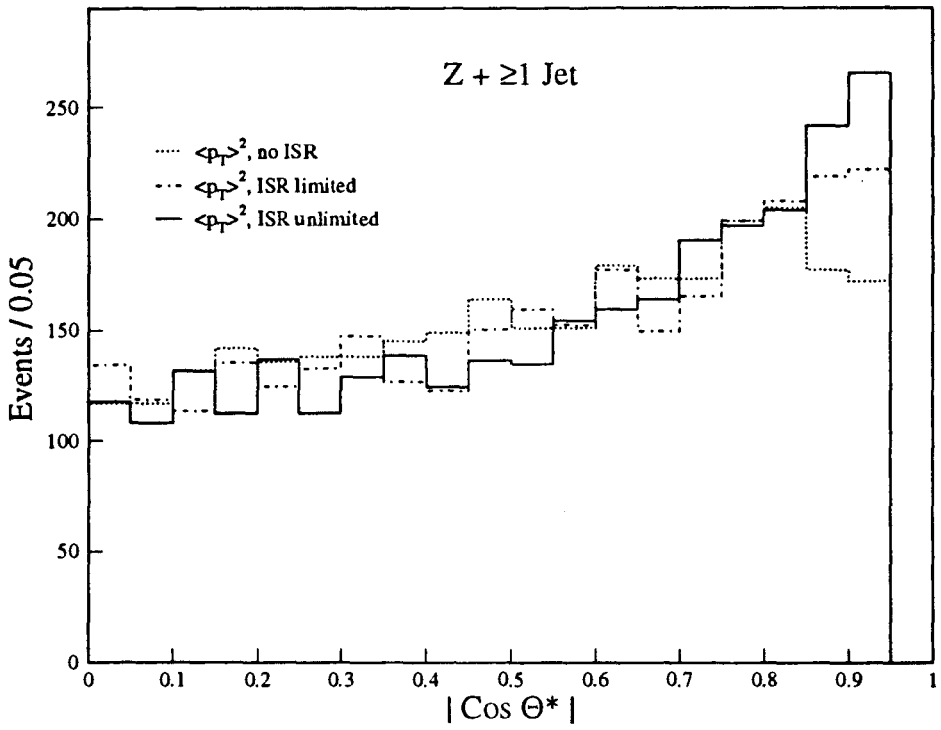

Figure 8.4: The $|cos\Theta^*|$ distribution for the range $|cos\Theta^*| < 0.95$ for QCD events with one or more jets and three levels of allowed gluon radiation at fragmentation.

in the central region. Once again, the data bear out the broader distribution predicted by the QCD samples with some gluon radiation (see Figure 9.6).

We conclude that the dependence of the QCD results on the level of allowed gluon radiation at fragmentation is evident in both the cross section determination and in the investigation of the kinematic distributions of $Z \rightarrow e^+e^- +$ jet events.

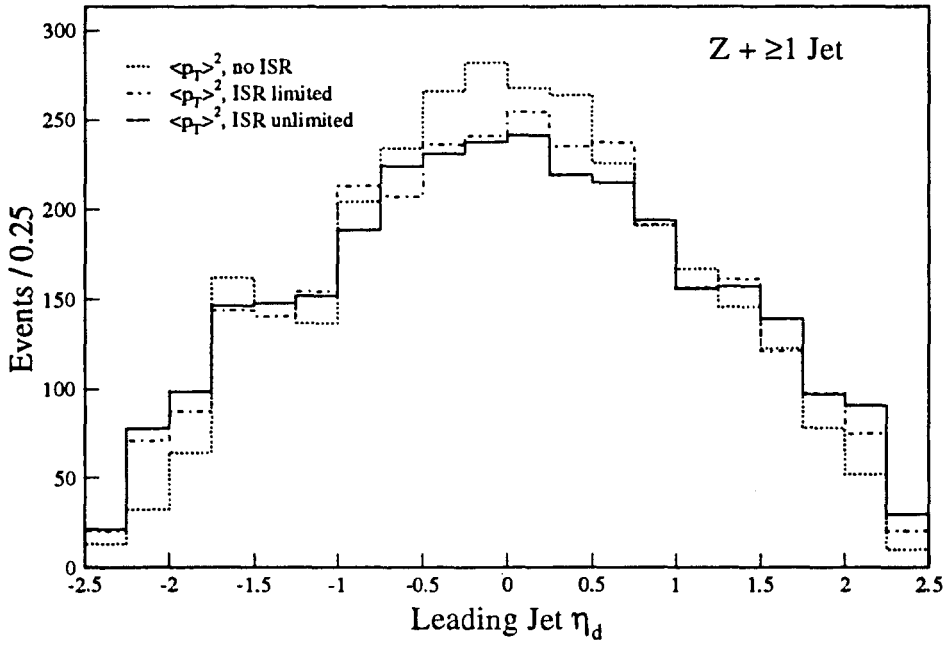

Figure 8.5: The distribution in pseudorapidity η of the leading jet in Z^0 + jet QCD events with three levels of allowed gluon radiation at fragmentation.

Chapter 9

Results

9.1 Introduction

The purpose of this analysis is twofold. In addition to obtaining a precise measurement of the $Z^0 + \geq N$ jet cross sections in our 106 pb^{-1} data sample, we wish to determine the reliability of leading-order QCD in accurately modeling Z^0 + jets, and by extension W + jets, production. There are several ways to compare data and QCD. In the data, one can attempt to unfold the detector resolution effects to reconstruct the partons at fragmentation level or even, banking on a full understanding of the fragmentation effects, reconstruct the generator-level partons. Conversely, one can use generated partons and pass them through fragmentation and detector simulation algorithms to emulate the data. We opt for the latter method in this analysis. Our approach leaves us free to explore the effects of different mass scales at the generator and fragmentation levels on the final QCD event sample without having to manipulate data in an effort to match the model we are testing.

We compare our data results to QCD predictions in two ways. First, we compare the measured cross sections for the $Z^0 + \geq N$ jet events to the

cross sections for fully reconstructed QCD-predicted events. Secondly, we plot Z^0 and jet variables as well as correlated jet-jet variables for data and QCD events to observe how well QCD models the kinematic properties of $Z^0 + \geq N$ jet events. The results of both of these comparisons are given in this chapter.

9.2 Cross Sections

Using the tools and event samples developed in Chapters 7 and 8, we now progress to the direct comparison of the $Z^0 + N$ jet cross sections calculated for the data to those predicted by QCD. Ideally, if the QCD calculation is done to all orders, and if all the detector acceptances and efficiencies for the data have been measured correctly, the ratio between the data cross sections and the QCD cross section should be 1. For the LO calculation available to us, in which higher-order corrections are absent, we expect r to be in the range 1–2. We will examine this ratio in Section 9.2.3.

9.2.1 Data Cross Sections

We use the *ratio method* and the measured[A+95c] inclusive Z^0 production cross section to obtain relative $Z^0 + \geq N$ Jet cross sections with reduced systematic uncertainties, as described in detail in Section 7.2. The results of the measurement, with all the statistical and systematic errors listed, are given in Table 9.1. Figure 9.1 shows a plot of the cross sections versus the inclusive jet multiplicities for the data and for a range of QCD predictions. The errors on the data are all the statistical and systematic uncertainties taken in quadrature, as given in Table 9.3.

Note that the cross section ratios $\sigma(N)/\sigma(N-1)$ are included in Table 9.1.

Table 9.1: $Z^0 + \geq N$ Jet Cross Sections. The first error listed is the statistical error, the second error is the systematic due to uncertainties in the Z^0 acceptance corrections. The third error is a common systematic error of 5.2% from the input inclusive Z^0 cross section. The last error reflects the jet-counting uncertainties.

N_j	σ(N)/σ(N-1)	σ(N)/σ(Incl.)	$BR \times \sigma$ (pb)
≥ 0		$\equiv 1.0$	$\equiv 231 \pm 12$
≥ 1	0.201 ± 0.007	0.2010 ± 0.0066	$46.4 \pm 1.2 \pm 0.9 \pm 2.4 \pm 4.9$
≥ 2	0.215 ± 0.014	0.0432 ± 0.0030	$10.0 \pm 0.6 \pm 0.3 \pm 0.5 \pm 1.7$
≥ 3	0.209 ± 0.027	0.0090 ± 0.0013	$2.08 \pm 0.28 \pm 0.10 \pm 0.11 \pm 0.48$
≥ 4	0.211 ± 0.059	0.0019 ± 0.0006	$0.44 \pm 0.14 \pm 0.03 \pm 0.02 \pm 0.10$

In Chapter 3 we discussed work by Berends *et al.*[BKTG91] in which the authors predict a constant value for $\sigma(N)/\sigma(N-1)$ of 0.22 for a jet clustering cone size of 0.4 and jet selection cuts $E_T > 15$ GeV and $|\eta| < 2$. In our measurement the ratio is indeed found to be constant, with a value of about 0.21 for jet multiplicities $N = 1$–4, in remarkable agreement with the LO QCD predicted behavior.

The data cross sections as a function of jet multiplicity are almost perfectly described by the exponential function

$$\mathrm{B}(Z \to e^+e^-)\sigma(Z^0 + N\text{jets}) = (231 \pm 12)e^{-\beta N} \text{ pb}$$

where N is the inclusive jet multiplicity and $\beta = 1.574 \pm 0.058$ denotes the magnitude of the slope (the error on β does not include the small effects from the fact that the cross section errors are correlated).

9.2.2 QCD Cross Sections

The QCD cross sections for Z^0 events containing 1, 2, or 3 jets, which we compare to our measured cross sections, are obtained after fragmentation and

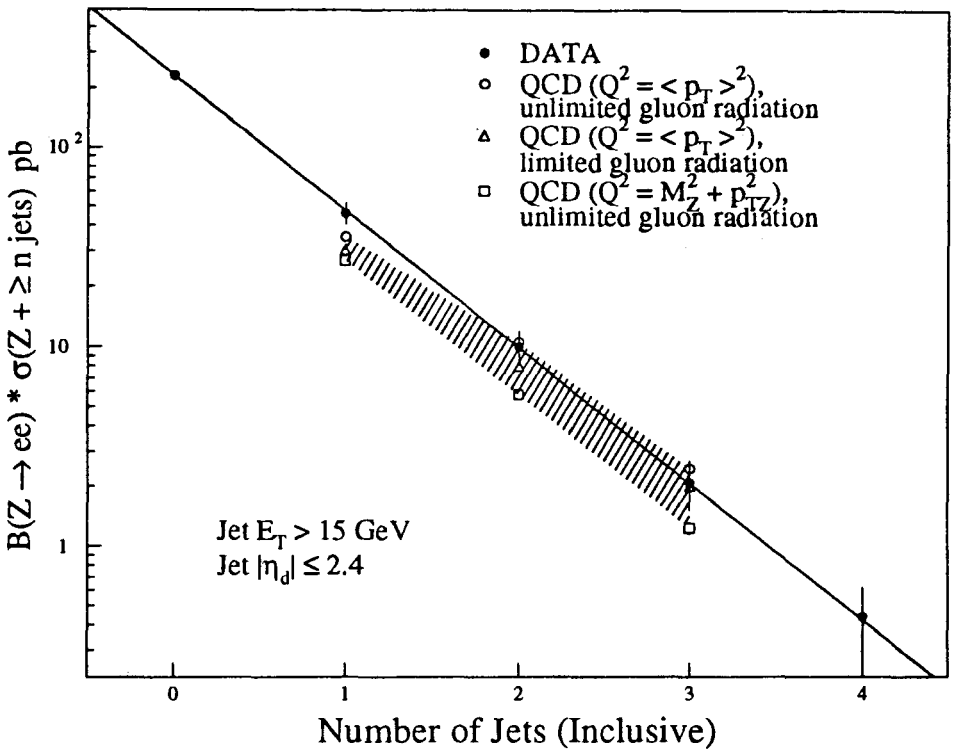

Figure 9.1: $B(Z \rightarrow e^+e^-)\sigma(Z^0 + \geq N\text{jets})$ plotted as a function of N. The shaded band indicates the range of the calculated QCD predictions.

detector simulation of the QCD events, as described in Chapter 8. To calculate the QCD cross sections, we apply our final jet cuts to the QCD events, but we assume full Z^0 decay acceptance. We require that at least N jets be reconstructed for each event in which N partons were generated. The results of our QCD cross section determinations are given in Table 9.2. Q^2 refers to the scale used for renormalization and factorization in the LO matrix element calculation.

In two cases the magnitude of the gluon radiation used in fragmentation

Table 9.2: $Z \rightarrow e^+e^- + N$ Jet QCD Cross Sections. The error shown is the statistical error. All cross sections are from LO calculations except for the inclusive (≥ 0 jet) cross section which is NNLO

N_j	Q^2 Scale	$BR \times \sigma$ (pb)	σ(N)/σ(N-1)	σ(N)/σ(Incl.)
≥ 0	M_Z^2	222.5 $\pm$ 1.1		
Gluon radiation limited to $< \sqrt{M_Z^2 + p_{T_Z}^2}$				
≥ 1	$\langle p_T \rangle^2$	35.16 $\pm$ 0.54	0.1580 $\pm$ 0.0025	0.1580 $\pm$ 0.0025
≥ 2	$\langle p_T \rangle^2$	10.53 $\pm$ 0.38	0.300 $\pm$ 0.012	0.0473 $\pm$ 0.0017
≥ 3	$\langle p_T \rangle^2$	2.44 $\pm$ 0.17	0.232 $\pm$ 0.018	0.0110 $\pm$ 0.0008
≥ 1	$M_Z^2 + p_{T_Z}^2$	26.82 $\pm$ 0.40	0.1205 $\pm$ 0.0019	0.1205 $\pm$ 0.0019
≥ 2	$M_Z^2 + p_{T_Z}^2$	5.77 $\pm$ 0.16	0.2151 $\pm$ 0.0068	0.0259 $\pm$ 0.0007
≥ 3	$M_Z^2 + p_{T_Z}^2$	1.229 $\pm$ 0.084	0.213 $\pm$ 0.016	0.0055 $\pm$ 0.0004
Gluon radiation limited to $< \langle p_T \rangle$				
≥ 1	$\langle p_T \rangle^2$	30.3 $\pm$ 0.47	0.1362 $\pm$ 0.0022	0.1362 $\pm$ 0.0022
≥ 2	$\langle p_T \rangle^2$	7.97 $\pm$ 0.29	0.263 $\pm$ 0.010	0.0358 $\pm$ 0.0013
≥ 3	$\langle p_T \rangle^2$	1.98 $\pm$ 0.13	0.248 $\pm$ 0.019	0.0089 $\pm$ 0.0006

is kinematically limited to $< \sqrt{M_Z^2 + p_{T_Z}^2}$. In the third instance the gluon radiation limit is reduced to $< \langle p_T \rangle$. The band dilineated by these predictions is compared to the data cross section measurement in Figure 9.1.

9.2.3 r-factors

To compare the measured $Z^0 + \geq N$ jet cross sections to those predicted by QCD, we take their ratios at each jet multiplicity. This ratio we will refer to as the r-factor, where

$$r = \frac{\sigma_{\text{data}}}{\sigma_{\text{QCD}}}.$$

Table 9.3 shows the r-factors obtained for jet multiplicities n = 1, 2, and 3. For completeness the r-factor for the inclusive cross sections is also shown, although these are numbers taken from another analysis[A+95c] and are not

Table 9.3: $Z^0 + N$ Jet Cross Section r-factors. The error shown includes the statistical and systematic uncertainties taken in quadrature. The cross sections are given in pb.

N_j	$BR \times \sigma$ (Data)	$BR \times \sigma$ (QCD)	Order	Q^2 Scale	$r = \frac{\sigma_{data}}{\sigma_{QCD}}$
≥ 0	231 ± 12	222.5 ± 1.1	NNLO	M_Z^2	1.01 ± 0.05
Gluon radiation limited to $< \sqrt{M_Z^2 + p_{T_Z}^2}$					
≥ 1	46.4 ± 5.7	35.16 ± 0.54	LO	$\langle p_T \rangle^2$	1.32 ± 0.16
≥ 2	10.0 ± 1.9	10.53 ± 0.38	LO	$\langle p_T \rangle^2$	0.95 ± 0.19
≥ 3	2.08 ± 0.58	2.44 ± 0.17	LO	$\langle p_T \rangle^2$	0.85 ± 0.24
≥ 1	46.4 ± 5.7	26.82 ± 0.40	LO	$M_Z^2 + p_{T_Z}^2$	1.73 ± 0.21
≥ 2	10.0 ± 1.9	5.77 ± 0.16	LO	$M_Z^2 + p_{T_Z}^2$	1.73 ± 0.34
≥ 3	2.08 ± 0.58	1.229 ± 0.084	LO	$M_Z^2 + p_{T_Z}^2$	1.70 ± 0.48
Gluon radiation limited to $< \langle p_T \rangle$					
≥ 1	46.4 ± 5.7	30.30 ± 0.47	LO	$\langle p_T \rangle^2$	1.53 ± 0.19
≥ 2	10.0 ± 1.9	7.97 ± 0.29	LO	$\langle p_T \rangle^2$	1.25 ± 0.24
≥ 3	2.08 ± 0.58	1.98 ± 0.13	LO	$\langle p_T \rangle^2$	1.05 ± 0.29

measured here. The errors on the cross section numbers are all the statistical and systematic errors from the above tables taken in quadrature.

We find that the quantitative agreement between the data and the two QCD samples generated with $Q^2 = \langle p_T \rangle^2$ is better than for QCD generated at the higher Q^2 value. That is, the ratios r between the data and the QCD-predicted cross sections are closer to unity for this Q^2 (see Figure 9.1). However, the r-factors are not constant; they decrease with increasing jet multiplicity, indicating that the number of jets reconstructed depends strongly on initial state gluon radiation at the fragmentation level. Such dependence is also clearly evident in the disparity between the $Q^2 = \langle p_T \rangle^2$ cross sections for limited and unlimited allowed gluon radiation.

Table 9.3 and Figure 9.1 indicate that the QCD prediction at $Q^2 = M_Z^2 + p_{T_Z}^2$ yields cross sections that are systematically lower than those measured

in the data. Yet we note that the r-factors in this case are constant over all jet multiplicities, indicating a reduced dependence of the multiplicities on fragmentation effects.

9.3 Comparison of Measured Jet Differential Distributions to QCD Predictions

A complementary way to test the reliability of a QCD algorithm such as VECBOS[BKTG91] in modeling heavy boson plus jets production is to examine the kinematic properties of the Z^0 and the jets after detector simulation, and to compare them to similar properties observed in the data. There is a plethora of distributions from which to choose in making such comparisons. In addition to the differential E_T distributions of the jets, for example, we investigate variables which depend on the correlations between multiple jets generated in an event. Among these are the invariant mass of the two highest-E_T jets, the jet-jet separation, and the scalar sum of the jet E_Ts.

The QCD event samples which are used in these comparisons are generated with VECBOS using $Q^2 = \langle p_T \rangle^2$ and fragmented by HERWIG[MW88, M$^+$92], where gluon radiation is limited to $< \sqrt{M_Z^2 + p_{T_Z}^2}$. Studies have shown that this places essentially no restriction on the allowed radiation within the kinematic limits. The events are processed through a detector simulation algorithm and analyzed analogously to the data. In addition to the jet selection criteria we also require the events to pass all the boson selection cuts. In our comparisons we normalize the QCD predictions to the number of events in the corresponding data samples. The χ^2 values quoted for the distribution comparisons are calculated by combining low-statistics bins (containing fewer than 5 entries)

with the bin containing the largest number of entries. This method reduces the significance of bins with a small number of counts.

In Figure 9.2 we show the differential E_T spectra for the leading (highest-E_T) jet in the Z^0 events containing ≥ 1, ≥ 2, and ≥ 3 jets. The E_T plots have been corrected for the estimated contribution of X-jets[1] to the samples, which affects primarily the low-E_T bins. The agreement between the QCD prediction and the data is quite good. A χ^2 test gives $\chi^2 = 16.3/12$ *d.o.f.* for the $Z^0 + \geq 1$ jet plot, $\chi^2 = 7.5/10$ *d.o.f.* for the $Z^0 + \geq 2$ jet plot, and $\chi^2 = 3.0/3$ *d.o.f.* for the $Z^0 + \geq 3$ jet plot.

The E_T distributions for the next-to-leading jet in Z^0 events with ≥ 2 and ≥ 3 jets are shown in Figure 9.3. The agreement is very good for the $Z^0 + \geq 2$ jet case, yielding $\chi^2 = 3.8/4$ *d.o.f.* In the three-jet plot, the poor statistics do not allow a meaningful χ^2 comparison, though for the record it gives $\chi^2 = 6.5/3$ *d.o.f.*

For completeness we also show the E_{T3} spectrum for events with three or more jets. Here the QCD prediction appears to follow the shape of the measured distribution quite well, though there is some disagreement in the $15 - 20$ GeV bin. In all the E_T spectra above, the low-E_T bins are the most sensitive to the effects of gluon radiation in the fragmentation of QCD events; the largest discrepancies between data and QCD are expected in the low-E_T region. However, limiting the gluon radiation at fragmentation level results in overall poorer agreement between the QCD and measured E_T distributions.

To determine whether VECBOS correctly models the angular distribution of Z^0 bosons produced with jets, we look at events containing one or more jets

[1] X-jets are jets which come from additional interaction vertices in an event crossing. They are discussed in detail in Section 7.4.4.

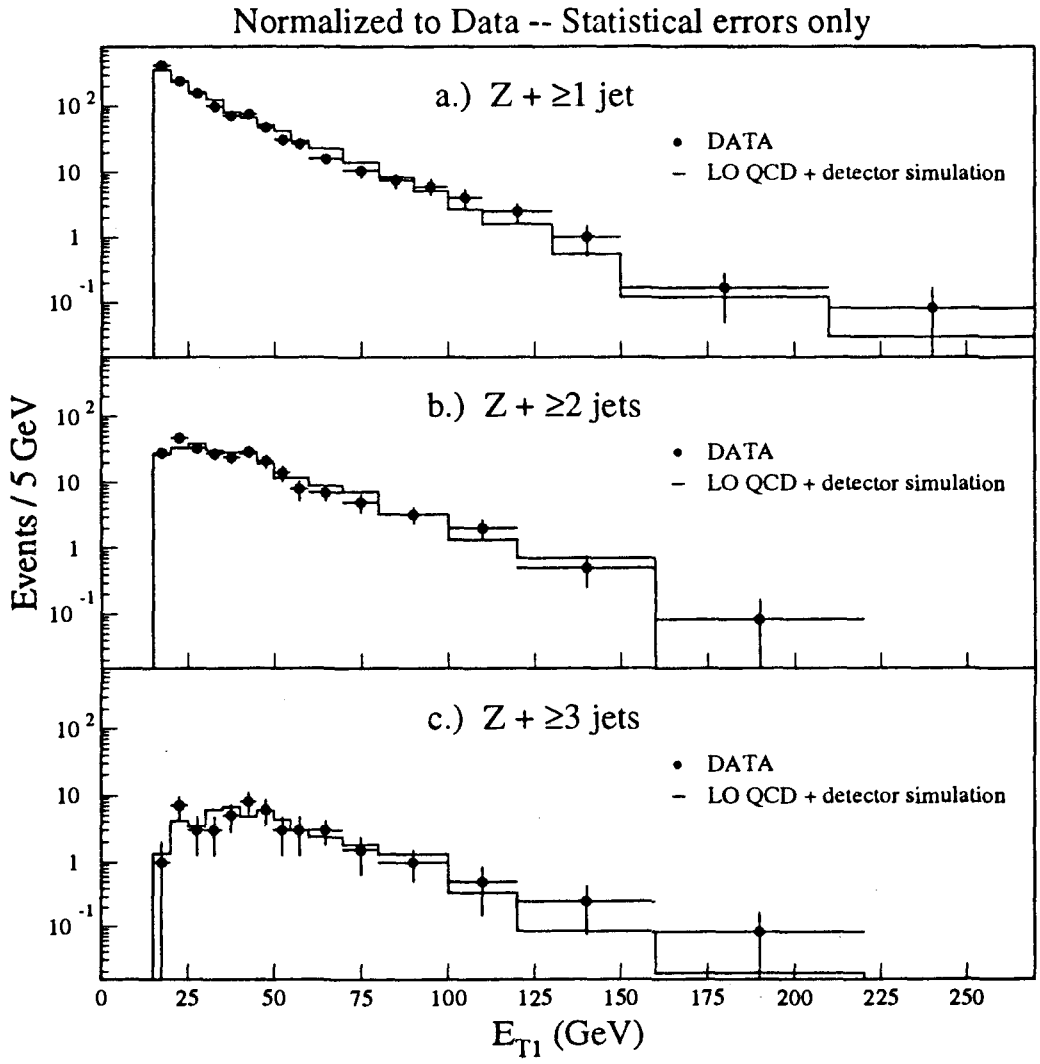

Figure 9.2: Transverse energy E_T of the leading jet in a.) $Z^0 + \geq 1$ jet events, b.) $Z^0 + \geq 2$ jet events, and c.) $Z^0 + \geq 3$ jet events.

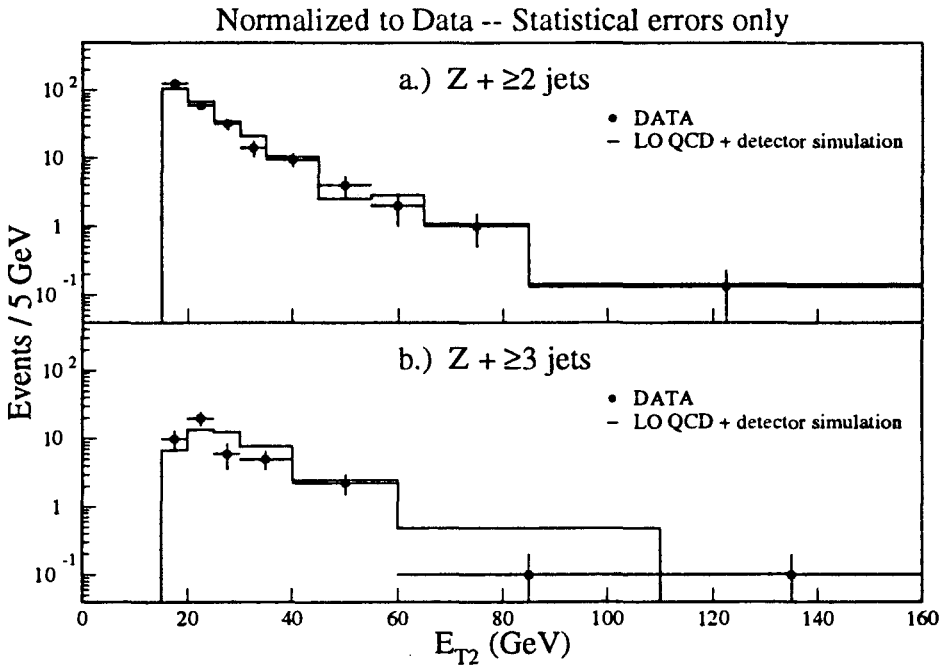

Figure 9.3: Transverse energy E_T of the next-to-leading jet in a.) $Z^0 + \geq 2$ jet events and b.) $Z^0 + \geq 3$ jet events.

in the center-of-mass frame of the Z^0 and the leading jet. In this frame, the angle Θ^* is defined to be the angle between the Z^0 and the bisector of the p and $-\overline{p}$ directions. In Figure 9.5, we show the distribution $|cos\Theta^*|$ for $|cos\Theta^*| < 0.95$. The region near $|cos\Theta^*| = 1$ is very sensitive to detector acceptance effects and is not included in the comparison. The agreement between the predicted and measured distributions is excellent, with $\chi^2 = 18.3/18$ $d.o.f.$

Of similar importance is the distribution of the reconstructed jets in pseudorapidity. Figure 9.6 shows this distribution for the leading jet in $Z^0 + \geq 1$

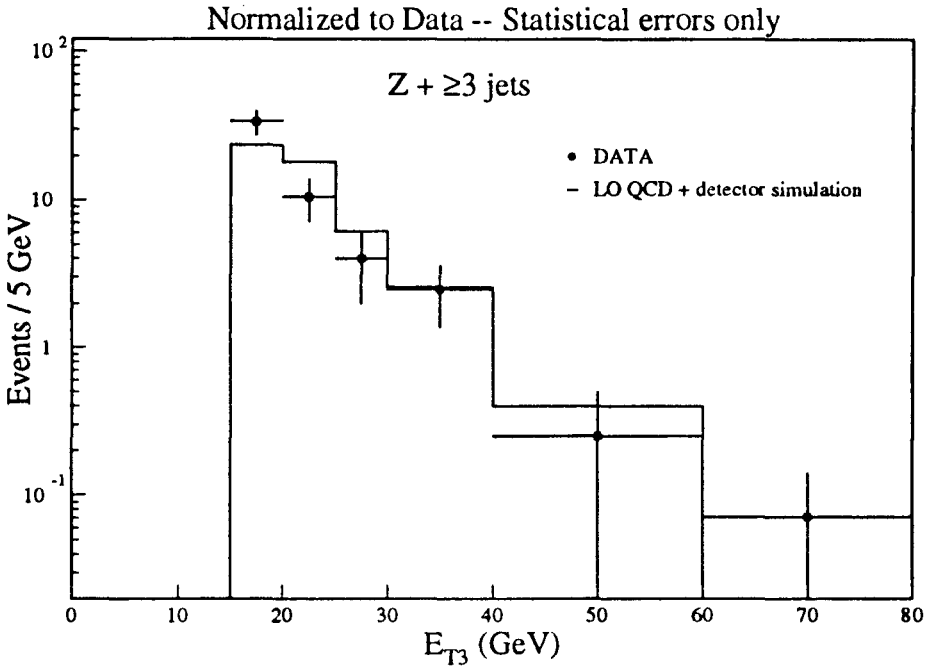

Figure 9.4: The E_T distribution for the third-highest-E_T jet in $Z^0 + \geq 3$ jet events.

jet events. The agreement is good for negative pseudorapidities, but at positive η the data exhibit a peculiar structure which may indicate a sensitivity to detector problems. Nevertheless, the predicted shape matches the overall measured shape fairly well. The χ^2 comparison gives $\chi^2 = 24.9/19$ *d.o.f.*

A Monte Carlo such as VECBOS, which models heavy boson plus jet production, must reproduce the kinematic distributions of the Z^0 or W and of the jets that are observed in the data. In events with multiple jets, it must also reproduce the distributions of correlated jet variables, such as the dijet invariant mass. We turn our attention to variables which carry information about the relationship between jets in Z^0 + multijet events.

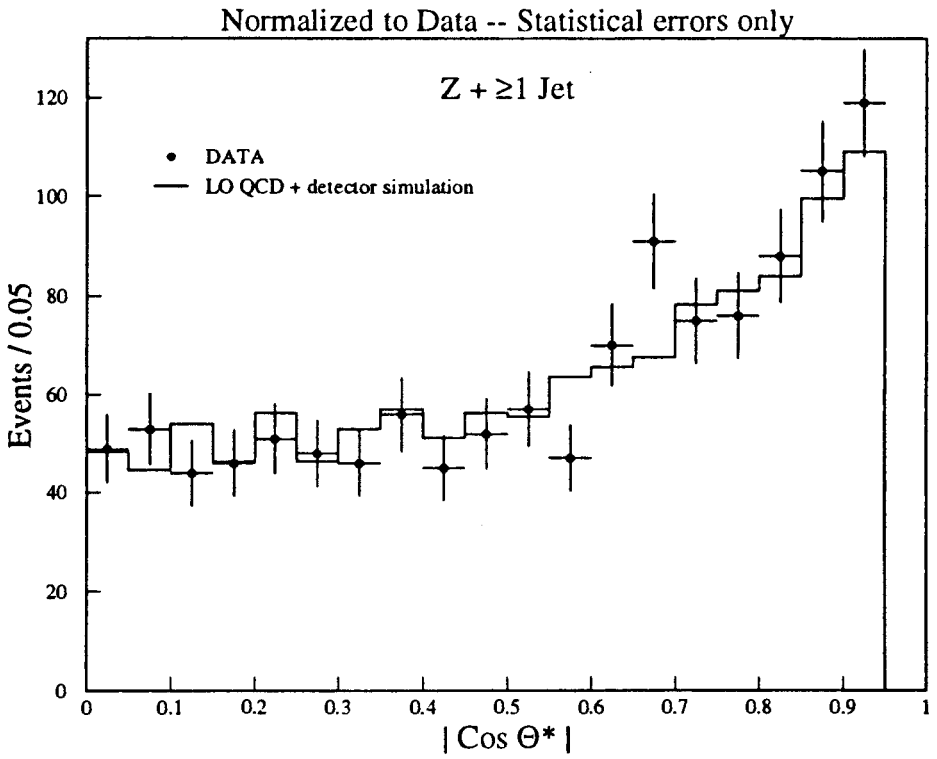

Figure 9.5: The $|cos\Theta^*|$ distribution for the range $|cos\Theta^*| < 0.95$ for events with one or more jets.

The first distribution we present is the scalar sum of the transverse energies of two jets. Figure 9.7 a.) shows the E_T sum of the two leading jets in events with two or more jets; in Figure 9.7 b.) we present the E_T sum for the second- and third-highest-E_T jets in events with three or more jets. These plots have not been corrected for the contribution from X-jets. As we expect this contribution to manifest itself in the lowest-E_T bins, it is not surprising that the discrepancy between QCD prediction and the data should be especially large there. Nevertheless, the $E_{T1} + E_{T2}$ plot shows good overall agreement between

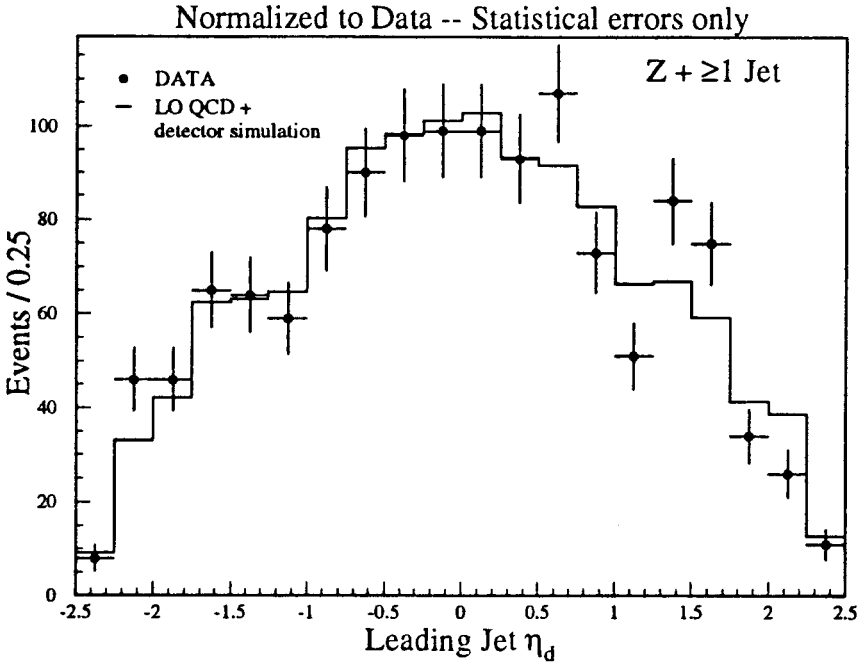

Figure 9.6: The distribution in pseudorapidity η of the leading jet in Z^0 + jet events.

the calculated and measured spectra, with a χ^2 value of 5.7/7 *d.o.f.* For the $E_{T2}+E_{T3}$ distribution the agreement is quite poor, yielding $\chi^2 = 13.0/3$ *d.o.f.*

Another interesting quantity to investigate is the invariant mass of the two leading jets in events with two or more jets. This spectrum is one of the most likely to reveal the presence of new physics, where the unknown particle decays hadronically. In the M_{jj} distribution shown in Figure 9.8, we observe structure in the data in the range $100 < M_{jj} < 140$ GeV/c^2 which is not entirely reproduced in the QCD prediction. The overall χ^2 fit in the M_{jj} spectrum is $\chi^2 = 20.5/12$ *d.o.f.*, indicating poor agreement. However, if the region $100 < M_{jj} < 140$ GeV/c^2 is removed from consideration, the χ^2 improves

substantially to 7.1/8 *d.o.f.* We have studied the structure to ascertain if it is due to some error in lepton removal, and have found no evidence for this. Similar plots using jets in $Z \rightarrow \mu^+\mu^-$ and $W \rightarrow e\nu$ decay events do not show the bump. We are forced reluctantly to conclude that the bump in the $Z \rightarrow e^+e^-$ events represents a statistical fluctuation. This question will be investigated further as the statistics in the $Z \rightarrow e^+e^-+ \geq 2$ jet sample improve.

We turn finally to a plot of the separation of the two leading jets in Z^0 events with two or more jets, which is shown in Figure 9.9. The separation is given in $\Delta R_{jj} = \sqrt{\Delta\eta_{jj}^2 + \Delta\phi_{jj}^2}$. This plot is interesting because the effect of the level of allowed gluon radiation is clearly reflected in the shape of the distribution. Figure 9.9 a.) shows the comparison between data and QCD prediction for QCD events which have undergone limited gluon radiation at fragmentation level. The χ^2 value obtained for this comparison is 12.9/7 *d.o.f.*, indicating poor agreement. Figure 9.9 b.) shows the comparison for QCD events in which the gluon radiation was essentially unlimited. For this plot we obtain $\chi^2 = 8.3/7$ *d.o.f.*, which is a significant improvement.

It is clear that restricting the magnitude of the allowed gluon radiation restricts the angle at which final state gluon emission can occur, resulting in a greater degree of jet-jet colinearity (*i.e.*, more jet-jet correlation at small values of ΔR_{jj})—behavior which is not seen in the data. Other angular distribution variables, such as jet η and $cos\Theta^*$, also depend strongly on the allowed gluon radiation at fragmentation (see Section 8.7 and Figures 8.4 and 8.5), and seem to be in better agreement with the data for unlimited gluon radiation.

This fact, together with the quantitative agreement in the cross section *r*-factors for QCD events with substantial gluon radiation, has led to our choice of

the VECBOS Q^2 parameter and the magnitude of the allowed gluon radiation in HERWIG which we use in our data and QCD kinematic comparisons.

We have found that a comparison of the measured and QCD-predicted kinematic spectra for Z^0 + jet events show overall good agreement for the Z^0 and jet distributions as well as for jet-jet correlated quantities. The choice to show plots for QCD events in which the allowed gluon radiation at fragmentation level is essentially unlimited is motivated by the clear indication in the jet η, $cos\Theta^*$, and ΔR_{jj} distributions that it is in better agreement with the observed data than a lower gluon radiation cutoff.

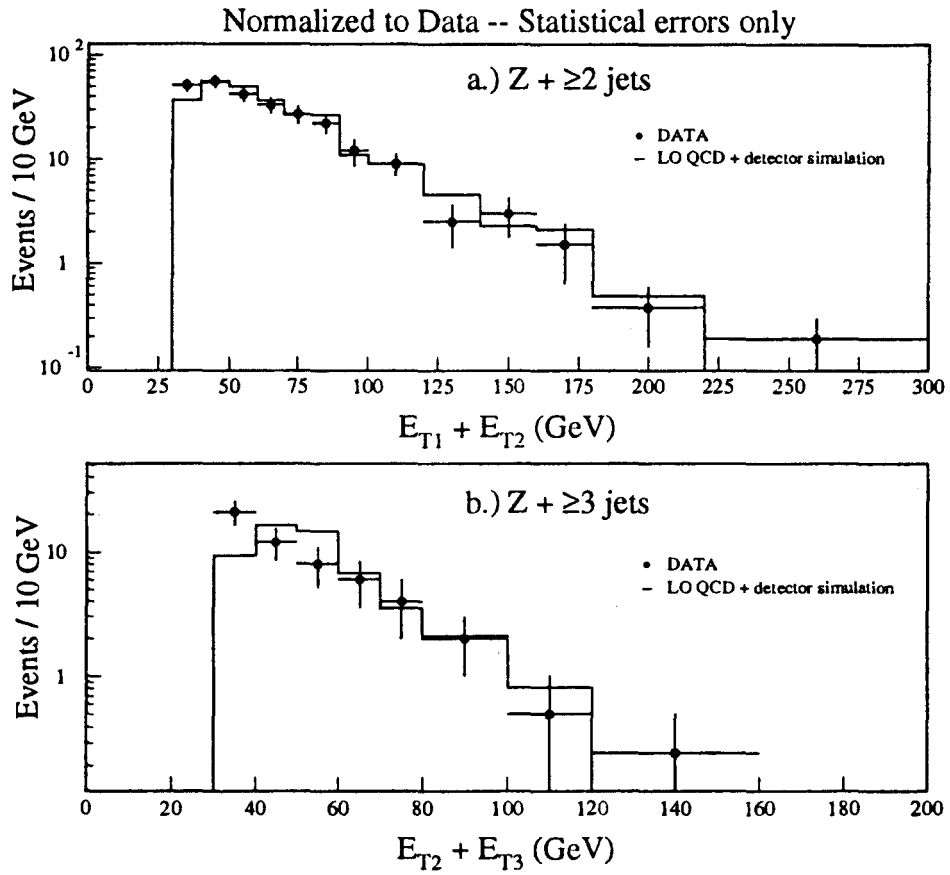

Figure 9.7: a.) Scalar E_T sum of the two leading jets in $Z^0 + \geq 2$ jet events; b.) E_T sum of the second- and third-highest-E_T jets in Z^0 events with three or more jets.

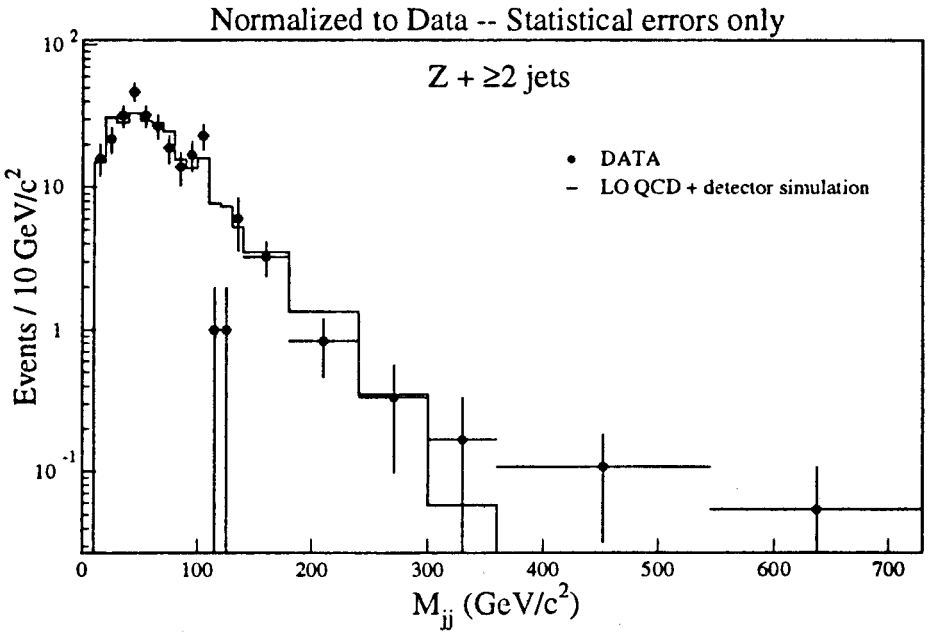

Figure 9.8: Invariant mass distribution of the two leading jets in Z^0 events with two or more jets.

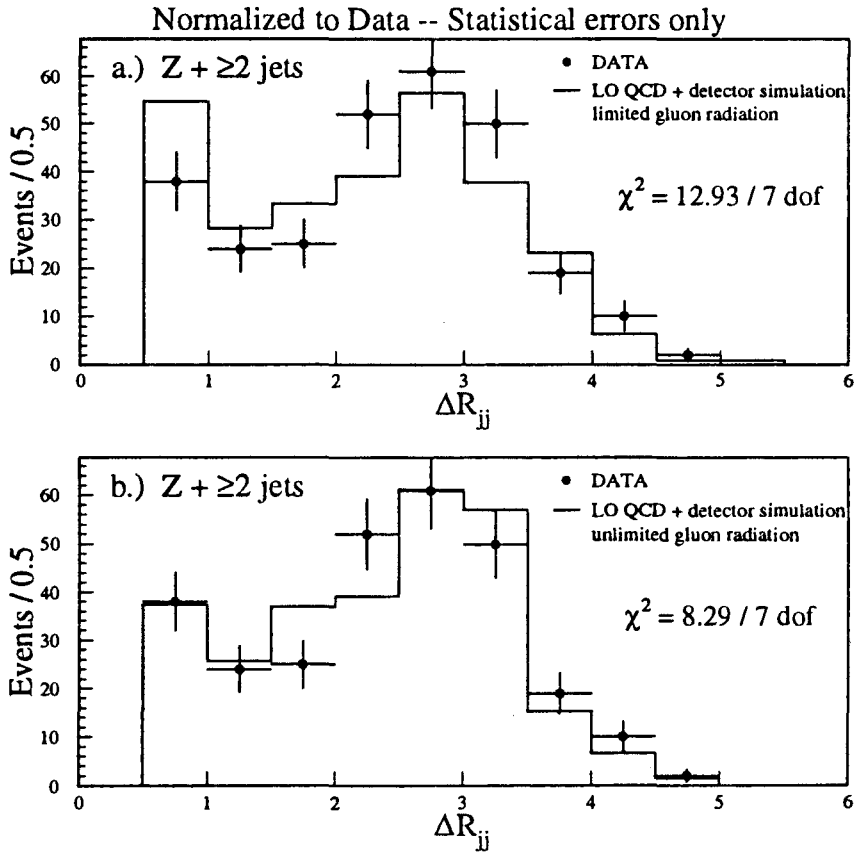

Figure 9.9: The separation in $\eta - \phi$ space between the two leading jets in $Z^0 + \geq 2$ jet events, for a.) limited gluon radiation in QCD event fragmentation, and b.) unlimited gluon radiation at fragmentation.

Chapter 10

Conclusions

We have measured the $Z \rightarrow e^+e^- + \geq N$ jet cross sections for jet multiplicities $N = 1 - 4$ using 6708 $Z \rightarrow e^+e^-$ decay candidates. The jets are clustered in cones of size 0.4 in $\eta - \phi$ space within a pseudorapidity range given by $|\eta| < 2.4$, and have a minimum E_T of 15 GeV. The behavior of the cross section value as a function of the jet multiplicity describes an exponential of the form $Ae^{-\beta N}$, where A is the inclusive $Z \rightarrow e^+e^-$ cross section $B(Z \rightarrow e^+e^-)\sigma = 231 \pm 12$ pb, and $\beta = 1.574 \pm 0.058$. The ratios $\sigma(N)/\sigma(N-1)$ are constant at about 0.21 for $N = 1 - 4$, which is in excellent agreement with the expected value of 0.22 given by Berends *et al.* for jets with $E_T > 15$ GeV and $|\eta| < 2.0$[BKTG91].

A search in the Z^0 + jets events for evidence of b-quark decay has yielded results which are in full agreement with the Standard Model predictions (see discussion in Section 7.5). An excess of b-tags in the Z^0 event sample would be a possible indication of new physics processes.

The ratios of the Z^0 + N jet cross sections measured in data and those predicted by QCD, which we call the r-factors, are an indicator of the degree to which the production of heavy bosons plus jets is understood and properly

modelled. We have calculated the r-factors for three types of QCD prediction:

1. $Q^2 = \langle p_T \rangle^2$ of the generated partons in VECBOS
   limited gluon radiation in HERWIG fragmentation

2. $Q^2 = \langle p_T \rangle^2$ of the generated partons in VECBOS
   full gluon radiation in HERWIG fragmentation

3. $Q^2 = M_Z^2 + p_{T_Z}^2$ in VECBOS
   full gluon radiation in HERWIG fragmentation.

We find that the best *quantitative* agreement, corresponding to r-factors closest to unity, is achieved for the second combination: a low Q^2 value at the generator level and unlimited gluon radiation at fragmentation. $Z^0 + 1$ jet cross sections obtained using a low Q^2 value at the generator level at leading order appear to approximate those obtained at NLO using a larger Q^2 value, if a 2-loop α_s evolution is employed in the calculation (see Section 8.3). In the absence of NLO calculations for the higher jet multiplicities, we assume that this holds for them, as well. Since the NLO calculation is more meaningful from a theoretical point of view, including tree-level as well as virtual contributions to the matrix element calculation, we are inclined to prefer the lower Q^2 value at LO generation which gives us the NLO cross section value.

For completeness, however, we also examine the cross section behavior for QCD calculations performed with a higher Q^2 at generator level. For this case, we obtain an r-factor which is constant over jet multiplicities. Though the QCD prediction is uniformly lower than the data cross section, one might argue that the *qualitative* behavior over all jet multiplicities investigated is better for the larger Q^2 at generation. Because the QCD prediction is given

by a LO calculation, the r-factors are in fact expected to lie somewhere in the range of 1–2. Table 9.3 clearly shows that the NNLO inclusive $B(Z \rightarrow e^+e^-)\sigma$ calculation, in which virtual diagrams are considered, agrees perfectly with the measured value ($r = 1.01 \pm 0.05$).

We determine qualitative agreement between data and QCD in a different way by comparing the shapes of various distributions obtained from the Z^0 and jets in the two event samples. For this study, we use QCD events of type 2 (see above). This choice is motivated by the fact that the ΔR_{jj}, jet η, and $cos\Theta^*$ plots for these parameters are in better agreement with the measured spectra than similar plots in which the allowed gluon radiation at fragmentation is either absent or limited.

The agreement between the measured and predicted kinematic distributions is excellent in almost every case. We conclude that LO VECBOS-generated events, in which substantial gluon radiation is allowed at fragmentation level, model heavy boson plus jet production well.

This analysis presents the first measurement of $Z^0 + N$ jet cross sections as a function of N. The data sample used consists of 6708 $Z \rightarrow e^+e^-$ decays collected over a three-year period at the Fermilab Tevatron by the CDF experiment. Continued running until early 1996 should increse the available statistics by another estimated 30–40%. Future studies using the combined $Z \rightarrow e^+e^-$ and $Z \rightarrow \mu^+\mu^-$ samples will improve the measurement; such event samples will also facilitate the extraction of the strong coupling α_s from a precision measurement of the Z^0 p_T. A cross section measurement analogous to that presented in this analysis is already underway for $W \rightarrow e\nu+$ jet events.

Appendix A

Derivation of the Central Electron Efficiency Equations

Definitions:

N_c = number of *events* in the central efficiency sample

N_t = number of *events* in which both electrons pass tight cuts

N_l = number of *events* in which one electron passes tight cuts and the other passes either tight or loose cuts

ϵ_{ct} = efficiency for a *single electron* to pass tight cuts

ϵ_{cl} = efficiency for a *single electron* to pass loose cuts

$\epsilon_f = 1 - \epsilon_{cl}$ = efficiency for a *single electron* to fail loose cuts.

A.1 The tight central electron efficiency

Since by design the efficiency sample N_c contains only events in which at least one of the electrons passes the tight cuts, we have

$$N_t = \frac{{\epsilon_{ct}}^2}{{\epsilon_{ct}}^2 + 2\epsilon_{ct}(\epsilon_{cl} - \epsilon_{ct}) + 2\epsilon_{ct}(1 - \epsilon_{cl})} \cdot N_c, \tag{A.1}$$

which simplifies to

$$N_t = \frac{\epsilon_{ct}}{2 - \epsilon_{ct}} \cdot N_c.$$

Solving for ϵ_{ct}, we obtain

$$\epsilon_{ct} = \frac{2N_t}{N_t + N_c}. \tag{A.2}$$

A.2 The loose central electron efficiency

The number of events passing the loose cuts is given by

$$N_l = \frac{{\epsilon_{ct}}^2 + 2\epsilon_{ct}(\epsilon_{cl} - \epsilon_{ct})}{{\epsilon_{ct}}^2 + 2\epsilon_{ct}(\epsilon_{cl} - \epsilon_{ct}) + 2\epsilon_{ct}(1 - \epsilon_{cl})} \cdot N_c, \tag{A.3}$$

which simplifies to

$$N_l = \frac{2\epsilon_{cl} - \epsilon_{ct}}{2 - \epsilon_{ct}} \cdot N_c.$$

Solving for ϵ_{cl}, we obtain

$$\epsilon_{cl} = \frac{N_l}{2N_c}(2 - \epsilon_{ct}) + \epsilon_{ct}. \tag{A.4}$$

Substituting Equation A.2 into Equation A.4 yields

$$\epsilon_{cl} = \frac{N_l}{2N_c}(2 - \frac{2N_t}{N_t + N_c} + \frac{2N_cN_t}{N_l(N_t + N_c)}).$$

This simplifies to

$$\epsilon_{cl} = \frac{N_l + N_t}{N_t + N_c}. \tag{A.5}$$

A.3 Special cases

We check the special cases:

1. If $N_l = N_c$ (*i.e.*, no loose cuts are applied), then

   $\epsilon_{cl} = 1$, as required.

2. If $N_l = N_t$ (*i.e.*, loose cuts are the same as tight), then

   $\epsilon_{cl} = \epsilon_{ct}$, as required.

Appendix B

The CDF Author List

F. Abe,[14] H. Akimoto,[32] A. Akopian,[27] M. G. Albrow,[7] S. R. Amendolia,[23] D. Amidei,[17] J. Antos,[29] C. Anway-Wiese,[4] S. Aota,[32] G. Apollinari,[27] T. Asakawa,[32] W. Ashmanskas,[15] M. Atac,[7] P. Auchincloss,[26] F. Azfar,[22] P. Azzi-Bacchetta,[21] N. Bacchetta,[21] W. Badgett,[17] S. Bagdasarov,[27] M. W. Bailey,[19] J. Bao,[35] P. de Barbaro,[26] A. Barbaro-Galtieri,[15] V. E. Barnes,[25] B. A. Barnett,[13] G. Bauer,[16] T. Baumann,[9] F. Bedeschi,[23] S. Behrends,[3] S. Belforte,[23] G. Bellettini,[23] J. Bellinger,[34] D. Benjamin,[31] J. Benlloch,[16] J. Bensinger,[3] D. Benton,[22] A. Beretvas,[7] J. P. Berge,[7] S. Bertolucci,[8] A. Bhatti,[27] K. Biery,[12] M. Binkley,[7] D. Bisello,[21] R. E. Blair,[1] C. Blocker,[3] A. Bodek,[26] W. Bokhari,[16] V. Bolognesi,[7] D. Bortoletto,[25] J. Boudreau,[24] L. Breccia,[2] C. Bromberg,[18] E. Buckley-Geer,[7] H. S. Budd,[26] K. Burkett,[17] G. Busetto,[21] A. Byon-Wagner,[7] K. L. Byrum,[1] J. Cammerata,[13] C. Campagnari,[7] M. Campbell,[17] A. Caner,[7] W. Carithers,[15] D. Carlsmith,[34] A. Castro,[21] D. Cauz,[23] Y. Cen,[26] F. Cervelli,[23] H. Y. Chao,[29] J. Chapman,[17] M.-T. Cheng,[29] G. Chiarelli,[23] T. Chikamatsu,[32] C. N. Chiou,[29] L. Christofek,[11]

S. Cihangir,[7] A. G. Clark,[23] M. Cobal,[23] M. Contreras,[5] J. Conway,[28] J. Cooper,[7] M. Cordelli,[8] C. Couyoumtzelis,[23] D. Crane,[1] D. Cronin-Hennessy,[6] R. Culbertson,[5] J. D. Cunningham,[3] T. Daniels,[16] F. DeJongh,[7] S. Delchamps,[7] S. Dell'Agnello,[23] M. Dell'Orso,[23] L. Demortier,[27] B. Denby,[23] M. Deninno,[2] P. F. Derwent,[17] T. Devlin,[28] M. Dickson,[26] J. R. Dittmann,[6] S. Donati,[23] J. Done,[30] A. Dunn,[17] N. Eddy,[17] K. Einsweiler,[15] J. E. Elias,[7] R. Ely,[15] E. Engels, Jr.,[24] D. Errede,[11] S. Errede,[11] Q. Fan,[26] I. Fiori,[2] B. Flaugher,[7] G. W. Foster,[7] M. Franklin,[9] M. Frautschi,[31] J. Freeman,[7] J. Friedman,[16] H. Frisch,[5] T. A. Fuess,[1] Y. Fukui,[14] S. Funaki,[32] G. Gagliardi,[23] S. Galeotti,[23] M. Gallinaro,[21] M. Garcia-Sciveres,[15] A. F. Garfinkel,[25] C. Gay,[9] S. Geer,[7] D. W. Gerdes,[17] P. Giannetti,[23] N. Giokaris,[27] P. Giromini,[8] L. Gladney,[22] D. Glenzinski,[13] M. Gold,[19] J. Gonzalez,[22] A. Gordon,[9] A. T. Goshaw,[6] K. Goulianos,[27] H. Grassmann,[23] L. Groer,[28] C. Grosso-Pilcher,[5] G. Guillian,[17] R. S. Guo,[29] C. Haber,[15] E. Hafen,[16] S. R. Hahn,[7] R. Hamilton,[9] R. Handler,[34] R. M. Hans,[35] K. Hara,[32] A. D. Hardman,[25] B. Harral,[22] R. M. Harris,[7] S. A. Hauger,[6] J. Hauser,[4] C. Hawk,[28] E. Hayashi,[32] J. Heinrich,[22] K. D. Hoffman,[25] M. Hohlmann,[1,5] C. Holck,[22] R. Hollebeek,[22] L. Holloway,[11] A. Hölscher,[12] S. Hong,[17] G. Houk,[22] P. Hu,[24] B. T. Huffman,[24] R. Hughes,[26] J. Huston,[18] J. Huth,[9] J. Hylen,[7] H. Ikeda,[32] M. Incagli,[23] J. Incandela,[7] G. Introzzi,[23] J. Iwai,[32] Y. Iwata,[10] H. Jensen,[7] U. Joshi,[7] R. W. Kadel,[15] E. Kajfasz,[7a] T. Kamon,[30] T. Kaneko,[32] K. Karr,[33] H. Kasha,[35] Y. Kato,[20] L. Keeble,[8] K. Kelley,[16] R. D. Kennedy,[28] R. Kephart,[7] P. Kesten,[15] D. Kestenbaum,[9] R. M. Keup,[11] H. Keutelian,[7] F. Keyvan,[4] B. Kharadia,[11] B. J. Kim,[26] D. H. Kim,[7a] H. S. Kim,[12] S. B. Kim,[17] S. H. Kim,[32] Y. K. Kim,[15] L. Kirsch,[3] P. Koehn,[26] K. Kondo,[32] J. Konigsberg,[9] S. Kopp,[5] K. Kordas,[12] W. Koska,[7] E. Kovacs,[7a] W. Kowald,[6] M. Krasberg,[17] J. Kroll,[7]

M. Kruse,[25] T. Kuwabara,[32] S. E. Kuhlmann,[1] E. Kuns,[28] A. T. Laasanen,[25] N. Labanca,[23] S. Lammel,[7] J. I. Lamoureux,[3] T. LeCompte,[11] S. Leone,[23] J. D. Lewis,[7] P. Limon,[7] M. Lindgren,[4] T. M. Liss,[11] N. Lockyer,[22] O. Long,[22] C. Loomis,[28] M. Loreti,[21] J. Lu,[30] D. Lucchesi,[23] P. Lukens,[7] S. Lusin,[34] J. Lys,[15] K. Maeshima,[7] A. Maghakian,[27] P. Maksimovic,[16] M. Mangano,[23] J. Mansour,[18] M. Mariotti,[21] J. P. Marriner,[7] A. Martin,[11] J. A. J. Matthews,[19] R. Mattingly,[16] P. McIntyre,[30] P. Melese,[27] A. Menzione,[23] E. Meschi,[23] S. Metzler,[22] C. Miao,[17] G. Michail,[9] R. Miller,[18] H. Minato,[32] S. Miscetti,[8] M. Mishina,[14] H. Mitsushio,[32] T. Miyamoto,[32] S. Miyashita,[32] Y. Morita,[14] J. Mueller,[24] A. Mukherjee,[7] T. Muller,[4] P. Murat,[23] H. Nakada,[32] I. Nakano,[32] C. Nelson,[7] D. Neuberger,[4] C. Newman-Holmes,[7] M. Ninomiya,[32] L. Nodulman,[1] S. H. Oh,[6] K. E. Ohl,[35] T. Ohmoto,[10] T. Ohsugi,[10] R. Oishi,[32] M. Okabe,[32] T. Okusawa,[20] R. Oliver,[22] J. Olsen,[34] C. Pagliarone,[2] R. Paoletti,[23] V. Papadimitriou,[31] S. P. Pappas,[35] S. Park,[7] A. Parri,[8] J. Patrick,[7] G. Pauletta,[23] M. Paulini,[15] A. Perazzo,[23] L. Pescara,[21] M. D. Peters,[15] T. J. Phillips,[6] G. Piacentino,[2] M. Pillai,[26] K. T. Pitts,[7] R. Plunkett,[7] L. Pondrom,[34] J. Proudfoot,[1] F. Ptohos,[9] G. Punzi,[23] K. Ragan,[12] A. Ribon,[21] F. Rimondi,[2] L. Ristori,[23] W. J. Robertson,[6] T. Rodrigo,[7a] J. Romano,[5] L. Rosenson,[16] R. Roser,[11] W. K. Sakumoto,[26] D. Saltzberg,[5] A. Sansoni,[8] L. Santi,[23] H. Sato,[32] V. Scarpine,[30] P. Schlabach,[9] E. E. Schmidt,[7] M. P. Schmidt,[35] A. Scribano,[23] S. Segler,[7] S. Seidel,[19] Y. Seiya,[32] G. Sganos,[12] A. Sgolacchia,[2] M. D. Shapiro,[15] N. M. Shaw,[25] Q. Shen,[25] P. F. Shepard,[24] M. Shimojima,[32] M. Shochet,[5] J. Siegrist,[15] A. Sill,[31] P. Sinervo,[12] P. Singh,[24] J. Skarha,[13] K. Sliwa,[33] F. D. Snider,[13] T. Song,[17] J. Spalding,[7] P. Sphicas,[16] F. Spinella,[23] M. Spiropulu,[9] L. Spiegel,[7] L. Stanco,[21] J. Steele,[34] A. Stefanini,[23] K. Strahl,[12] J. Strait,[7] R. Ströhmer,[9]

D. Stuart,[7] G. Sullivan,[5] A. Soumarokov,[29] K. Sumorok,[16] J. Suzuki,[32] T. Takada,[32] T. Takahashi,[20] T. Takano,[32] K. Takikawa,[32] N. Tamura,[10] F. Tartarelli,[23] W. Taylor,[12] P. K. Teng,[29] Y. Teramoto,[20] S. Tether,[16] D. Theriot,[7] T. L. Thomas,[19] R. Thun,[17] M. Timko,[33] P. Tipton,[26] A. Titov,[27] S. Tkaczyk,[7] D. Toback,[5] K. Tollefson,[26] A. Tollestrup,[7] J. Tonnison,[25] J. F. de Troconiz,[9] S. Truitt,[17] J. Tseng,[13] N. Turini,[23] T. Uchida,[32] N. Uemura,[32] F. Ukegawa,[22] G. Unal,[22] S. C. van den Brink,[24] S. Vejcik, III,[17] G. Velev,[23] R. Vidal,[7] M. Vondracek,[11] D. Vucinic,[16] R. G. Wagner,[1] R. L. Wagner,[7] J. Wahl,[5] C. Wang,[6] C. H. Wang,[29] G. Wang,[23] J. Wang,[5] M. J. Wang,[29] Q. F. Wang,[27] A. Warburton,[12] G. Watts,[26] T. Watts,[28] R. Webb,[30] C. Wei,[6] C. Wendt,[34] H. Wenzel,[15] W. C. Wester, III,[7] A. B. Wicklund,[1] E. Wicklund,[7] R. Wilkinson,[22] H. H. Williams,[22] P. Wilson,[5] B. L. Winer,[26] D. Wolinski,[17] J. Wolinski,[30] X. Wu,[23] J. Wyss,[21] A. Yagil,[7] W. Yao,[15] K. Yasuoka,[32] Y. Ye,[12] G. P. Yeh,[7] P. Yeh,[29] M. Yin,[6] J. Yoh,[7] C. Yosef,[18] T. Yoshida,[20] D. Yovanovitch,[7] I. Yu,[35] J. C. Yun,[7] A. Zanetti,[23] F. Zetti,[23] L. Zhang,[34] W. Zhang,[22] and S. Zucchelli[2]

(CDF Collaboration)

[1] *Argonne National Laboratory, Argonne, Illinois 60439*

[2] *Istituto Nazionale di Fisica Nucleare, University of Bologna, I-40126 Bologna, Italy*

[3] *Brandeis University, Waltham, Massachusetts 02254*

[4] *University of California at Los Angeles, Los Angeles, California 90024*

[5] *University of Chicago, Chicago, Illinois 60637*

[6] *Duke University, Durham, North Carolina 27708*

[7] *Fermi National Accelerator Laboratory, Batavia, Illinois 60510*

[8] *Laboratori Nazionali di Frascati, Istituto Nazionale di Fisica Nucleare, I-00044 Frascati, Italy*

[9] *Harvard University, Cambridge, Massachusetts 02138*

[10] *Hiroshima University, Higashi-Hiroshima 724, Japan*

[11] *University of Illinois, Urbana, Illinois 61801*

[12] *Institute of Particle Physics, McGill University, Montreal H3A 2T8, and University of Toronto, Toronto M5S 1A7, Canada*

[13] *The Johns Hopkins University, Baltimore, Maryland 21218*

[14] *National Laboratory for High Energy Physics (KEK), Tsukuba, Ibaraki 305, Japan*

[15] *Lawrence Berkeley Laboratory, Berkeley, California 94720*

[16] *Massachusetts Institute of Technology, Cambridge, Massachusetts 02139*

[17] *University of Michigan, Ann Arbor, Michigan 48109*

[18] *Michigan State University, East Lansing, Michigan 48824*

[19] *University of New Mexico, Albuquerque, New Mexico 87131*

[20] *Osaka City University, Osaka 588, Japan*

[21] *Universita di Padova, Istituto Nazionale di Fisica Nucleare, Sezione di Padova, I-35131 Padova, Italy*

[22] *University of Pennsylvania, Philadelphia, Pennsylvania 19104*

[23] *Istituto Nazionale di Fisica Nucleare, University and Scuola Normale Superiore of Pisa, I-56100 Pisa, Italy*

[24] *University of Pittsburgh, Pittsburgh, Pennsylvania 15260*

[25] *Purdue University, West Lafayette, Indiana 47907*

[26] *University of Rochester, Rochester, New York 14627*

[27] *Rockefeller University, New York, New York 10021*

[28] *Rutgers University, Piscataway, New Jersey 08854*

[29] *Academia Sinica, Taipei, Taiwan 11529, Republic of China*

[30] *Texas A&M University, College Station, Texas 77843*

[31] *Texas Tech University, Lubbock, Texas 79409*

[32] *University of Tsukuba, Tsukuba, Ibaraki 305, Japan*

[33] *Tufts University, Medford, Massachusetts 02155*

[34] *University of Wisconsin, Madison, Wisconsin 53706*

[35] *Yale University, New Haven, Connecticut 06511*

Bibliography

[A+83a] G. Arnison et al. Experimental observation of isolated large transverse energy electrons with associated missing energy at $\sqrt{s} = 540$ GeV. *Phys. Lett.*, B122:103, 1983.

[A+83b] G. Arnison et al. Experimental observation of lepton pairs of invariant mass around 95 GeV/c^2 at the CERN sps collider. *Phys. Lett.*, B126:398, 1983.

[A+86a] J.A. Appel et al. Measurement of $W^{\pm}$ and Z^0 properties at the CERN $\overline{p}p$ collider. *Z. Phys.*, C30:1–22, 1986.

[A+86b] G. Arnison et al. Recent results on intermediate vector boson properties at the CERN super proton synchroton collider. *Phys. Lett.*, B166:484, 1986.

[A+87a] C. Albajar et al. Intermediate vector boson cross sections at the CERN super proton synchroton collider and the number of neutrino types. *Phys. Lett.*, B198:271, 1987.

[A+87b] R. Ansari et al. Measurement of W and Z production properties at the CERN $\overline{p}p$ collider. *Phys. Lett.*, B194:158, 1987.

[A+88a] F. Abe et al. The CDF detector: An overview. *NIM*, A271:387–403, 1988.

[A+88b] D. Amidei et al. A two level FASTBUS based trigger system for CDF. *NIM*, A269:51–62, 1988.

[A+88c] R. Ansari et al. Measurement of the strong coupling constant α_s from a study of W bosons produced in association with jets. *Phys. Lett.*, B215:175–185, 1988.

[A+88d] G. Ascoli et al. CDF central muon detector. *NIM*, A268:33–40, 1988.

[A+88e] G. Ascoli et al. CDF central muon Level-1 trigger electronics. *NIM*, A269:63–67, 1988.

[A+89] C. Albajar et al. Studies of intermediate vector boson production and decay in UA1 at the CERN proton-antiproton collider. *Z. Phys.*, C44:15–61, 1989.

[A+90a] J. Alitti et al. Measurement of the transverse momentum distribution of W and Z bosons at the CERN $\bar{p}p$ collider. *Z. Phys.*, C47:523–531, 1990.

[A+90b] J. Alitti et al. Measurement of W and Z production cross sections at the CERN $\bar{p}p$ collider. *Z. Phys.*, C47:11–22, 1990.

[A+91a] F. Abe et al. Measurement of $\sigma \cdot B(W \to e\nu)$ and $\sigma \cdot B(Z^0 \to e^+e^-)$ in $\bar{p}p$ collisions at $\sqrt{s} = 1800$ GeV. *Phys. Rev.*, D44:29–52, 1991.

[A+91b] F. Abe et al. Measurement of the e^+e^- invariant-mass distribution in $\overline{p}p$ collisions at $\sqrt{s} = 1.8$ TeV. *Phys. Rev. Lett.*, 67:2418–2422, 1991.

[A+91c] F. Abe et al. Measurement of the W-boson P_T distribution in $\overline{p}p$ collisions at $\sqrt{s} = 1.8$ TeV. *Phys. Rev. Lett.*, 66:2951–2955, 1991.

[A+91d] F. Abe et al. Measurement of the Z-boson p_T distribution in $\overline{p}p$ collisions at $\sqrt{s} = 1.8$ TeV. *Phys. Rev. Lett.*, 67:2937–2941, 1991.

[A+91e] J. Alitti et al. *Phys. Lett.*, B263:563, 1991.

[A+92] F. Abe et al. Topology of three-jet events in $\overline{p}p$ collisions at $\sqrt{s} = 1.8$ TeV. *Phys. Rev.*, D45:1448–1458, 1992.

[A+93] F. Abe et al. Measurement of jet multiplicity in W events produced in $\overline{p}p$ collisions at $\sqrt{s} = 1.8$ TeV. *Phys. Rev. Lett.*, 70:4042–4046, 1993.

[A+94a] F. Abe et al. Evidence for top quark production in $\overline{p}p$ collisions at $\sqrt{s} = 1.8$ TeV. *Phys. Rev.*, D50:2966–3026, 1994.

[A+94b] F. Abe et al. Measurement of the B^+ and B^0 Meson Lifetimes. *Phys. Rev. Lett.*, 72:3456–3460, 1994.

[A+94c] F. Abe et al. Measurement of the ratio $\sigma B(W \to e\nu)/\sigma B(Z^0 \to e^+e^-)$ in $\overline{p}p$ collisions at $\sqrt{s} = 1.8$ TeV. *Phys. Rev. Lett.*, 73:220–224, 1994.

[A+94d] D. Amidei et al. The Silicon Vertex Detector of the Collider Detector at Fermilab. *NIM*, A350:73, 1994.

[A+95a] S. Abachi et al. Study of the strong coupling constant using W + jet processes. *Phys. Rev. Lett.*, 75:3226–3231, 1995.

[A+95b] S. Abachi et al. W and Z boson production in $\overline{p}p$ collisions at $\sqrt{s} = 1.8$ TeV. *Phys. Rev. Lett.*, 75:1456, 1995.

[A+95c] F. Abe et al. Measurement of $\sigma \cdot B(W \to e\nu)$ and $\sigma \cdot B(Z^0 \to e^+e^-)$ in $\overline{p}p$ collisions at $\sqrt{s} = 1.8$ TeV. *Phys. Rev. Lett.*, submitted September 21, 1995. FERMILAB-Pub-95/301-E.

[AEM85] G. Altarelli, R.K. Ellis, and G. Martinelli. Vector boson production at present and future colliders. *Z. Phys.*, C27:617–632, 1985.

[AK91] Peter B. Arnold and Russel P. Kauffman. W and Z production at next-to-leading order: from large q_T to small. *Nucl. Phys.*, B349:381–413, 1991.

[AR89] Peter B. Arnold and M. Hall Reno. The complete computation of high-p_T W and Z production in second-order QCD. *Nucl. Phys.*, B319:37–71, 1989.

[B+69] M. Briedenbach et al. *Phys. Rev. Lett.*, 23:935, 1969.

[B+83a] P. Bagnaia et al. Evidence for $Z^0 \to e^+e^-$ at the CERN $\overline{p}p$ collider. *Phys. Lett.*, B129:130, 1983.

[B+83b] M. Banner et al. Observation of single isolated electrons of high transverse momentum in events with missing transverse energy at the CERN $\overline{p}p$ collider. *Phys. Lett.*, B122:476, 1983.

[B+84] P. Bagnaia et al. *Z. Phys.*, C24:1–17, 1984.

[B+88a] L. Balka et al. The CDF central electromagnetic calorimeter. *NIM*, A267:272–279, 1988.

[B+88b] F. Bedeschi et al. Design and construction of the CDF central tracking chamber. *NIM*, A268:50–74, 1988.

[B+88c] S. Bertolucci et al. The CDF central and endwall hadron calorimeter. *NIM*, A267:301–314, 1988.

[B+88d] G. Brandenburg et al. An electromagnetic calorimeter for the small angle regions of the collider detector at fermilab. *NIM*, A267:257–271, 1988.

[B+88e] K. Byrum et al. The CDF forward muon system. *NIM*, A268:46–49, 1988.

[B+89] F.A. Berends et al. Multijet production in W, Z events at $\bar{p}p$ collisions. *Phys. Lett.*, B224:237–242, 1989.

[B+92] B. Barnett et al. Progress in the construction of the CDF silicon vertex detector. *NIM*, A315:125, 1992.

[Bar] Vernon Barger, private communication.

[BKN91] F.T. Brandt, G. Kramer, and Su-Long Nyeo. W, Z plus jet production at $\bar{p}p$ colliders. *Int. J. Mod. Phys.*, A6:3973–3988, 1991.

[BKTG91] F.A. Berends, H. Kuijf, B. Tausk, and W.T. Giele. On the production of a W and jets at hadron colliders. *Nuclear Physics*, B357:32–64, 1991.

[C+88] S. Cihangir et al. The CDF forward/backward hadron calorimeter. *NIM*, A267:249–256, 1988.

[Dug89] G. Dugan. Tevatron collider: Status and prospects, 1989. FERMILAB-Conf-89/182.

[EKS85] S.D. Ellis, R. Kleiss, and W.J. Stirling. W's, Z's and Jets. *Phys. Lett.*, B154:435, 1985.

[F+88a] G. Foster et al. A fast hardward track-finder for the CDF central tracking chamber. *NIM*, A269:93–100, 1988.

[F+88b] Y. Fukui et al. CDF end plug electromagnetic calorimeter using conductive plastic proportional tubes. *NIM*, A267:280–300, 1988.

[FF78] R.D. Field and R.P. Feynman. A parametrization of the properties of quark jets. *Nucl. Phys.*, B136:1–76, 1978.

[GGK93] W.T. Giele, E.W.N. Glover, and D.A. Kosower. Higher-order corrections to jet cross sections in hadron colliders. *Nuclear Physics*, B403:633–667, 1993.

[GGY95] W.T Giele, E.W.N. Glover, and J. Yu. The determination of α_s at hadron colliders, 1995. FERMILAB-Pub-95/127-T.

[GHRZ95] A.T. Goshaw, S. Hauger, W.J. Robertson, and B. Zou. Monte Carlo Simulation of $\bar{p}p \rightarrow Z +$ Jets. Technical Report CDF/-ANAL/JET/CDFR/3359, Fermilab, 1995.

[Gie] Walter Giele, private communication.

[Gla61] Sheldon L. Glashow. Partial symmetries of weak interactions. *Nucl. Phys.*, 22:579–588, 1961.

[GMN64] M. Gell-Mann and Y. Ne'eman. A schematic model of baryons and mesons. *Phys. Lett.*, 8:214, 1964.

[Gol61] J. Goldstone. Field theories with 'superconductor' solutions. *Nuovo Cimento*, 19:154–164, 1961.

[Gos] Alfred Goshaw and William Robertson, private communication.

[GPW89] R.J. Gonsalves, J. Pawlowski, and Chung-Fai Wai. QCD radiative corrections to electroweak-boson production at large transverse momentum in hadron collisions. *Phys. Rev.*, D40:2245–2268, 1989.

[Hig64] P.W. Higgs. Broken Symmetries, Massless Particles and Gauge Fields. *Phys. Lett.*, 12:132–133, 1964.

[HM84] Francis Halzen and Alan D. Martin. *Quarks and Leptons: An Introductory Course in Modern Particle Physics.* John Wiley & Sons, New York, 1984.

[KF91] L. Keeble and B. Flaugher. New jet correction function QDJSCO 2.0. Technical Report CDF/ANAL/JET/CDFR/1513, Fermilab, 1991.

[L+92] M. Lindgren et al. *Phys. Rev.*, D45:3038, 1992.

[Led91] L.M. Lederman. The Tevatron. *Scientific American*, 264:48–55, 1991.

[M+92] G. Marchesini et al. HERWIG 5.1 — a Monte Carlo event generator for simulating hadron emission reactions with interfering gluons. *Comput. Phys. Comm.*, 67:465–508, 1992.

[Man] Michelangelo Mangano, private communication.

[MHvN90] T. Matsuura, R. Hamberg, and W.L. van Neerven. The contribution of the gluon-gluon subprocess to the Drell-Yan K-factor. *Nucl. Phys.*, B345:331–368, 1990.

[MW88] G. Marchesini and B.R. Webber. Monte Carlo simulation of general hard processes with coherent QCD radiation. *Nuclear Physics*, B310:461–526, 1988.

[Par94] Particle Data Group. Review of particle properties. *Phys. Rev.*, D50:1173, 1994.

[PP93] Frank E. Paige and Serban D. Protopescu. A Monte Carlo event generator for $P - P$ and $Pbar - P$ reactions, 1993.

[S+92] M. Shapiro et al. A user's guide to QFL. Technical Report CDF/-ANAL/MONTECARLO/PUBLIC/1810, Fermilab, 1992.

[Sal68] Abdus Salam. Weak and electromagnetic interactions. In N. Svartholm, editor, *Elementary Particle Theory: Relativistic groups and analyticity*, Proceedings of the Eighth Nobel Symposium held May 19–25, 1968, at Aspenäsgården, Lerum, in the county of Älvsborg, Sweden. Alqvist & Wiksell, Stockholm, 1968.

[Sho91] M. Shochet. The physics of proton-antiproton collisions, 1991. FERMILAB-Conf-91/341-E, Published Lectures, Les Houches

Summer School, Particles in the 90's, Ecole d'Eté de Physique Théorique, Les Houches, France.

[Ton93] James Tonnison. QDJSCO corrections for 6.01 data. Technical Report CDF/ANAL/JET/CDFR/2053, Fermilab, 1993. See also update by Nathan Eddy (1994); new underlying event corrections were calculated by Weiming Yao (1995).

[Wei67] Steven Weinberg. A model of leptons. *Phys. Rev. Lett.*, 19:1264, 1967.

[YM54] C.N. Yang and R.L. Mills. Conservation of spin and isotopic gauge invariance. *Phys. Rev.*, 96:191–195, 1954.

[YN90] D.E. Young and R.J. Noble. 400-MeV upgrade for the Fermilab Linac. *Part. Accel.*, 26:205–210, 1990.

[Zwe64] G. Zweig, 1964. CERN Preprint TH-401.

Biography

Susanne Andrea Hauger [redacted] She attended Duke University in her freshman year, after which she transferred to New College in Sarasota, FL. She earned her Bachelor of Arts in physics there in 1989.

She returned to Duke University on a James B. Duke Fellowship to begin graduate school, and eventually joined the High Energy Physics group. In 1991 she moved to Chicago, where she stayed for almost a year working on the CDF collider experiment at Fermilab and collecting data for her dissertation. In January of 1992 she completed her Master's Degree in physics. Since then, she has been working in the Duke high energy physics group as a research assistant.

She is a member of the American Physical Society and an Associate Member of the Duke chapter of Sigma Xi. She has presented her work at several CDF collaboration meetings and at the Albuquerque meeting of the Division of Particles and Fields in 1994.